

1 Tropical upper tropospheric trends in ozone and carbon 2 monoxide (2005–2020): observational and model results

3 Lucien Froidevaux¹, Douglas E. Kinnison², Benjamin Gaubert², Michael J. Schwartz¹, Nathaniel
4 J. Livesey¹, William G. Read¹, Charles G. Bardeen², Jerry R. Ziemke^{3,4}, and Ryan A. Fuller¹

5 ¹Jet Propulsion Laboratory, California Institute of Technology, Pasadena, California, USA

6 ²NSF National Center for Atmospheric Research (NSF NCAR), Boulder, Colorado, USA

7 ³NASA Goddard Space Flight Center, Greenbelt, MD, USA

8 ⁴Goddard Earth Sciences Technology and Research (GESTAR)/Morgan State University,
9 Baltimore, MD, USA

10 *Correspondence to:* Lucien Froidevaux (lucienf@jpl.nasa.gov)

11 **Abstract.** We analyze tropical ozone (O₃) and carbon monoxide (CO) distributions in the upper
12 troposphere (UT) and their temporal changes for 2005–2020 using Aura Microwave Limb Sounder
13 (MLS) observations and chemistry climate model simulations. The **simulations are from** the Whole
14 Atmosphere Community Climate Model (WACCM6) and two variants of the Community
15 Atmosphere Model with Chemistry (CAM-chem), each variant using different anthropogenic
16 emissions **for CO**. Upper tropospheric trends and variability diagnostics are obtained from multiple
17 linear regression analyses.

18 We compare the model and MLS annual climatologies, focusing on 147 and 215 hPa pressure
19 levels; climatological values generally fall within 10–20% of each other, with both positive and
20 negative differences for O₃, and with models generally underestimating observed CO. In the
21 northern hemisphere tropics, we find significantly poorer model fits to the observed phasing of
22 CO seasonal changes at 215 hPa than at 147 hPa. This discrepancy is much smaller for the
23 comparison of modeled and Measurements of Pollution in the Troposphere (MOPITT) V9J CO
24 columns. We also find that the sensitivity of UT CO to El Niño / Southern Oscillation (ENSO) is
25 positive at all tropical longitudes, in contrast to the dipolar longitudinal structure that exists for UT
26 O₃ ENSO sensitivity.

27 MLS O₃ has a zonal mean trend at 20°S–20°N of $+0.39 \pm 0.28$ %yr⁻¹; **the WACCM simulation**
28 **(WACCM-CEDS) and both** CAM-chem **simulations** have similar trends, **although the WACCM-**
29 **CEDS result** is somewhat smaller. Our analyses for specific latitude/longitude bins yield positive
30 trends up to 1.4 %yr⁻¹ over Indonesia and East of that region, as well as over tropical Africa and
31 the tropical Atlantic. We find broad similarities between the mapped MLS-derived UT O₃ trends

32 and corresponding mapped trends of tropospheric column ozone. Positive tropical UT mapped O₃
33 trends are generally captured by the model **simulations**, although in a more muted way. The MLS
34 zonal mean CO **UT** trend is $-0.25 \pm 0.30 \text{ \%yr}^{-1}$, whereas the corresponding model CO trends are
35 **close to** zero ($0.0 \pm 0.14 \text{ \%yr}^{-1}$) when the anthropogenic emissions used in CAM-chem and
36 WACCM are taken from Community Emissions Data System (CEDS) version 2. The non-CEDS
37 version of CAM-chem (**the CAM-chem-CAMS simulation**) **yields average** CO UT trends of 0.22
38 $\pm 0.19 \text{ \%yr}^{-1}$, in contrast to the negative **tendencies prevalent in the** MLS CO trends throughout
39 the tropics. The negative MLS tropical UT CO trends for 2005–2020 agree with (but tend to be
40 smaller in magnitude than) previously published total column CO trends.

41 **The MLS-derived upper tropospheric tropical trends in these species arise from a well-sampled**
42 **multi-year data set, with the results showing a first-order correlation to large-scale changes in**
43 **lower tropospheric composition (O₃ increases and CO decreases). We find that there are broad**
44 **similarities (and a few differences) between the measured UT trends and corresponding results**
45 **from model simulations, which incorporate state-of-the-art representations of the complex**
46 **interplay between emissions, photochemistry, convection, and transport in the upper troposphere**
47 **and lower stratosphere. These results will contribute to the continuing assessments of tropospheric**
48 **evolution, in particular the large community efforts regarding TOAR-II and CMIP-7.**

49
50

51 **1 Introduction**

52 Tropospheric ozone (O₃) can be influenced by downward transport from the stratospheric ozone
53 layer, but the main O₃ source in the troposphere is in situ photochemical formation through the
54 oxidation of carbon compounds in the presence of (catalyzing) nitrogen oxides (NO_x = NO + NO₂)
55 (Crutzen, 1973; Logan, 1985); tropospheric ozone loss is dominated by in situ photochemistry and
56 by deposition at the Earth's surface (Monks et al., 2015). Past studies have also shown that the
57 main sources of tropospheric NO_x are fossil fuel combustion, biomass burning, soil microbial
58 activity, and lightning. Global anthropogenic emissions dominate the natural NO_x sources and
59 biomass burning plays quite a significant role in the tropics. There is evidence from in situ
60 measurements from ozonesondes and commercial aircraft for slow increases in tropospheric and
61 upper tropospheric O₃ abundances (e.g., Cooper et al., 2014; Gaudel et al., 2020; Thompson et al.,

62 2021; Wang et al., 2022). At the surface, regional differences have been noted, for example, a
63 leveling off in ozone increases over western Europe and parts of the United States after the 1990s,
64 including some decreases, depending on the season. Changes in tropospheric ozone precursor
65 emissions (e.g., from NO_x, carbon monoxide – CO, and volatile organic compounds) have been
66 implicated as causes for global tropospheric ozone change over the past few decades (Zhang et al.,
67 2016; Zheng et al., 2018; Liu et al., 2022; Wang et al., 2022). Souri et al. (2017) and Zhang et al.
68 (2016), for example, discussed the existence of decreases in NO_x emissions **over developed**
69 **countries following emission regulations** after the turn of the century. In the North Atlantic region,
70 both surface O₃ and CO have decreased; Kumar et al. (2013) showed this for 2001–2011. Such
71 decreases have been attributed to a decline in anthropogenic emissions from North America that
72 more than compensate for emission increases over parts of Asia. Furthermore, after the dramatic
73 reduction in global economic activity following the CO₂ CoronaVirus Disease 2019 pandemic,
74 significant reductions in northern hemisphere (NH) tropospheric ozone values were observed in
75 2020 and 2021, although the tropical decreases are much smaller (Ziemke et al., 2022; Steinbrecht
76 et al., 2021; Bouarar et al., 2021; Miyazaki et al., 2021).

77 Carbon monoxide is another important pollutant in the troposphere. Its primary tropospheric
78 sources are incomplete combustion (**biomass burning emissions and pollution** from industrial and
79 traffic-related emissions), and the oxidation of methane and other hydrocarbons (Logan et al.,
80 1981; Crutzen and Andreae, 1990; Khalil and Rasmussen, 1990); its main tropospheric loss
81 pathway is oxidation by the hydroxyl radical (OH). Lower tropospheric CO anomalies are
82 **propagated upward by convection and general ascent to produce a tropical “CO tape recorder”**
83 (Schoeberl et al., 2006), primarily as a result of biomass burning episodes near the equinoxes
84 (Duncan et al., 2003, 2007; Logan et al., 2008; Nassar et al., 2009; Livesey et al., 2013; Huang et
85 al., 2016). Further insights into the transport of CO pollution into the upper troposphere and lower
86 stratosphere (UTLS) have been provided by Park et al. (2013), who examined CO and other species
87 from the Atmospheric Chemistry Experiment Fourier Transform Spectrometer (ACE-FTS) and
88 MLS. In the tropics, the clear signature of semiannual maxima centered around April and October
89 were observed, primarily over Africa, Indonesia, and South America, with connections to biomass
90 burning and convection patterns. Park et al. (2021) examined CO pollution transport to the UTLS
91 during and long after the highly enhanced 2015 Indonesian fire season, using a combination of CO
92 satellite data and model simulations (**with the CAM-chem model**), which generally showed

93 underestimates of satellite-derived tropospheric and stratospheric CO. In terms of tropospheric CO
94 trends, Worden et al. (2013a) found significant CO column decreases for the 2000–2011 period at
95 a rate of -1.5 \%yr^{-1} over Europe, East Asia, and the United States; **this work was based mainly on**
96 **data from the Measurements of Pollution in the Troposphere (MOPITT) and the Atmospheric**
97 **Infrared Sounder (AIRS) (see also Warner et al., 2013). Using MOPITT data, Laken and Sahbaz**
98 **(2014) obtained a significant global CO trend of -0.6 \%yr^{-1} from 2000–2012; they also pointed to**
99 **significant increasing trends over parts of Asia, South America, and Africa.** Buchholz et al. (2021)
100 found a similar result using 2002–2018 gridded time series from MOPITT CO, AIRS, and other
101 satellite instruments; the global trend for this period was found to be $-0.5 \pm 0.3 \text{ \%yr}^{-1}$, with a slower
102 decreasing trend during 2010–2018. Hedelius et al. (2021) also discussed MOPITT-inferred
103 decreasing trends in column CO for 2002–2017 and pointed out that decreases in CO emissions,
104 obtained from the Emissions Database for Global Atmospheric Research (EDGAR) version 4.3.2,
105 do not always match column CO trends. Analyses of ground-based in situ surface CO data also
106 point to a slowdown in the rate of decrease of CO after 2010, in comparison to the 2001–2010
107 decade (Patel et al., 2024). There is also a north-south interhemispheric difference in the CO
108 abundances (and total columns), along with faster rates of decrease in the northern hemisphere.
109 Decreasing CO emissions from anthropogenic and biomass burning sources appear to be the main
110 cause of global tropospheric CO decreases (Jiang et al., 2017, **Andela et al., 2017**), while secondary
111 CO resulting from methane oxidation is increasing (Gaubert et al., 2017). Some steeper CO
112 decreases have been observed in local extra-tropical near-surface data (Li and Liu, 2011; He et al.,
113 2013; Yoon and Pozzer, 2014; Gratz et al., 2015), apparently because of tighter air quality
114 standards and reduced pollution from industrial and traffic-related emissions.

115 **The upper troposphere is a complex region where production of NO_x by lightning (Schumann**
116 **and Huntrieser, 2007; Murray et al., 2014), aircraft NO_x emissions (Hoor et al., 2009; Brasseur et**
117 **al., 2016; Lee et al., 2021; Wang et al., 2022), and stratosphere-troposphere exchange (STE) (Sudo**
118 **et al., 2003; Collins et al., 2003; Hegglin and Shepherd, 2009; Hess and Zbinden, 2013; Neu et al.,**
119 **2014) can significantly impact ozone concentrations; STE plays a larger role in the extra-tropics**
120 **than in the tropics (Hsu and Prather, 2014).** Upper tropospheric trend analyses of in situ CO data
121 from commercial aircraft participating in the In-service Aircraft for a Global Observing System
122 (IAGOS, see Petzold et al., 2015) measurements have indicated decreasing trends from 1995 to
123 2013 in northern midlatitude UT CO, with some larger (and statistically robust) trends as high as

124 -2 to -3 % yr⁻¹ over eastern Asia (Cohen et al., 2018). The UT ozone trends from the latter analyses
125 were found to range between 0.25 to 0.45 ppbv yr⁻¹; this reflects changes of order 0.4–0.8% yr⁻¹.
126 In terms of variability, there are interannual composition changes in the troposphere and in the
127 UTLS associated with ENSO (Chandra et al., 1998; Ziemke and Chandra, 2003; Nassar et al.,
128 2009; Oman et al., 2011, 2013) and related sea surface temperature and pressure changes. It has
129 long been known that this important mode of climate variability that originates in the Pacific
130 Ocean, with alternating warm (El Niño) and cold (La Niña) phases, leads to disruptions in global
131 circulation patterns, and has impacts on fire and wetland emissions that affect tropospheric
132 composition (Feely et al., 1987; Jones et al., 2001; Sudo and Takahashi, 2001; Duncan et al., 2003;
133 Doherty et al., 2006; Calvo et al., 2010; Voulgarakis et al., 2015; Rowlinson et al., 2019).

134 How do changes in the upper troposphere relate to changes in the lower troposphere, such as
135 changes in emissions? There have not been many such studies in the past, in large part because of
136 the lack of well-sampled long-term data in the upper reaches of the troposphere, where ozone is of
137 radiative significance. While this region is not directly connected to surface pollution, fast
138 convection episodes in the tropics imply that there might well be some correlations between lower
139 tropospheric and upper tropospheric abundances, and even for long-term trends. Long-range
140 transport of pollution can, however, extend into the UT, and also back downward with cross-
141 continental impacts on surface pollution levels. Constraints on chemistry climate models are one
142 important goal for studies of long-term measurements of upper tropospheric composition. Such
143 studies are also expected to contribute to continuing assessments of pollutant trends in the
144 troposphere, such as the Tropospheric Ozone Assessment Report Phase II (TOAR-II), while
145 related model simulations are of interest to continuing assessments of chemistry climate models
146 (e.g., CMIP-7).

147 Tropical upper tropospheric profiles of O₃ and CO have been measured on a continuous daily
148 basis by the Microwave Limb Sounder on the Aura satellite, from a near-polar sun synchronous
149 orbit since late 2004. Here, we present results of trends and variability analyses of these data sets
150 (from 2005–2020), along with a similar treatment of UT O₃ and CO time series from two chemistry
151 climate models, “specified dynamics” versions of the Whole Atmosphere Community Climate
152 Model version 6 (WACCM6) and the Community Atmosphere Model with chemistry (CAM-
153 chem), both of which are configurations of the Community Earth System Model version 2.2
154 (CESM2.2). When using regression fits, as done here, to analyze broadscale atmospheric time

155 series, one should pay attention to likely drivers (e.g., ENSO) of variability in that region, since a
156 better fitting of such variability can reduce the resulting trend uncertainties. Altogether, we use
157 one WACCM simulation as well as two separate CAM-chem simulations (the latter two having
158 different anthropogenic emission inputs for CO), as described in Sect. 2, where we provide more
159 details about the MLS data and these model simulations. Section 3 focuses on the trend analysis
160 methodology. In Sect. 4, we discuss the analysis results for O₃, and then for CO; we review the
161 UT climatologies for these species and some differences versus model simulations, and discuss
162 results from zonal mean and mapped trend analyses. We also place our results in the context of
163 past analyses. We then finish with some brief conclusions in Section 5.

164 **2 Observations, model simulations, and trend analysis methods**

165 For both MLS and the chemistry climate models, we analyze monthly averaged zonal mean
166 time series as well as monthly-averaged longitude/latitude binned time series. The models have
167 been designed to capture key dynamical and chemical processes well enough to be usefully
168 compared to the observations. We focus on a region that is somewhat below the tropopause, to
169 minimize potential effects from stratosphere-troposphere exchange and to avoid results that might
170 depend more on lower stratospheric rather than tropospheric change.

171 **2.1 Observations**

172 The Aura MLS observational dataset considered here is taken from sixteen full years (2005
173 through 2020) of global composition measurements, with about 3500 vertical profiles per day per
174 measured species. The MLS antenna performs scans of the atmospheric limb ahead of the Aura
175 satellite in its near-polar sun-synchronous orbit. MLS measures daytime and nighttime thermal
176 emission using microwave radiometers operating at frequencies near 118, 190, 240, and 640 GHz;
177 a 2.5 THz module measured OH during the early part of the mission. The 240 GHz radiometer
178 provides the standard O₃ and CO measurements. For an overview of the MLS measurement
179 technique, the reader is referred to Waters et al. (2006). Read et al. (2006) gave a description of
180 the simulated MLS forward model and related spectra. The MLS retrievals (Livesey et al., 2006)
181 use the optimal estimation approach (Rodgers, 2000); there is no assumption of atmospheric
182 homogeneity along the line of sight (see Livesey and Read, 2000), and the retrievals make use of
183 the MLS antenna's views along overlapping tangent rays during consecutive scans of the Earth's

184 limb. The specifics of MLS data characterization and data quality, along with estimated errors and
185 related information can be found in the documentation by Livesey et al. (2022).

186 Here, we have used the latest data version from MLS, labeled version 5.0 or v5. More
187 specifically, we use the binned MLS Level 3 data sets, with a latitude grid that includes the
188 equatorial bin (-2° to $+2^{\circ}$) and the 44 other adjacent 4° -wide bins. In this work, **we use monthly**
189 **mean time series based on zonal averages as well as latitude bands divided into 12 longitude bins.**
190 The typical number of MLS profiles in a monthly zonal mean 4° bin is of order 2400, and about
191 200 for each of the 12 mapped (monthly) longitude/latitude bins. Prior to averaging the MLS data,
192 the standard MLS data quality screening criteria (Livesey et al., 2022) have been applied to all the
193 O₃ and CO Level 2 profiles; this screening removes only a very small fraction (typically **1–3%**) of
194 the retrieved profiles. In the troposphere and stratosphere, the MLS O₃ retrieval grid is defined by
195 a subset of the pressure levels given by $p(n) = 1000 \times 10^{-n/12}$ hPa, where n is the pressure level index
196 number; for CO, the grid is twice as coarse, meaning that $n/6$ is used as an exponent in the above
197 equation, rather than $n/12$. The bottom recommended levels for the O₃ and CO retrievals are at 261
198 and 215 hPa, respectively. Our tropical analyses will focus on results between 215 and 147 hPa,
199 in order to largely obtain upper tropospheric results, as more influence from the stratosphere occurs
200 as one gets closer to 100 hPa in the tropics. In the upper troposphere, the vertical resolution of the
201 O₃ and CO products is about 3 km and 5 km respectively (Livesey et al., 2022). In this region, the
202 single-profile precision (1σ random uncertainty) is 20–30 ppbv (**meaning ~35-50%**) for O₃ and
203 15–20 ppbv (**~20–30%**) for CO. For our analyses of monthly MLS averages, the relevant precision
204 for O₃ and CO reduces to ~0.5 ppbv (**~1%**) for 4° zonal means and ~2 ppbv (**~4%**) for the gridded
205 data using 30° longitude by 4° latitude bins. In addition, the methodology used by the MLS team
206 to assess the aggregate effects of estimated errors in various input parameters, coupled with
207 validation results (see Livesey et al., 2022), leads to systematic uncertainty estimates (1σ) of 5–12
208 ppbv (**~10–20%**) and 15–25 ppbv (**~20–35%**) for tropical upper tropospheric O₃ and CO,
209 respectively.

210 Following validation work on UT MLS O₃ and CO in the early few years since the Aura launch
211 (Livesey et al., 2008), studies of UT MLS O₃ by Livesey et al. (2013) focused on seasonal and
212 interannual variability and comparisons versus ozonesonde data. Despite sampling differences
213 between these measurement systems, the temporal patterns evident in the MLS UT O₃ data were
214 found to be generally well correlated with the *in-situ* data over different low latitude regions.

215 Distinct seasonality was evident in O₃ and CO (as well as MLS-derived ice water content) over
216 South America and South Africa. Other patterns such as the “wave-one” pattern in tropical O₃ (see
217 [Thompson et al., 2000, 2003, Wang et al., 2006](#)) and double peaks in O₃ variability over eastern
218 equatorial Africa (with enhancements around May/June and September to November) were
219 discussed; for MLS UT CO, distinct seasonal behavior was found, for example, in the northern
220 hemisphere tropics, over Eastern Asia and across the Pacific (see also [Huang et al., 2012](#)). [Livesey](#)
221 [et al. \(2013\)](#) and [Huang et al. \(2014\)](#) discussed the connection between emissions from intense
222 fires over Indonesia in 2006 (following the El Niño-related drought) and dramatic concomitant
223 enhancements in UT CO (from MLS data) over this region. This work has been expanded upon in
224 analyses by [Park et al. \(2013, 2021\)](#) of the significant and long-lasting impacts of more recent El
225 Niño-related droughts and wildfires on tropospheric and lower stratospheric CO abundances.

226 Regarding MLS ozone, previous work has shown vertical oscillations in zonal mean MLS
227 UTLS O₃ profiles (e.g., see [Livesey et al., 2022](#)). There are also some biases in MLS tropical UT
228 ozone values, which tend to be on the high side (by 10–20%) with respect to ozonesonde data (see
229 [Hubert et al., 2016, Fig. 6](#)), but the above issues are systematic in nature. While we think that
230 neither these biases nor the small vertical oscillations (a few % in magnitude in the region of
231 interest here) would play a major role in changing our MLS UT trend results, given the trend
232 uncertainties (discussed later), any time-dependent effect, if it exists, would be quite difficult to
233 characterize, or provide a fix for.

234 We also compare the CO simulations to CO data from Terra/MOPITT, obtained from
235 multispectral retrievals (V9J) Level 3 dry air total column data, or X_{CO} in ppbv ([Deeter et al.,](#)
236 [2022](#)). The simulated CO values are smoothed by using the MOPITT a priori columns as well as
237 the 10 layers a priori and averaging kernel profiles, as recommended for a quantitative comparison
238 of modelled and MOPITT X_{CO}.

239 **2.2 Model simulations**

240 We use the Whole Atmosphere Community Climate Model version 6 (WACCM6) and the
241 Community Atmosphere Model with Chemistry (CAM-chem), both of which are components of
242 the CESM2.2 ([Danabasoglu et al., 2020](#)). WACCM6 uses the “high-top” set of 70 model levels
243 between the surface and the lower thermosphere (~140 km), while CAM-chem uses 32 layers
244 (“low-top”) that stop in the middle of the stratosphere (~40 km). Both configurations run on a

245 horizontal resolution that is 0.95° latitude \times 1.25° longitude and share the same vertical grid in the
246 troposphere, with a vertical resolution in the upper troposphere of about 1.2 km. Both CAM-chem
247 and WACCM6 include the same representations of boundary layer processes, shallow convection,
248 liquid cloud macrophysics, and cloud microphysics (Gettelman et al., 2019). Each model employs
249 the same chemical mechanism processes (labeled TS1). The chemical scheme includes the O_x ,
250 NO_x , HO_x , ClO_x , and BrO_x families, along with CH_4 and its degradation products, as well as
251 primary non-methane hydrocarbons and related oxygenated organic compounds (Emmons et al.,
252 2020). Reaction rates follow the JPL Publication 19-5 recommendation (Burkholder et al., 2019).
253 TS1 includes a total of 231 species and 583 chemical reactions broken down into 150 photolysis
254 reactions, 403 gas-phase reactions, 13 tropospheric, and 17 stratospheric heterogeneous reactions.
255 The photolytic reactions are based on both inline chemical modules and a lookup table approach
256 (Kinnison et al., 2007). Secondary organic aerosols are represented through the Volatility Basis
257 Set approach (Tilmes et al., 2019). Comparisons of oxidants during the Korea–United States Air
258 Quality (KORUS-AQ) experiment in South Korea led to a revision of the heterogeneous aerosol
259 uptake of hydroperoxyl radicals (HO_2) to produce H_2O instead of H_2O_2 and a reduction of the
260 coefficient (γ) from 0.2 to 0.1 (Gaubert et al., 2020).

261 To accurately represent weather conditions as well as the Quasi-Biennial Oscillation (QBO)
262 and to reproduce various modes of middle atmospheric variability, both simulations are run in the
263 ‘specified dynamics’ (SD) mode. The model dynamical constraints are taken from meteorological
264 fields provided by the Modern-Era Retrospective Analysis for Research and Applications version
265 2 or MERRA-2 (Gelaro et al., 2017). Contrary to the previous SD approach, the MERRA-2 fields,
266 here the zonal and meridional winds and temperature, are first regridded to the model horizontal
267 and vertical grids. The model nudging (Davis et al., 2022) is updated at every (30 min) time step
268 using the closest 3-hourly MERRA-2 fields; nudging timescales are set at 6 hours for the CAM-
269 chem simulations and at 12 hours for WACCM6. The 11-year solar cycle variability is taken from
270 the Naval Research Laboratory’s (NRL) solar model, namely the NRL Solar Spectral Irradiance
271 version 2 (NRLSSI2; Coddington et al., 2016). Volcanic SO_2 emissions (used in sulfate aerosol
272 density calculations) are derived for significant volcanic eruptions using the Neely and Schmidt
273 (2016) database updated through the year 2020. The model scenario used here is based on historical
274 forcings (and recent updates) from the Climate Model Intercomparison Project – Phase 6
275 (Meinshausen et al., 2017). The forcings include greenhouse gases (CH_4 , N_2O , and CO_2) and

276 organic halogens. After 2014, the greenhouse gas and organic halogen inputs follow the CMIP6
277 SSP5-8.5 scenario that projects inputs beyond 2014 (O'Neill et al., 2016; Riahi et al., 2017;
278 Meinshausen et al., 2020).

279 The emissions from CMIP6 were updated to CAMS-GLOB-ANT_v5.1 in **the simulation we**
280 **refer to as CAM-chem-CAMS (CAMS is the Copernicus Atmosphere Monitoring Service)** and
281 CAMS-GLOB-ANT_v5.3 in the WACCM **simulation (labeled WACCM-CEDS)** for all surface
282 anthropogenic emissions (Soulié et al., 2024). CO anthropogenic emissions were found to be too
283 low in South Asia and China (Gaubert et al., 2023), so these emissions were replaced by the
284 Community Emissions Data System (CEDS) v2, presented in McDuffie et al. (2020), **for the CAM-**
285 **chem-CEDS simulation also analyzed here, and for the only WACCM simulation used here. We**
286 **can thus exclude a change in CO secondary formation or sink between these two simulations.**
287 Daily biomass burning emissions are obtained from the Quick-Fire Emissions Dataset (QFED) 2.5
288 (Darmenov and da Silva, 2014) in **all three** simulations.

289 **The lightning NO_x production and its role in ozone formation is reviewed by Verma et al.**
290 **(2021). This study showed that most lightning activity occurs within deep convective clouds in the**
291 **tropical and subtropical region. In our study, the emission of NO from lightning is based on the**
292 **Price parametrization (Price and Rind, 1992; Price et al., 1997). This parameterization**
293 **is dependent on cloud height, which includes a stronger dependence over land versus ocean**
294 **(Emmons et al., 2010). The CAM-Chem and WACCM models used here derive tropical (and**
295 **global) lightning NO_x values of 2.34 (3.23) and 2.78 (4.11) Tg (N) yr⁻¹, respectively (Table 1),**
296 **with no significant trends over the course of these simulations. These global values are within the**
297 **generally accepted global range of 3–8 TgN yr⁻¹ for lightning NO emission (Schumann**
298 **and Huntrieser, 2007).**

299 Aircraft emissions from CMIP6 were employed in WACCM6. **Both CAM-chem simulations**
300 **use the version 2.1 of CAMS-GLOB-AIR for aircraft emissions described by Soulié et al. (2024).**
301 Gaubert et al. (2020, 2023) found that this version of CAM-chem tends to overestimate
302 tropospheric oxidants, such as ozone, hydrogen peroxide, nitric acid, and hydroxyl radical,
303 resulting in a shorter lifetime of tropospheric methane and CO, mainly in the northern hemisphere
304 extra-tropics. Some of the main model characteristics (with a focus on the differences) are
305 summarized in Table 1.

306 In terms of the model run analyses, we follow the same basic approach as for the MLS data.
307 The daily model profiles are first interpolated (as a function of $\log(\text{pressure})$) onto the MLS
308 pressure grid and then binned and averaged to produce the monthly zonal means (on a 4° latitude
309 grid) and gridded data on the same latitude/longitude grid as is described in Sect. 2.1 for MLS. **We**
310 **note also that we do not find much impact on the MLS versus model comparisons if we use a**
311 **vertically smoothed version of the model profiles, which more properly takes into account the**
312 **vertical resolution of the MLS observations, as the differences between smoothed and unsmoothed**
313 **zonal mean values are much smaller than the model biases. For general simplicity, and for the**
314 **above reasons, we use unsmoothed model values in this work. A more detailed example of**
315 **smoothed model profile analyses is provided further below, in connection with observed seasonal**
316 **CO differences between the models and the MLS measurements.**

317 **2.3 Trend analysis methods**

318 For both MLS and model time series trend analyses in the upper troposphere, we use the
319 multivariate linear regression (MLR) method discussed as part of similar studies performed by
320 Froidevaux et al. (2019) for the stratosphere. We refer the reader to Appendix (A3) of the above
321 reference for more details on the regression fit model, which includes commonly used functional
322 terms, namely a linear trend, and cosine and sine functions with **annual and semi-annual**
323 **periodicities, to account for these known variabilities in atmospheric composition, with 3- and 4-**
324 **month periodic components to better fit shorter-term (intra-seasonal) variations, which also helps**
325 **to reduce the trend error bars. In addition, we include functions describing multi-year variations**
326 **caused by the QBO (which mostly affects the stratosphere) and by ENSO, which has been tied, for**
327 **example, to regional droughts and biomass burning events, with related increases in convection**
328 **and transport of surface pollution into the upper troposphere.** The QBO-related equatorial wind
329 dataset is obtained from the publicly available datasets at the Free University of Berlin. ENSO-
330 related data are in the form of a multivariate index, following the initial work of Wolter and Timlin
331 (2011), as updated by Zhang et al. (2019). We have also included a fitted component that follows
332 variations in solar radio flux (at 10.7 cm), based on Canadian solar measurements (Tapping, 2013);
333 this component typically plays a negligible role in our results. For trend uncertainty estimates, as
334 discussed also by Froidevaux et al. (2019, 2022), we use the block bootstrap resampling method
335 (Efron and Tibshirani, 1993), as done by Bourassa et al. (2014) and others in such atmospheric

336 composition analyses. For every fitted time series, we analyze thousands of re-samplings of the fit
337 residuals, with year-long blocks of residual values replaced by residual series from randomly
338 chosen years; twice the standard deviations in these random distributions' trends provide the (2σ)
339 trend uncertainty values that we use as trend error bars throughout this work.

340 **3 Results**

341 **3.1 Climatologies**

342 Although this work focuses on variability and underlying trends, we start in Fig. 1 by showing
343 annually-averaged climatological ozone comparisons between MLS, the WACCM-CEDS
344 simulation, and the CAM-chem-CEDS simulation for 2005–2020 at 147 and 215 hPa for low
345 latitudes (4-degree bin centers between 24°S and 24°N); mapped fields and zonal mean line plots
346 are compared in this figure. At 215 hPa near 20°N and 20°S, the zonal mean O₃ values from both
347 models are ~5–15% lower than the MLS fields; differences of this order are also observed in the
348 mapped fields. The differences reach about -20% in the deep tropics, as the MLS latitudinal
349 gradients are flat in this region, in contrast to the models' more curved behavior, with a minimum
350 at the equator (see panel (k)). The differences observed here are within the MLS systematic
351 uncertainties mentioned in Sect. 2.1 (up to 24 ppbv, 2σ). These two models agree quite well in the
352 UT region as a whole (typically within about 5 ppbv); such a good level of agreement is not too
353 surprising, given that these models are based on a very similar framework, with nearly identical
354 inputs (see Sect. 2.2). At smaller pressures (147 hPa and also for 100 hPa, which is not shown
355 here), the models follow the MLS latitudinal gradients better (see panel (d) for the comparison at
356 147 hPa), as well as the longitudinal features (including the well-known wave-one ozone pattern
357 discussed by Thompson et al., 2000, 2003, Wang et al., 2006, and others). However, the models
358 exhibit a positive average bias versus MLS at these two pressure levels (see panel (e), where the
359 model bias for 147 hPa is about +20%). However, MLS UT O₃ profiles have been found to be
360 biased positively (by about 10–20%) versus averaged tropical ozonesonde profiles (Sect. 2.1).
361 Thus, positive model biases versus MLS ozone in the tropical UT are not likely caused by a
362 significant underestimate by MLS. We note that the positive model biases (at 147 and 100 hPa)
363 occur for all months of the year (not shown here), so this is not caused by a very large bias in some
364 months, that could be partially compensated for by negative model biases in other months.

365 For CO, a similar set of annual mean climatological plots as those from Fig. 1 is provided in
366 Fig. 2. We observe that the model CO values follow the patterns of the MLS UT CO fields fairly
367 well, and the zonal mean model biases are usually **around -10% to -20%**; the model biases are
368 most often negative, and more so in the northern tropics at 215 hPa. Again, it does not appear that
369 vertical smoothing of the models with MLS averaging kernels would account for the **differences**
370 **between models and** MLS (see more details further below). The model **mean CO** biases shown in
371 Fig. 2 are well within the MLS CO systematic uncertainties mentioned in Sect. 2.1; the CAM-
372 chem-CEDS climatological UT CO is slightly closer to the MLS UT CO climatology than is the
373 WACCM-CEDS CO climatology. As in the case of ozone, the aforementioned model versus data
374 CO biases are found to exist not only for annual averages, but also on a month-to-month basis.
375 The SPARC Data Initiative report (SPARC, 2017) and the more recent update by Hegglin et al.
376 (2021) showed that MLS CO values in the tropical UT are within about 10–15% of the mean values
377 that include other data from ACE-FTS and the Michelson Interferometer for Passive Atmospheric
378 Sounding (MIPAS). However, the MLS mean values are larger than the multi-instrument mean at
379 100 hPa by about 10–20%, which can account for more than half of the MLS/model bias at this
380 level (not shown here). Also, just considering the theoretical systematic uncertainty estimates
381 provided in Sect. 2.1, it is possible that most (or even all) of the **bias between models and** MLS at
382 100 hPa is caused by a positive bias in the MLS CO data. However, an earlier WACCM-CEDS
383 version (WACCM4) underestimated CO and other hydrocarbon data in the southern tropical UT,
384 as described by Park et al. (2013); those authors noted that model deficiencies in emission source
385 strengths or in the upward rate of transport could potentially explain these model underestimates.
386 As mentioned previously, we focus on the upper tropospheric region, somewhat removed from the
387 tropopause, with 147 to 215 hPa being the main levels of interest in the analyses below; while the
388 UT average differences between model and MLS are worth noting, this is not a primary concern
389 in terms of the trend comparisons that we focus on here.

390 **3.2 Zonal mean trends**

391 Figure **S1** gives some time series examples for ozone at 12°N and 12°S at 147 and 215 hPa,
392 with the MLS and modeled (WACCM-CEDS) series and their respective regression fits, along
393 with the fitted trend lines. The linear correlation coefficients listed above each panel provide a
394 measure of how well the chemistry climate model can fit the MLS series variability. The UT O₃

395 WACCM-CEDS trends roughly follow the trends that are obtained from the MLS regression fits.

396 For CO, the time series provided in Fig. S2 show that there are some slight differences in the
397 trends between observed and modeled (WACCM-CEDS) CO, with more negative trends in the
398 MLS series than in the model series. The large variability seen in the MLS CO series shows
399 correlation with WACCM-CEDS (see the large correlation coefficient values, R, in the 12°S series
400 for 147 and 215 hPa). We know that the largest CO peaks in these time series are tied to surface
401 emissions, convection, and subsequent transport into the upper troposphere and lower stratosphere
402 (UTLS), with a strong connection to El Niño-related droughts and intense fire (biomass burning)
403 events (see, e.g., Schoeberl et al., 2006, Jiang et al., 2007, Liu et al., 2013, Park et al., 2021, Duncan
404 et al., 2003, 2007). At 12°N, however, the observed CO variability is somewhat smaller than at
405 12°S, and the model variability is much more muted, while the model versus MLS phasing
406 agreement is quite poor, especially at 215 hPa (where R is very small and the MLS time series
407 annual phase is very poorly matched by the model). We have checked that this poor correlation is
408 not tied to an issue involving the smoothing of model profiles to account for the MLS averaging
409 kernels; indeed, Fig. S3 shows the small relative impact resulting from a smoothed (versus
410 vertically interpolated) model series on the average CO profile at 215 hPa and 12°N, as well as
411 regarding the smoothed time series and its phasing.

412 Regarding the trends, we now switch to results from our analyses of the monthly zonal mean
413 MLS and model time series. Figure 3 displays ozone trend results for MLS and the
414 for 147, 178, and 215 hPa, based on a multiple linear regression analysis of the
415 respective time series from 2005 through 2020. Figure 3 shows that the tropical upper tropospheric
416 MLS ozone trends are generally positive and significant (meaning that a zero trend lies outside the
417 2σ estimate of trend uncertainty). The observed average ozone trends at all three pressure levels
418 lie within about 0.3 to 0.5 % yr⁻¹; the peak average trends occur at 178 hPa. There are fairly small
419 latitudinal differences at 178 and 215 hPa. At 147 hPa, the MLS results indicate ~50% larger trends
420 in the NH tropics than in the SH tropics, although this difference is not very significant. The zonal
421 mean MLS ozone trend (averaging the three pressure levels at 147, 178, and 215 hPa) for 2005–
422 2020 in the 20°S–20°N UT region is 0.39 ± 0.28 % yr⁻¹. The error bars here indicate the 2σ trend
423 uncertainty (calculated here as the root mean square of the 2σ trend uncertainties at all three
424 pressure levels in Fig. 3). This tropical UT O₃ trend is equivalent to 0.21 ± 0.15 ppbv yr⁻¹ (based
425 on the annual average tropical UT values of 56 ppbv measured by MLS). The corresponding model

426 O₃ zonal mean trend results obtained here for 2005–2020 have a positive trend, with excellent
427 agreement with MLS from CAM-chem-CEDS ($0.38 \pm 0.28 \text{ \%yr}^{-1}$). This agreement is also apparent
428 in the latitudinal pattern, with larger trends in the NH than in the SH, even if the error bars are
429 large enough that there is no “statistically significant difference” between the hemispheres. There
430 is also good statistical agreement between the MLS trends and the slightly smaller WACCM-
431 CEDS trends ($0.21 \pm 0.23 \text{ \%yr}^{-1}$). We note that statisticians have been working to guide or adjust
432 “common practices” regarding statements of “significance”, and one should be sensitive to some
433 of the broad differences that occur even within the so-called formal criteria (such as 2σ or a
434 p-level of 0.05), which could sometimes be interpreted in too stringent a way (Wasserstein et al.,
435 2019), and as pointed out by Y. Cohen (private communication, 2024). We keep this in mind in
436 some of our discussions here, but we also wish to comment specifically on the use of broader
437 latitude bins. Indeed, if broader latitude regions were analyzed for trends, the corresponding trend
438 uncertainties would be reduced, which could make some of the compared trends differ by more
439 than their 2σ error bar variability. However, the trend error reduction in our testing with a 20° -
440 wide latitude bin instead of a 4° bin is only 5–10%, meaning that the uncertainties get divided by
441 much less than the square root of the number of small latitude bins used (an error reduction result
442 corresponding to zero correlation in the temporal variability between bins, e.g., if random noise
443 alone was present). Thus, we do not readily obtain more significant differences in these trend
444 comparisons by just averaging over broader regions. In Figure 4, the MLS and CAM-chem-CEDS
445 UT O₃ trend sensitivity analysis is repeated for 2005–2018, 2005–2019, 2006–2020, and 2007–
446 2020, showing the relative insensitivity of the MLS results to the choice of time period. This is
447 also true for the CAM-chem-CEDS trends in the NH tropics, although there is more ozone trend
448 sensitivity to the time period choice in this model’s results over the SH tropics. The WACCM-
449 CEDS tropical UT ozone trend results versus time period (not shown here) lead to a spread in the
450 SH tropical trends that is about halfway between the small MLS trend spread and the larger CAM-
451 chem-CEDS trend sensitivity shown in Fig. 4.

452 For the UT CO trends, Figure 5 provides results in a similar way as shown in Fig. 3 for ozone,
453 but for just the two MLS CO retrieval levels at 147 and 215 hPa. In contrast to ozone, we can see
454 that the MLS-derived tropical UT CO values have typically decreased from 2005 to 2020; these
455 CO trends display negligible latitude dependence. Using the same approach as for ozone, but based
456 on the Fig. 5 results, we obtain an average MLS-based UT CO trend of $-0.25 \pm 0.30 \text{ \%yr}^{-1}$

457 (equivalent to -0.20 ± 0.23 ppbv yr⁻¹). The trends at 215 hPa (-0.16 %yr⁻¹) are a factor of two
458 smaller than those at 147 hPa (-0.34 %yr⁻¹), although both of these numbers agree within the (2σ)
459 trend uncertainties of 0.3 %yr⁻¹; based on the error bars, the CO trend from MLS at 147 hPa is
460 different from zero, while the corresponding MLS trend at 215 hPa is not. In contrast, the average
461 CAM-chem-CAMS UT CO trend at these levels is 0.22 ± 0.19 % yr⁻¹, with little difference
462 between 147 and 215 hPa. The two simulations that use CEDS emissions (WACCM-CEDS and
463 CAM-chem-CEDS) yield smaller trends for CO, namely 0.0 ± 0.14 %yr⁻¹, with slightly negative
464 average trends at 147 hPa and slightly positive average trends at 215 hPa. This difference in trends
465 can be explained by significant decreases in Chinese anthropogenic emissions in CEDSv2, despite
466 the increasing anthropogenic tropical CO emissions in both CAMS-GLOB-ANTv5.1 and CEDSv2
467 (see Fig. S4).

468 Furthermore, larger MLS CO abundances in 2020 explain why the MLS CO UT trends are
469 more negative if one stops the analyses in 2018 or 2019, as can be seen from Fig. 6, which is
470 analogous to the ozone trend sensitivity study provided in Fig. 4. Regarding another aspect of CO
471 trend sensitivities, we considered the issue of large peaks in the observed MLS CO time series (see
472 examples in Fig. S2) typically resulting from El Niño related biomass burning events, followed by
473 convective uplift and CO advective transport into the UTLS. If the model has smaller peaks than
474 the MLS data show, it may be that this could explain some differences, or even a change of sign
475 in the trends. This would stand out more if the large peaks occurred close to the beginning or end
476 of the time series. As a sensitivity test, we artificially suppressed the peaks in these series by setting
477 any CO value larger than 2.5 times the (1σ) variability to a value of 1.5 times this variability, and
478 we found the impact on the linear trends to be negligible (well within the error bars shown here).
479 Such a sensitivity study gives added confidence in the robustness of these trends.

480 In Fig. 7(old9), we show the MLS, WACCM-CEDS, and CAM-chem-CEDS climatological
481 mean CO changes over the annual cycle at 215 hPa for 12°N and 12°S, along with the range of
482 variability (twice the standard deviations about the means). The fits from the models to the MLS
483 CO behavior at 12°S are quite good. The MLS CO curves show the two maxima previously
484 observed in seasonal analyses of biomass burning events, with related upward injections of CO
485 and their subsequent transport to the UT being implicated. Based on fire counts from satellite data
486 (see e.g., Duncan et al., 2003, 2007), a March biomass burning maximum has been associated with
487 the northern hemisphere (mainly from Southeast Asia, but also from northern Africa); outflow

488 from the Asian monsoon contributes to the August NH maximum. The September/October
489 maximum arises from the southern hemisphere (Indonesia, Malaysia, Southern Africa, Brazil). We
490 should also note (more broadly) that the climatological double maximum CO structure measured
491 by MLS near 215 hPa over the broader (20°S–20°N) tropics is well matched by MIPAS CO zonal
492 means (see SPARC DI, 2017, chapter 4). At 12°N, however, the lack of correlation between the
493 model variations and those deduced from MLS in Fig. 7(old9) appears to stem from the poorly
494 modeled double maximum structure; we also find that these poorer fits occur more generally
495 throughout the northern tropics. The model underestimates the boreal winter buildup of CO
496 (Gaubert et al., 2020; 2023), which may explain a poor representation of the northern hemisphere
497 March/April maximum. Also, biomass burning emission biases can vary regionally and this might
498 explain some of the model/data differences, with some regions providing somewhat better
499 comparisons than others. We do not ascribe the larger model/MLS discrepancies at 215 hPa in the
500 northern tropics to an undue influence of the MLS a priori on the retrievals in this region, as the
501 (averaged) a priori MLS values (although not shown in Fig. 7(old9)) follow the WACCM-CEDS
502 fields quite well, and the MLS CO retrievals are producing significantly different variations. To
503 explore this hemispherical asymmetry further, we show CO column comparisons between zonal
504 mean time series from MOPITT, CAM-chem-CEDS and WACCM-CEDS in Fig. 8(old10); all CO
505 columns are averaged over the same latitudes (10°N–14°N and 10°S–14°S). We obtain much better
506 agreement in the phasing of these CO column comparisons for 12°N than we do in the model
507 versus MLS CO comparisons at 215 hPa in Fig. 7(old9). This is clearly seen in the time series
508 evolution, as well as in the correlation coefficients shown in both of these Figures, although R is
509 smaller at 12°N than at 12°S in Fig. 8(old10) (but still about 0.75 to 0.8). We also look at this issue
510 for the gridded fields and provide R values for the 12°N and 12°S bins in Fig. 9(old11), where we
511 superpose the column CO model results versus MOPITT and the 215 hPa model results versus
512 MLS as a function of longitude. Again, we observe that R is much higher for the CO total columns
513 than for the 215 hPa level, especially so in the northern tropics. The patterns versus longitude
514 indicate that poorer correlations exist over the Atlantic Ocean (just West of the Greenwich
515 meridian) than over land masses. We do not have clear explanations for the exact patterns in
516 Fig. 9(old11), except for the suggestion that regions with strong land convection might show better
517 UT correlations between models and data, while outflow regions (downwind of convection) in the
518 upper troposphere could be more poorly modeled. The models do not follow the observed UT CO

519 seasonal behavior in a narrow UT region of the northern tropics, even if the modeled seasonal total
520 columns compare well to MOPITT columns in that region. More in-depth analysis would be
521 needed to probe **whether this might be caused by a poor representation of emissions and/or**
522 **transport to this region**. Alternatively, it might be that currently unaccounted for variations of the
523 MLS vertical averaging kernels could affect the (properly smoothed) model values in the northern
524 hemisphere tropics at 215 hPa, in ways that are somehow significantly different than what we show
525 in Fig. S3; this is highly unlikely, given that the smoothed model plots in this Figure hardly change
526 if we replace the tropical MLS averaging kernel values used in that plot by kernels appropriate for
527 70°N. Another potential issue might be poorly understood cloud impacts on the 215 hPa MLS
528 retrievals, specifically in the northern hemisphere tropics; although this is speculative, it might be
529 worth exploring in the future.

530 **3.3 Mapped trends**

531 We now turn to the mapped tropical UT trends by analyzing subsets of the O₃ and CO fields
532 from MLS and the models, based on monthly mean time series for 2005–2020 in latitude/longitude
533 bins, rather than on zonal means. As mentioned previously, these bins are also 4° wide in latitude,
534 and the longitude bins are 30° wide. The same regression methodology as described previously
535 here is used for each of the binned time series; we focus on the WACCM-CEDS and CAM-chem-
536 CEDS ozone trends, as we have found that the CAM-chem-CAMS and CAM-chem-CEDS results
537 are quite similar, in the case of ozone at least. Figure 10(old12) shows the resulting mapped O₃
538 trends from MLS and the two models for 147 and 215 hPa (top and bottom rows, respectively),
539 with the maps spanning 26°S to 26°N. **Hatched bins indicate trends for which the 2σ uncertainty**
540 **range encompasses the zero trend value which is often interpreted as a low level of “statistical**
541 **significance”, although one should be cautious (see the previous Section) regarding the strict**
542 **application of such a criterion or wording. The largest MLS trends are observed over the**
543 **Indonesian region and (mostly) to the East of that region, as well as over the northern Atlantic.**
544 **The mapped trends confirm the overall zonal mean result of slightly larger O₃ trends in MLS than**
545 **in WACCM-CEDS. Broad regions with positive tendencies are observed in both model trend**
546 **results; these regions include SouthEast Asia, Indonesia, northern Australia, the Atlantic, and**
547 **northern Africa, with some, but not exact agreement with the regions mentioned above for the**
548 **larger MLS trends. At 215 hPa, the slightly larger positive trends in CAM-chem-CEDS than in**

549 WACCM-CEDS over the Australian region (bottom right quadrant, south of the equator)
550 contribute to the better correspondence between the zonal mean O₃ trend results (Fig. 3c) between
551 CAM-chem-CEDS and MLS over the southern tropics. The mapped trend discrepancies between
552 the simulations and MLS are rarely outside the 2σ error bar ranges. Nevertheless, some of the
553 discrepancies are worth noting, especially when they cover multiple adjacent bins; in particular,
554 the easternmost longitude band shows MLS trends with (significant) positive values, in contrast to
555 the simulation results, with binned trends that are often small and/or negative.

556 We have compared these mapped ozone trend results to those for tropospheric column ozone
557 (TCO) obtained by Ziemke et al. (2019), using a combination of total O₃ columns from the Aura
558 Ozone Monitoring Instrument (OMI) and MLS-based stratospheric O₃ columns. In Fig. 11(old13),
559 we show in the top two rows the trends from MLS ozone at 178 hPa (top map) versus the bottom
560 map which provides the mapped TCO trends for the same time period, obtained from an
561 appropriate horizontal smoothing of the results obtained following the above reference, to make
562 the MLS and TCO resolutions comparable; this smoothing comes from an interpolation versus
563 latitude and a weighted averaging in longitude, since the TCO results have finer longitudinal
564 resolution (5°-wide bins) than the MLS longitudinal grid used here (30°-wide bins). Similarities
565 are observed in the longitudinal pattern of UT O₃ and TCO trends, as shown also for 3 different
566 latitude bins in panel (c) of Fig. 11(old13); variations of a factor of two to three are observed,
567 mostly in the northern half, between the western and eastern hemispheres for both sets of trends,
568 which tend to lie between roughly 0.3 and 1.2 % yr⁻¹. However, the agreement between MLS UT
569 O₃ and TCO trends is often worse for other MLS pressure level choices; this can be deduced from
570 panel (d), where R (correlation coefficient) values relating to the longitudinal variations obtained
571 from MLS at different pressures versus the longitudinal variations in TCO are displayed as a
572 function of latitude (y-axis). In fact, one might not expect the MLS ozone UT trends to track the
573 TCO trends very well, given that TCO measures the entire column whereas MLS measures trends
574 in a vertical region about 5 km wide in the upper troposphere, but this was worth looking into.
575 Regional variability and horizontal sampling differences between MLS and OMI will also play a
576 role (see Thompson et al., 2021, for variability aspects of sonde-derived tropospheric trends). Our
577 comparisons imply that the correlation between lower and upper tropospheric ozone trends is not
578 a strict “one-to-one mapping”, but there are nevertheless some similarities between these regions.

579 In Fig. 12(old14), we show the mapped CO trend results for MLS and all three simulations
580 (WACCM-CEDS, CAM-chem-CAMS, and CAM-chem-CEDS) at 147 and 215 hPa. As seen
581 above, MLS CO trends in the UT are generally negative, with the more statistically significant
582 result occurring at 147 hPa (where the trends are more negative than at 215 hPa). There is an
583 indication of slightly positive trends over or near western Africa, mainly at 215 hPa, although this
584 is not statistically significant. The binned model results from CAM-chem-CAMS confirm the
585 zonal mean view from this model, with mostly positive trends, in contrast to the generally
586 tendencies in the MLS trend results. The average trends (from both pressure levels) based on all
587 grid cells for MLS is -0.25 \% yr^{-1} , as opposed to $+0.24 \text{ \% yr}^{-1}$ obtained from CAM-chem-CAMS.
588 Of note, these values lie well outside twice the standard errors in the means (of 0.1 \% yr^{-1}),
589 although one should understand that there are limitations in the use of such a small error bar, given
590 the existence of correlations in atmospheric variability between the various bins. When the CEDS
591 emissions are used, as done for WACCM-CEDS and CAM-chem-CEDS, there is a general
592 decrease in the UT CO trends, with some small negative values, although the vast majority of the
593 model CO trends obtained here are not statistically different from zero within any given bin. The
594 averaged UT mapped trend for CAM-chem-CEDS is 0.0 \% yr^{-1} , with twice the standard error in
595 the mean also about 0.1 \% yr^{-1} . While the use of the model CEDS emissions does lead to a better
596 model agreement with the gridded MLS UT CO trends, the MLS-derived trends are still, on the
597 whole, more negative than these simulated CO trends.

598 We have also analyzed the level of explained variance in the regression fits for these binned
599 trend results. Figure 13(old15) shows the square of the correlation coefficient values (R^2) as a
600 function of latitude and longitude for different explanatory variables used in the binned O_3 fits at
601 147 hPa, based on fit comparisons to the MLS series (top 6 panels), and for the regression fit versus
602 the WACCM-CEDS series (bottom 6 panels). We have ignored the solar component in these plots
603 as it was found to be of negligible importance; we display the remaining contributions, namely the
604 annual, semi-annual, short-term (sum of the 3-month and 4-month terms), QBO, and ENSO terms,
605 as well as the contribution from the full regression fit, which shows that most (but certainly not
606 all) of the time series variance can be explained by such a regression model. The annual term and
607 semi-annual terms can generally explain a large part of the variance, usually followed in
608 importance by the ENSO term, over most of the Pacific. The QBO component is very small in the
609 upper troposphere, even though it is a well-known and large contributor to stratospheric trace gas

610 variability in the lowermost stratosphere. There is **also** a significant annual cycle in the tropical
611 lowermost stratosphere related to variations in vertical velocities and in the Brewer-Dobson
612 circulation (Randel et al., 2007; Witte et al., 2008). The R^2 patterns observed in the MLS panels
613 are reproduced in a broad sense by the fits to the CCM, as shown in the bottom 6 panels; this is
614 also a result of the close match between the CCM and the MLS O_3 time series, shown earlier in
615 this work. The ENSO model pattern for O_3 does not match the MLS-derived pattern that well over
616 Indonesia, but this comparison is generally better in the Pacific region between -90° and -180° . **A**
617 **somewhat weaker R^2 value in the model simulation also exists in parts of the Eastern hemisphere**
618 **for the semi-annual term. The combination of these differences helps to explain the somewhat**
619 **poorer overall fits (and variance contributions) for the model than for MLS.** For the most part, it
620 does not matter much which model run is used for these analyses, or even which pressure level is
621 used; **indeed**, the results at 215 hPa (see Fig. S5) are **generally** similar to those in Fig. 13(old15).

622 For CO, we repeat in Fig. 14(old16) the explained variance analysis provided in Fig. 13(old15)
623 for O_3 . Overall, the full fits explain less of the variability in the CO case, in part because of the
624 large ENSO-related peaks that occur throughout the MLS and WACCM-CEDS records, which the
625 regression model, as designed, can only imperfectly match. Also, there are regions in the southern
626 tropics where the annual cycle in the model is better fit by the regression than in the MLS case,
627 and this translates to a somewhat better overall full fit. For both MLS and model, the semi-annual
628 cycle component shows peaks over the South Atlantic region, which is likely linked to biomass
629 burning **in Africa** and related CO transport to the UT following convective activity (e.g., Duncan
630 et al., 2007; Park et al., 2013, 2021). **As for the ozone case, the QBO-related UT variability in the**
631 **tropics is very small (as seen from the QBO R^2 contributions). For both MLS and model**
632 **representations, the ENSO-related correlation patterns are broadly similar to the ozone case, in**
633 **that there is larger variance in the more extreme longitudes of both western and eastern sides. As**
634 **for O_3 , there are somewhat smaller variance contributions in the Eastern hemisphere from ENSO**
635 **and the semi-annual term than in the MLS case. At 215 hPa (see Fig. S6), the ENSO variance**
636 **contribution is slightly larger than at 147 hPa only in a small number of bins, but the overall ENSO-**
637 **related patterns are not stronger, as seen also in the CO sensitivity coefficients to ENSO in Figure**
638 **16(old18) below, which shows only slight differences between the two pressure levels.**

639 To pursue the ENSO-related patterns further, one can obtain a (mapped) sensitivity coefficient
640 to ENSO from the regression fits regarding this component's importance in ppbv/K (where "K"

641 relates to tropical sea surface temperatures changes). The O₃ ENSO sensitivity is shown in Fig.
642 15(old17) for the 2005–2020 MLS and WACCM-CEDS results at 147 and 215 hPa. This provides
643 more information about the sign of the sensitivity over different regions, and we observe generally
644 positive (negative) sensitivity in the Eastern (Western) hemisphere, for both MLS and WACCM-
645 CEDS cases; moreover, at least at 147 hPa, there are two strong negative minima on each side of
646 the Equator in the central Pacific region. The model results are quite consistent with those from
647 MLS in terms of the ENSO-related sensitivity coefficient patterns and magnitudes, although the
648 model response is often slightly smaller than seen in the MLS result. As we discuss further below,
649 such ozone sensitivity patterns have been described and interpreted before. Figure 16(old18)
650 provides the same analysis, but for the CO sensitivity to ENSO. These maps show a positive CO
651 ENSO sensitivity coefficient throughout the tropics, with local maxima in both the Eastern and
652 Western hemispheres, rather than the O₃ dipole (positive/negative) structure shown in Fig.
653 15(old17). The model CO ENSO sensitivity broadly matches the MLS results, although it is not
654 as strong; the different patterns in the western hemisphere, compared to the O₃ sensitivity to ENSO,
655 might be caused by differences in O₃ and CO vertical profile gradients in these regions, but this
656 would require further detailed investigations. We also note that, especially in the MLS case, the
657 peak magnitudes of the CO ENSO sensitivity coefficients in Fig. 16(old18) match the peak
658 magnitudes of the positive O₃ ENSO sensitivity in Fig. 15(old17).

659 4 Discussion

660 We have found some climatological differences between the MLS observations of O₃ and CO
661 in the tropical upper troposphere and the WACCM-CEDS simulation, as well as both CAM-chem
662 simulations considered here. For O₃, the models underestimate the mean MLS values at 215 hPa;
663 at 147 hPa, the models are biased high by about 15–25%, and we have no reason to believe that
664 such positive biases result from an average negative bias in the corresponding MLS values. For
665 CO, the models underestimate the MLS UT values by up to 20%, and these differences could be
666 readily caused by systematic biases in either MLS or the models, or both. Park et al. (2013) also
667 found that model CO values from a (WACCM4) simulation at 147 hPa were smaller than the ACE-
668 FTS (and MLS) CO abundances, especially in the SH sub-tropics; they attributed this to a possible
669 underestimation of surface emissions or transport via deep convection. We note that low biases in
670 simulated tropospheric CO have also been found before at northern latitudes and may arise from

671 various factors, such as underestimated CO emissions, high biases in modeled tropospheric OH
672 (Strode et al., 2016; Gaubert et al., 2023), or issues with simulated CO dry deposition rates (Stein
673 et al., 2014). Based on our model/MLS comparisons of UT CO seasonal changes, we find
674 significantly poorer matches at 215 hPa in the northern tropics **than in the southern tropics**. The
675 detailed causes of this discrepancy are currently not clear to us, given the better matches
676 (correlation coefficients) we obtain between MOPITT total CO columns and modeled CO
677 columns. Potential causes could include model inaccuracies (possibly related to convection and/or
678 CO emissions and subsequent transport in this fairly narrow latitude region), or an alternate
679 explanation having to do with poorly understood limitations of the MLS data in this same region
680 (see the previous section).

681 The **temporal** variability that we have observed in the upper troposphere is difficult to fit
682 completely using standard linear regression, given the existence of short-term variability in the
683 troposphere (e.g., Dunkerton and Crum, 1995; Ziemke et al., 2015), as well as large episodic and
684 somewhat random enhancements in UT abundances (for CO in particular). Regarding this strong
685 CO variability, we note that ACE-FTS UT CO monthly zonal mean time series track those from
686 MLS, as shown by Park et al. (2021); **this helps to validate the UT time series and variability from**
687 **MLS**. The TCO interannual variability is also heavily influenced by ENSO (Ziemke and Chandra,
688 2003; Ziemke et al., 2010). We found that the annual, semi-annual, and ENSO terms dominate
689 the ozone variability in the tropical upper troposphere. The MLS UT ozone variations and their
690 relation to ENSO, in particular, were discussed by Oman et al. (2013), who showed patterns of
691 ozone sensitivity to ENSO at 147 hPa (their Figure 6) that resemble the ones we produced here
692 (Fig. 14(old16)) from analyses of MLS data over almost twice as long a period. Oman et al. (2013)
693 also found that the ENSO relationship for ozone could be simulated by a chemical climate model
694 driven by observed SSTs. The observed and matching simulated sensitivity coefficients imply
695 increased downwelling from the stratosphere and suppressed convection during El Niño periods
696 for regions of positive sensitivity (Chandra et al., 1998; Sudo and Takahashi, 2001; Oman et al.,
697 2013). We find here that the CO sensitivity to ENSO is much more spatially uniform in sign than
698 the O₃ sensitivity; UT O₃ generally increases toward the tropopause while CO decreases, leading
699 to opposite sensitivities to increased upwelling phase over the Pacific (Figs. 15 and 16). In some
700 regions, the CO sensitivity has the same sign as for ozone, and in other regions, it differs;
701 moreover, the model's UT CO sensitivity coefficient to ENSO seems to broadly match the

702 observational sensitivity from MLS, as it shows positive values throughout the tropics. These
703 different behaviors between tropical UT O₃ and CO seem to mainly reflect a stronger (and positive)
704 sensitivity to biomass burning events in the case of CO.

705
706 Our multiple linear regression analyses lead to an averaged zonal mean tropical UT O₃ trend
707 from MLS for 2005–2020 of $0.39 \pm 0.28 \text{ \%yr}^{-1}$ (or about $0.22 \pm 0.16 \text{ ppbv yr}^{-1}$), where the error
708 bars indicate uncertainties at the 2σ level. We obtain excellent agreement with the above result
709 from **the (averaged) CAM-chem-CEDS O₃ zonal mean trends** ($0.38 \pm 0.28 \text{ \%yr}^{-1}$) and somewhat
710 poorer agreement from the smaller **WACCM-CEDS trends** ($0.21 \pm 0.23 \text{ \%yr}^{-1}$). We also show that
711 the zonal mean **MLS O₃ tropical UT trend results** for different time period choices, with start and
712 end years adjusted by one or two years, do not significantly depart from the 2005–2020 results;
713 **there is more sensitivity to the choice of time period in the CAM-chem-CEDS trend results over**
714 **the southern tropics.**

715 The largest MLS-derived mapped O₃ tropical trends (up to $+1.4\% \text{ yr}^{-1}$) are observed over
716 Indonesia and East of that region, as well as over the northern Atlantic region. In terms of the
717 mapped model O₃ UT trends, they broadly match the MLS-based UT trends, albeit with somewhat
718 smaller variations. The significant model maxima over Southeast Asia and the North Atlantic are
719 similar to the significant MLS patterns in those regions. More qualitatively, the Indonesian region
720 displays smaller model O₃ trends than those derived from MLS data; parts of the western Pacific
721 region exhibit some negative trends in the MLS and model trends, but not with good spatial
722 correlation.

723 **The mapped MLS-based UT O₃ trends and TCO trends for the same period (see Fig. 11), based**
724 **on the analyses of Ziemke et al. (2019), provide good correlations in parts of the tropics, with**
725 **similar values and longitudinal patterns; however, the MLS UT O₃ trend maxima over the western**
726 **Pacific are symmetric about the equator, whereas the TCO maxima in that region are found in the**
727 **northern part only. Since the TCO measurement weighting does not favor the UT region, we would**
728 **not necessarily expect a really high correlation versus the MLS UT trends.**

729 We should also note that the MLS ozone profile trend detection capability lies within the most
730 stable among ozone sounders, based on the satellite and ground-based ozone intercomparison work
731 by Hubert et al. (2016). In addition, differences between stratospheric ozone columns from MLS
732 and the Aura Ozone Monitoring Instrument (OMI) exhibit no significant drift (Ziemke et al.,

733 2019), thus providing added confidence in the temporal stability of both measurement systems; we
734 expect a similar level of confidence in the stability of the MLS CO measurements, since CO is
735 retrieved using the same radiometer as the MLS standard ozone product.

736 The analyses by Wang et al. (2022) of the IAGOS commercial aircraft database for several
737 regions of the globe indicate that upper tropospheric O₃ values have increased from 1995–2017,
738 with some of the larger trends residing in the tropics. IAGOS-derived trends were previously
739 discussed by Cohen et al. (2018) for the 1994–2013 period, but with an emphasis on the extra-
740 tropics. The IAGOS trend analysis by Gaudel et al. (2020) for five tropical regions over 1994–
741 2016 gave positive UT trends in the range 0.3–1.3 % yr⁻¹, with an average value of 0.5 % yr⁻¹, and
742 largest values over Southeast Asia and Malaysia/Indonesia. As mentioned above, the MLS results
743 also show peak ozone trends over this general region. The above average trend agrees quite well
744 with the average tropical UT O₃ trends (0.39 ± 0.28 % yr⁻¹) we obtain from MLS, which provides
745 more uniform (and daily) tropical coverage. This seems to be unexpectedly good agreement, since
746 there are different sampling characteristics, regions, and time periods for IAGOS versus MLS;
747 given the time period differences, in particular, we should only consider this to be a loose
748 comparison. More detailed comparisons between MLS and IAGOS are difficult and beyond the
749 scope of this work, given the differences in coverage (and in the vertical and horizontal footprints)
750 between these measurement systems.

751 There have been large differences between past satellite-based tropospheric O₃ trends (Gaudel
752 et al., 2018). Leventidou et al. (2018) pointed out that tropical tropospheric ozone column trends
753 derived from a combination of European satellite measurements from 1996 to 2015 showed
754 regional increases as large as 1–2%yr⁻¹, with some negative trends over the oceans, but with
755 significant uncertainties as well (see also Heue et al., 2016, and Ebojie et al., 2016). The TCO
756 analyses by Ziemke et al. (2019) using combined OMI and MLS ozone columns showed that the
757 TCO trends are larger in the 2005–2016 time period than in the two decades before 2005; for the
758 2005–2016 period, the derived TCO trends in the tropics are about 0.4–0.7 % yr⁻¹ (see also Gaudel
759 et al., 2020). These two investigations found regional differences in the TCO trends, with maxima
760 over India, Southeast Asia, the eastern Pacific region, and the tropical Atlantic, while they obtained
761 near zero or slightly negative TCO trends over the Western Pacific. Similar TCO trends (based on
762 combined OMI and MLS data) were also given by Liu et al. (2022) for the slightly longer 2005–
763 2018 period.

764 Wang et al. (2022) showed that derived ozone trends from ozonesonde profiles agree broadly
765 with the IAGOS results, although the sonde spatio-temporal coverage is naturally more limited,
766 and there can be a fair amount of scatter in the trends between different sonde sites. Thompson et
767 al. (2021) observed significant seasonal variations in derived tropical ozonesonde trends (based on
768 data over the 1998-2019 period from the Southern Hemisphere Additional Ozonesondes, or
769 SHADOZ network); these authors noted that dynamical influences (besides emissions changes)
770 likely play a role in these tropical tropospheric trends, which average $0.1\text{--}0.4\ \text{yr}^{-1}$, but with trends
771 in certain regions/seasons (February to May in particular) as large as $1\text{--}2.5\ \text{yr}^{-1}$.

772 Zhang et al. (2016) and Wang et al. (2022) have ascribed the positive sign of post-2000 tropical
773 ozone trends to an equatorward redistribution of surface emissions over the years. Moreover, Wang
774 et al. (2022) discussed how increases in aircraft emissions of nitrogen oxides should also have
775 contributed to enhancements in UT ozone. The UT **zonal mean** model O_3 trends shown in our work
776 are **typically larger (by $\sim 30\text{--}50\%$)** in the NH tropics than in the SH tropics. This is also true for the
777 model simulation (also from CESM2) provided by Wang et al. (2022); these authors also point out
778 that uncertainties in estimates of ozone precursor emission inventories (including those for volatile
779 organic carbons species, or VOCs) may well contribute to differences between modeled and
780 observational ozone trends. We note that there are large differences (a range of a factor of two or
781 more) between the tropospheric ozone burden changes predicted by various global models in the
782 work by Wang et al. (2022). Liu et al. (2022) show that significant regional differences in ozone
783 column trends exist in their model results (using the NASA Goddard Earth Observing System
784 Chemistry Climate Model, GEOSCCM), with near zero trends over the tropical western Pacific;
785 their modeled TCO trend results underestimate the observed positive TCO trends. These authors
786 point to underestimates of ozone precursor emissions, notably for VOCs such as formaldehyde, as
787 a potential explanation for the model underestimates of some observed TCO increases (mostly in
788 the extra-tropics). While VOC source strengths might be difficult to invoke as a major source of
789 uncertainty for the tropical regions, other potential model issues (e.g., larger than currently
790 expected uncertainties in lightning-generated ozone in the tropical upper troposphere) may be
791 worth further consideration.

792 For the CO trends, the average tropical **MLS** UT trend is $-0.25 \pm 0.30\ \text{yr}^{-1}$, whereas the
793 corresponding trends from CAM-chem-CEDS and WACCM-CEDS are **close to zero** (0.0 ± 0.14
794 yr^{-1}) for this region; **these average trend results are statistically in agreement, even if the MLS**

795 CO trends tend to generally be more negative than the simulation results. However, the CAM-
796 chem-CAMS simulations (which use CAMS anthropogenic CO emissions, see sect. 2.2), yield
797 statistically significant positive average tropical UT CO trends ($+0.22 \pm 0.19 \text{ \%yr}^{-1}$). More
798 specifically, these simulated latitude-dependent trends are significantly different from the MLS
799 CO trends in the 12°N - 24°N latitude bins. Larger MLS CO abundances in 2020 explain why the
800 MLS CO UT trends are more negative if one stops the analyses in 2018 or 2019. The mapped
801 MLS CO trends in the UT are also negative, with the more statistically significant result (stronger
802 negative trends) occurring at 147 hPa. While there have not been any past decades-long trend
803 estimates for CO in the broad tropical UT region, our results yield somewhat smaller rates of
804 decrease than other trends mentioned in the Introduction, for example -0.5 to -2 \%yr^{-1} , based on
805 IAGOS UT data at northern midlatitudes (Cohen et al., 2018). The mapped model UT CO trends
806 obtained here confirm the zonal mean model results. Although the CEDS emissions have helped
807 to produce near zero or slightly negative UT tropical CO trends in both WACCM-CEDS and
808 CAM-chem-CEDS simulations, the MLS UT CO trends in the tropical UT are significantly more
809 negative than these model results. Column CO in the free troposphere has generally shown
810 decreasing trends since the turn of the century, typically between about -0.5 and -1.5 \%yr^{-1} , as
811 observed in particular by MOPITT and AIRS (Worden et al., 2013a, Strode et al., 2016; Buchholz
812 et al., 2021; Hedelius et al., 2021). Liu et al. (2022) presented a recent analysis of MOPITT CO
813 data from 2005–2018, along with tropospheric model comparisons to observed CO and O₃ time
814 series. These authors found (as shown here and described for MLS and ACE-FTS data by Park et
815 al., 2021) that their modeled and observational time series both exhibit large interannual
816 variability, with some of the largest interannual changes driven by El Niño events in 2006 and
817 2015 and related biomass burning and CO enhancements tied to droughts over the Indonesian
818 region (see also Logan et al., 2008; Zhang et al., 2011; Livesey et al., 2013; Worden et al., 2013b;
819 Park et al., 2013; Field et al., 2016). Liu et al. (2022) found that modeled CO column trends over
820 various regions of the globe were generally negative, although a lower latitude region (India)
821 exhibited a positive model trend. Jiang et al. (2017) provide some arguments (and other references)
822 pointing to flat biomass burning emission trends over Africa for the first 10–15 years since the
823 turn of the century. Not including the strong tropical anomaly caused by El Niño in 2015, they
824 infer a negative trend in global biomass burning emissions. Uncertainties in the temporal evolution
825 of OH (a major sink for CO) could also explain model CO trend issues. However, Jiang et al.

826 (2017) implied that changes in global OH abundances could not readily explain global CO
827 decreases, given constraints from methyl chloroform surface data (this species also having OH as
828 a major sink, as discussed by Montzka et al., 2011) and despite large uncertainties in OH,
829 especially during the last decade. Rather, these authors conclude that decreasing CO emissions
830 from anthropogenic and biomass burning sources are the main cause of tropospheric CO decreases,
831 although some regional increasing emission trends do exist. While a systematic model bias cannot
832 readily lead to a significant discrepancy in model trend estimates (in percent per year) versus
833 observations, time-dependent emission biases could (e.g., Gaubert et al., 2023). To first order, the
834 decreasing UT CO tropical trends derived from MLS for 2005–2020 agree with (but tend to be
835 smaller in magnitude than) total column CO trends discussed previously in the literature. As
836 discussed by others, some temporal non-linearity in CO trends may be responsible for some of the
837 differences between past tropospheric CO trend results over different periods.

838 We believe that further investigations into how well different models of O₃ and CO in the
839 tropical UT match the MLS UT trends in these species are warranted, to provide better
840 understanding of differences between models. There may still be adjustments to make to the
841 models regarding the assumed CO surface emissions, convection, and/or transport-related issues,
842 even though such detailed studies are beyond the scope of this paper. Indeed, biomass burning
843 from Africa or South America and emissions from Asia, followed by transport, can influence the
844 tropical upper tropospheric abundances of CO and O₃ (e.g., Tsvilidou et al., 2023). On a broader
845 note, the troposphere is a region where the relative importance of multiple factors might change
846 over the multi-decadal timescale of climate change; also, longer-term projections from (free
847 running) models may not be representative of changes from a particular decade or two (see Fiore
848 et al., 2022, regarding model ensemble projections). For example, while the MLS-derived ozone
849 trends in the tropical UT from 2005–2020 (a particular “snapshot” in time) compare fairly well
850 with other recent estimates of tropospheric ozone change over similar time periods, UT changes
851 may diverge from lower tropospheric changes in the longer-term. Long-term positive trends in the
852 influx of ozone from the stratosphere to the troposphere may be expected as a result of climate
853 change (Meul et al., 2018), probably with more of a significant influence on the extra-tropical
854 upper troposphere. Regarding the tropics, Stevenson et al. (2013) showed that a number of
855 chemistry climate model simulations of climate change scenarios yielded long-term ozone
856 decreases in the lower troposphere as a result of enhancements in water vapor (implying more

857 ozone destruction), but low latitude upper tropospheric ozone could be expected to rise, following
858 increased production from lightning. Finally, obtaining accurate enough observations of large-
859 scale tropospheric composition change over the long-term is expected to represent a continuing,
860 but worthy challenge.

861 **5 Conclusions**

862 [this concluding section will be added in step 2 (the final PDF file after step 2 was submitted, after accepting
863 all of the above detailed tracked changes), and is a shorter summary of the main results, not too much
864 different from the Abstract. Other changes in that final PDF are mainly the re-organization into O3 and CO
865 sections with little changed (we basically moved things around with only a few small cuts in text) in the
866 rest of the text.]

869 **Data availability.**

870 The MLS data files analyzed here come from the MLS Level 3 data sets (zonal mean and gridded
871 quantities), which are publicly available from the Goddard Earth Sciences Data and Information Services
872 Center (GES DISC) at <https://earthdata.nasa.gov/eosdis/daacs/gesdisc>.
873 The MOPITT Version 9 products are available from NASA through the Earthdata portal
874 (<https://earthdata.nasa.gov/>; https://asdc.larc.nasa.gov/project/MOPITT/MOP03JM_9; or directly from the
875 ASDC archive (<https://asdc.larc.nasa.gov/data/MOPITT/>). We used the following site,
876 ftp://ftp.seismo.nrcan.gc.ca/spaceweather/solar_flux/monthly_averages/solflux_monthly_average.txt to
877 obtain monthly means of the Canadian F10.7 solar flux measurements (Tapping, 2013); these series (see
878 <http://www.spaceweather.gc.ca>) were included in our regression fits. The QBO-related equatorial wind
879 monthly time series were obtained from the public website at <https://www.geo.fu-berlin.de/en/met/ag/strat/produkte/qbo>. The multivariate ENSO index dataset was obtained from the NOAA
880 Physical Sciences Laboratory website at <https://www.psl.noaa.gov/enso/mei/> (Wolter and Timlin, 2011;
881 Zhang et al., 2019). OMI/MLS tropospheric ozone data were obtained from the NASA satellite tropospheric
882 ozone webpage https://acd-ext.gsfc.nasa.gov/Data_services/cloud_slice/.

884
885 **Supplement.** Supplementary material is included as a separate file.

886
887 **Author contributions.** LF analyzed the MLS and model data for trends and variability, and prepared the
888 manuscript, along with contributions from all co-authors. DEK, CGB, and BG provided inputs for running

889 the model runs, as well as properly averaged and formatted outputs from the model, as well as pertinent
890 model-related comments and interpretation of results. JRZ provided TCO datasets and comments on the
891 manuscript. NJL, MJS, WGR, and others on the MLS team provided analyses and expertise to enable the
892 production of the Aura MLS data sets; NJL, MJS, and WGR also provided comments on the manuscript;
893 RAF provided programming assistance for the creation of the MLS data sets and for storage and analyses
894 of the MLS and model files.

895

896 **Competing interests.** The authors declare that they have no conflict of interest.

897

898 **Acknowledgments.** We are thankful to the whole MLS team (past and present) for their contributions over
899 the years to the MLS instrument, data, processing, and database management. **We very much acknowledge**
900 **the referees, who helped improve the initial manuscript with quite a list of useful and detailed comments.**
901 **We acknowledge the encouragement from Owen Cooper and Helen Worden to link our paper to the**
902 **TOAR-II Copernicus special issue; thanks also to Kai-Lan Chang for briefly reviewing aspects of our**
903 **statistical approach regarding the guidelines adopted for reporting TOAR-linked results. WACCM-CEDS**
904 is a component of the CESM, supported by the National Science Foundation (NSF). We acknowledge high-
905 performance computing support from Cheyenne (doi:10.5065/D6RX99HX) provided by NCAR's
906 Computational and Information Systems Laboratory, sponsored by the NSF. F10.7 data collection and
907 dissemination are supported by the National Research Council of Canada, with the participation of Natural
908 Resources Canada and support by the Canadian Space Agency. Work at the Jet Propulsion Laboratory,
909 California Institute of Technology, was performed under contract with the National Aeronautics and Space
910 Administration (80NM0018D0004). Copyright 2024. All rights reserved.

911

912 **Financial support.** LF and RAF were funded by the NASA Atmospheric Composition Modeling and
913 Analysis Program (ACMAP). NJL, MJS, and WGR (as well as LF) were supported by the Aura Microwave
914 Limb Sounder project. DEK, BG, and CGB were funded separately by NASA and NSF grants. Part of this
915 material is based on work supported by the National Center for Atmospheric Research, which is a major
916 facility sponsored by the National Science Foundation under Cooperative Agreement No. 1852977. The
917 NSF NCAR MOPITT project is supported by the National Aeronautics and Space Administration (NASA)
918 Earth Observing System (EOS) program.

919 **References**

- 920 Andela, N., Morton, D. C., Giglio, L., Chen, Y., van der Werf, G. R., Kasibhatla, P. S., DeFries, R. S., Collatz, G. J.,
921 Hantson, S., Kloster, S., Bachelet, D., Forrest, M., Lasslop, G., Li, F., Mangeon, S., Melton, J. R., Yue, C., and
922 Randerson, J. T.: A human-driven decline in global burned area, *Science*, 356(6345):1356-1362, doi:
923 [10.1126/science.aal4108](https://doi.org/10.1126/science.aal4108), 2017.
- 924 Bouarar, I., Gaubert, B., Brasseur, G. P., Steinbrecht, W., Doumbia, T., Tilmes, S., et al.: Ozone anomalies in the free
925 troposphere during the COVID-19 pandemic, *Geophys. Res. Lett.*, 48, e2021GL094204.
926 <https://doi.org/10.1029/2021GL094204>, 2021.
- 927 Bourassa, A. E., Degenstein, D. A., Randel, W. J., Zawodny, J. M., Kyrölä, E., McLinden, C. A., Sioris, C. E., and
928 Roth, C. Z.: Trends in stratospheric ozone derived from merged SAGE II and Odin-OSIRIS satellite observations,
929 *Atmos. Chem. Phys.*, 14, 6983-6994, <https://doi.org/10.5194/acp-14-6983-2014>, 2014.
- 930 Brasseur, G. P., Gupta, M., Anderson, B. E., Balasubramanian, S., Barrett, S., Duda, D., Fleming, G., Forster, P. M.,
931 Fuglestvedt, J., Gettelman, A., Halthore, R. N., Jacob, D., Jacobson, M. Z., Khodayari, A., Liou, K.-N., Lund, M.
932 T., Miake-Lye, R. C., Minnis, P., Olsen, S., Penner, J. E., Prinn, R., Schumann, U., Selkirk, H. B., Sokolov, A.,
933 Unger, N., Wolfe, P., Wong, H.-W., Wuebbles, D. W., Yi, B., Yang, P., and Zhou, C.: Impact of aviation on
934 climate, FAA's Aviation Climate Change Research Initiative (ACCRI) Phase II, *Bull. Amer. Met. Soc.*,
935 [10.1175/BAMS-D-13-00089.1](https://doi.org/10.1175/BAMS-D-13-00089.1), 2016.
- 936 Buchholz, B. R., Worden H. M., et al.: Air pollution trends measured from Terra: CO and AOD over industrial, fire-
937 prone, and background regions, *Remote Sensing of Environment*, 256, 112275,
938 <https://doi.org/10.1016/j.rse.2020.112275>, 2021.
- 939 Burkholder, J. B., Sander, S. P., Abbatt, J. P. D., Barker, J. R., Cappa, C., Crouse, J. D., Dibble, T. S., Huie, R. E.,
940 Kolb, C. E., Kurylo, M. J., Orkin, V. L., Percival, C. J., Wilmouth, D. M., and Wine, P. H.: Chemical kinetics and
941 photochemical data for use in atmospheric studies, Evaluation No. 19, JPL Publication 19-5, Jet Propulsion
942 Laboratory, California Institute of Technology, Pasadena, <http://jpldataeval.jpl.nasa.gov> (last access: 1 March
943 2022), 2019.
- 944 Calvo, N., Garcia, R. R., Randel, W. J., and Marsh, D.: Dynamical mechanism for the increase in tropical upwelling
945 in the lowermost tropical stratosphere during warm ENSO events, *J. Atmos. Sci.*, 67, 2331–2340,
946 <https://doi.org/10.1175/2010JAS3433.1>, 2010.
- 947 Chandra, S., Ziemke, J. R., Min, W., and Read, W. G.: Effects of 1997–1998 El Niño on tropospheric ozone and water
948 vapor, *Geophys. Res. Lett.*, 25(20), 3867– 3870, <https://doi.org/10.1029/98GL02695>, 1998.
- 949 Coddington, O., Lean, J., Pilewskie, P., Snow, M., and Lindholm, D.: A solar irradiance climate data record, *Bull.*
950 *Amer. Meteor. Soc.*, <https://doi.org/10.1175/BAMS-D-14-00265.1>, 2016.
- 951 Cohen, Y., Petetin, H., Thouret, V., Marécal, V., Josse, B., Clark, H., Sauvage, B., Fontaine, A., Athier, G., Blot, R.,
952 Boulanger, D., Cousin, J.-M., and Nédélec, P.: Climatology and long-term evolution of ozone and carbon
953 monoxide in the upper troposphere–lower stratosphere (UTLS) at northern midlatitudes, as seen by IAGOS from
954 1995 to 2013, *Atmos. Chem. Phys.*, 18, 5415–5453, <https://doi.org/10.5194/acp-18-5415-2018>, 2018.

955 Collins, W. J., Derwent, R. G., Garnier, B., C. E. Johnson, C. E., Sanderson, M. G., and Stevenson, D. S.: Effect of
956 stratosphere-troposphere exchange on the future tropospheric ozone trend, *J. Geophys. Res.*, 108, D12, 8528,
957 <https://doi.org/10.1029/2002JD002617>, 2003.

958 Cooper, O. R., Parrish, D. D., Ziemke, J. R., Balashov, N. V., Cupeiro, M., Galbally, I., Gilge, S., Horowitz, L., Jensen,
959 N. R., Lamarque, J.-F., Naik, V., Oltmans, S. J., Schwab, J., Shindell, D. T., Thompson, A. M., Thouret, V., Wang,
960 Y., and Zbinden, R. M.: Global distribution and trends of tropospheric ozone: An observation-based review,
961 *Elementa*, 2, 000029, <https://doi.org/10.12952/journal.elementa.000029>, 2014.

962 Crutzen, P. J.: A discussion of the chemistry of some minor constituents in stratosphere and troposphere, *Pure Appl.*
963 *Geophys.*, 106, 1385–1399, <https://doi.org/10.1007/BF00881092>, 1973.

964 Crutzen, P. J., and Andreae, M. O.: Biomass burning in the tropics: Impact on atmospheric chemistry and
965 biogeochemical cycles, *Science*, 250, 1669–1678, <https://doi.org/10.1126/science.250.4988.1669>, 1990.

966 Danabasoglu, G., Lamarque, J.-F., Bacmeister, J., Bailey, D. A., DuVivier, A. K., Edwards, J., Emmons, L. K.,
967 Fasullo, J., Garcia, R., Gettelman, A., Hannay, C., Holland, M. M., Large, W. G., Lauritzen, P. H., Lawrence, D.
968 M., Lenaerts, J. T. M., Lindsay, K., Lipscomb, W. H., Mills, M. J., Neale, R., Oleson, K. W., Otto-Bliesner, B.,
969 Phillips, A. S., Sacks, W., Tilmes, S., van Kampenhout, L., Vertenstein, M., Bertini, A., Dennis, J., Deser, C.,
970 Fischer, C., Fox-Kemper, B., Kay, J. E., Kinnison, D. E., Kushner, P. J., Larson, V. E., Long, M. C.,
971 Mickelson, S., Moore, J. K., Nienhouse, E., Polvani, L., Rasch, P. J., and Strand, W. G.: The Community Earth
972 System Model Version 2 (CESM2), *J. Adv. in Modeling Earth Systems*, 12,
973 <https://doi.org/10.1029/2019MS001916>, 2020.

974 Darnenov, A., and da Silva, A. M.: The Quick Fire Emissions Dataset (QFED) - Documentation of versions 2.1, 2.2
975 and 2.4, NASA/TM–2015–104606, 2015;38:183, <http://gmao.gsfc.nasa.gov/pubs/tm/>, 2014.

976 Davis, N. A., Callaghan, P., Simpson, I. R., and Tilmes, S.: Specified dynamics scheme impacts on wave-mean flow
977 dynamics, convection, and tracer transport in CESM2 (WACCM6), *Atmos. Chem. Phys.*, 22, 197–
978 214, <https://doi.org/10.5194/acp-22-197-2022>, 2022.

979 Deeter, M., Francis, G., Gille, J., Mao, D., Martínez-Alonso, S., Worden, H., Ziskin, D., Drummond, J., Commane,
980 R., Diskin, G., and McKain, K.: The MOPITT Version 9 CO product: sampling enhancements and validation,
981 *Atmos. Meas. Tech.*, 15, 2325–2344, <https://doi.org/10.5194/amt-15-2325-2022>, 2022.

982 Doherty, R. M., Stevenson, D. S., Johnson, C. E., Collins, W. J., and Sanderson, M. G.: Tropospheric ozone and El
983 Niño–Southern Oscillation: Influence of atmospheric dynamics, biomass burning emissions, and future climate
984 change, *J. Geophys. Res.-Atmos.*, 111, D19304, <https://doi.org/10.1029/2005JD006849>, 2006.

985 Duncan, B. N., Martin, R. V., Staudt, A. C., Yevich, R., and Logan, J. A.: Interannual and seasonal variability of
986 biomass burning emissions constrained by satellite observations, *J. Geophys. Res.-Atmos.*, 108, 4100,
987 <https://doi.org/10.1029/2002jd002378>, 2003.

988 Duncan, B. N., Strahan, S. E., Yoshida, Y., Steenrod, S. D., and Livesey, N.: Model study of the cross-tropopause
989 transport of biomass burning pollution, *Atmos. Chem. Phys.*, 7, 3713–3736, [https://doi.org/10.5194/acp-7-3713-](https://doi.org/10.5194/acp-7-3713-2007)
990 [2007](https://doi.org/10.5194/acp-7-3713-2007), 2007.

991 Dunkerton, T. J., and Crum, F. X.: Eastward propagating eastward ~2- to 15-day equatorial convection and its relation
992 to the tropical intraseasonal oscillation, *J. Geophys. Res.*, 100, D12, 25781–25790,
993 <http://dx.doi.org/10.1029/95JD02678>, 1995.

994 Ebojje, F., Burrows, J. P., Gebhardt, C., Ladstter-Weienmayer, A., von Savigny, C., Rozanov, A., Weber, M., and
995 Bovensmann, H.: Global tropospheric ozone variations from 2003 to 2011 as seen by SCIAMACHY, *Atmos.*
996 *Chem. Phys.*, 16, 417–436, <https://doi.org/10.5194/acp-16-417-2016>, 2016.

997 Efron, B., and Tibshirani, R.: *An Introduction to the Bootstrap*, Monographs on Statistics and Applied Probability 57,
998 Chapman and Hall, 1993.

999 **Emmons, L. K., Walters, S., Hess, P. G., Lamarque, J. F., Pfister, G. G., Fillmore, D., Granier, C. Guenther, A.**
1000 **Kinnison, D., Laepple, T., Orlando J., Tie, X., Tyndall, G., Wiedinmyer, C., Baughcum S. L., and Kloster,**
1001 **S.: Description and evaluation of the Model for Ozone and Related chemical Tracers, version 4 (MOZART-**
1002 **4). *Geoscientific Model Development*, 3(1), 43-67. <https://doi.org/10.5194/gmd-3-43-2010>.**

1003 Emmons, L. K., Schwantes, R. H., Orlando, J. J., Tyndall, G., Kinnison, D., Lamarque, J.-F., Marsh, D., Mills, M. J.,
1004 Tilmes, S., Bardeen, C., Buchholz, R. R., Conley, A., Gettelman, A., Garcia, R., Simpson, I., Blake, D. R.,
1005 Meinardi, S., and Pétron, G.: The Chemistry Mechanism in the Community Earth System Model version 2
1006 (CESM2), *Journal of Advances in Modeling Earth Systems*, 12, <https://doi.org/10.1029/2019MS001882>, 2020.

1007 Feely, R. A., Gammon, R. H., Taft, B. A., Pullen, P. E., Waterman, L. S., Conway, T. J., Gendron, J. F., and
1008 Wisegarver, D. P.: Distribution of chemical tracers in the eastern equatorial Pacific during and after the 1982–
1009 1983 El Niño/Southern Oscillation Event, *J. Geophys. Res.-Oceans*, 92, 6545–6558,
1010 <https://doi.org/10.1029/JC092iC06p06545>, 1987.

1011 Field, R. D., van der Werf, G. R., Fanin, T., Fetzer, E. J., Fuller, R., Jethva, H., Levy, R., Livesey, N. J., Luo, M.,
1012 Torres, O., and Worden, H. M.: Indonesian fire activity and smoke pollution in 2015 show persistent nonlinear
1013 sensitivity to El Niño-induced drought, *Proceedings of the National Academy of Sciences of the United States of*
1014 *America*, 113, 9204–9209, <https://doi.org/10.1073/pnas.1524888113>, 2016.

1015 Fiore, A. M., Hancock, S. E., Lamarque, J.-F., Correa, G. P., Chang, K.-L., Ru, M., Cooper, O., Gaudel, A., Polvani,
1016 L. M., Sauvage, B., and Ziemke, J. R.: Understanding recent tropospheric ozone trends in the context of large
1017 internal variability: a new perspective from chemistry-climate model ensembles, *Environ. Res.: Climate* 1 (2022)
1018 025008, <https://doi.org/10.1088/2752-5295/ac9cc2>, 2022.

1019 Froidevaux, L., Kinnison, D. E., Wang, R., Anderson, J., and Fuller, R. A.: Evaluation of CESM1 (WACCM) free-
1020 running and specified dynamics atmospheric composition simulations using global multispecies satellite data
1021 records, *Atmos. Chem. Phys.*, 19, 4783–4821, <https://doi.org/10.5194/acp-19-4783-2019>, 2019.

1022 Froidevaux, L., Kinnison, D. E., Santee, M. L., Millán, L. F., Livesey, N. J., Read, W. G., Bardeen, C. G., Orlando, J.
1023 J., and Fuller, R. A.: Upper stratospheric ClO and HOCl trends (2005–2020): Aura Microwave Limb Sounder and
1024 model results, *Atmos. Chem. Phys.*, 22, 4779–4799, <https://doi.org/10.5194/acp-22-4779-2022>, 2022.

1025 Gaubert, B., Worden, H. M., Arellano, A. F. J., Emmons, L. K., Tilmes, S., Barré, J., Martínez Alonso, S., Vitt, F.,
1026 Anderson, J. L., Alkemade, F., Houweling, S., and Edwards, D. P.: Chemical feedback from decreasing carbon
1027 monoxide emissions, *Geophys. Res. Lett.*, 44, 9985–9995, <https://doi.org/10.1002/2017GL074987>, 2017.

1028 Gaubert, B., Emmons, L. K., Raeder, K., Tilmes, S., Miyazaki, K., Arellano Jr., A. F., Elguindi, N., Granier, C., Tang,
1029 W., Barré, J., Worden, H. M., Buchholz, R. R., Edwards, D. P., Franke, P., Anderson, J. L., Saunio, M., Schroeder,
1030 J., Woo, J.-H., Simpson, I. J., Blake, D. R., Meinardi, S., Wennberg, P. O., Crouse, J., Teng, A., Kim, M.,
1031 Dickerson, R. R., He, H., Ren, X., Pusede, S. E., and Diskin, G. S.: Correcting model biases of CO in East Asia:
1032 impact on oxidant distributions during KORUS-AQ, *Atmos. Chem. Phys.*, 20, 14617–14647,
1033 <https://doi.org/10.5194/acp-20-14617-2020>, 2020.

1034 Gaubert, B., Edwards, D. P., Anderson, J. L., Arellano, A.F., Barré, J., Buchholz, R.R., Darras, S., Emmons, L.K.,
1035 Fillmore, D., Granier, C., et al.: Global Scale Inversions from MOPITT CO and MODIS AOD, *Remote Sens.* 15,
1036 4813, <https://doi.org/10.3390/rs15194813>, 2023.

1037 Gaudel, A., Cooper, O. R., Ancellet, G., Barret, B., Boynard, A., Burrows, J. P., Clerbaux, C., Coheur, P. F., Cuesta,
1038 J., Cuevas, E., Doniki, S., Dufour, G., Ebojje, F., Foret, G., Garcia, O., Granados-Muñoz, M. J., Hannigan, J. W.,
1039 Hase, F., Hassler, B., Huang, G., Hurtmans, D., Jaffe, D., Jones, N., Kalabokas, P., Kerridge, B., Kulawik, S.,
1040 Latter, B., Leblanc, T., Le Flochmoën, E., Lin, W., Liu, J., Liu, X., Mahieu, E., McClure-Begley, A., Neu, J. L.,
1041 Osman, M., Palm, M., Petetin, H., Petropavlovskikh, I., Querel, R., Rahpoe, N., Rozanov, A., Schultz, M. G.,
1042 Schwab, J., Siddans, R., Smale, D., Steinbacher, M., Tanimoto, H., Tarasick, D. W., Thouret, V., Thompson, A.
1043 M., Trickl, T., Weatherhead, E., Wespes, C., Worden, H. M., Vigouroux, C., Xu, X., Zeng, G., and Ziemke, J.:
1044 Tropospheric Ozone Assessment Report: Present-day distribution and trends of tropospheric ozone relevant to
1045 climate and global atmospheric chemistry model evaluation, *Elem. Sci. Anth.*, 6, 39,
1046 <https://doi.org/10.1525/elementa.291>, 2018.

1047 Gaudel, A., Cooper, O. R., Chang, K.-L., Bourgeois, I., Ziemke, J. R., Strode, S. A., Oman, L. D., Sellitto, P., Nédélec,
1048 P., Blot, R., Thouret, V., and Granier, C.: Aircraft observations since the 1990s reveal increases of tropospheric
1049 ozone at multiple locations across the Northern Hemisphere, *Sci. Adv.*, 6, eaba8272,
1050 <https://doi.org/10.1126/sciadv.aba8272>, 2020.

1051 Gelaro, R., McCarty, W., Suarez, M. J., Todling, R., Molod, A., Takacs, L., Randles, C. A., Darmenov,
1052 A., Bosilovich, M. G., Reichle, R., Wargan, K., Coy, L., Cullather, R., Draper, C., Akella, S., Buchard,
1053 V., Conaty, A., da Silva, A. M., Gu, W., Kim, G.-K., Koster, R., Lucchesi, R., Merkova, D., Nielsen, J.
1054 E., Partyka, G., Pawson, S., Putman, W., Rienecker, M., Schubert, S. D., Sienkiewicz, M., and Zhao, B.: The
1055 Modern-Era Retrospective Analysis for Research and Applications, Version 2 (MERRA2), *J. Clim.*, 30, 5419–
1056 5454, <https://doi.org/10.1175/JCLI-D-16-0758.1>, 2017.

1057 Gettelman, A., Mills, M. J., Kinnison, D. E., Garcia, R. R., Smith, A. K., Marsh, D. R., Tilmes, S., Vitt, F., Bardeen,
1058 C. G., McInerney, J., Liu, H.-L., Solomon, S. C., Polvani, L. M., Emmons, L. K., Lamarque, J.-F., Richter, J. H.,
1059 Glanville, A. S., Bacmeister, J. T., Phillips, A. S., Neale, R. B., Simpson, I. R., DuVivier, A. K., Hodzic, A., and
1060 Randel, W. J.: The Whole Atmosphere Community Climate Model version 6 (WACCM6), *J. Geophys. Res.-*
1061 *Atmos.*, 124, 12,380–12,403, <https://doi.org/10.1029/2019JD030943>, 2019.

1062 Gratz, L. E., Jaffe, D. A., and Hee, J. R.: Causes of increasing ozone and decreasing carbon monoxide in springtime
1063 at the Mt. Bachelor Observatory from 2004 to 2013, *Atm. Env.*, 109, 323–330,
1064 <http://dx.doi.org/10.1016/j.atmosenv.2014.05.076>, 2015.

1065 He, H., Stehr, J. W., Hains, J. C., Krask, D. J., Doddridge, B. G., Vinnikov, K. Y., Canty, T. P., Hosley, K. M.,
1066 Salawitch, R. J., Worden, H. M., and Dickerson, R. R.: Trends in emissions and concentrations of air pollutants in
1067 the lower troposphere in the Baltimore/Washington airshed from 1997 to 2011, *Atmos. Chem. Phys.* 13,
1068 <https://doi.org/10.5194/acp-13-7859-2013>, 2013.

1069 Hedelius, J. K., Toon, G. C., Buchholz, R. R., Iraci, L. T., Podolske, J. R., Roehl, C. M., et al.: Regional and urban
1070 column CO trends and anomalies as observed by MOPITT over 16 years, *J. Geophys. Res.-Atmos.*, 126,
1071 e2020JD033967, <https://doi.org/10.1029/2020JD033967>, 2021.

1072 Hegglin, M. I., and Shepherd, T. G.: Large Climate-Induced Changes in Ultraviolet Index and Stratosphere-to
1073 Troposphere Ozone Flux, *Nature Geoscience*, 2, 687–691, <http://dx.doi.org/10.1038/ngeo604>, 2009.

1074 Hegglin, M. I., Tegtmeier, S., Anderson, J., Bourassa, A. E., Brohede, S., Degenstein, D., Froidevaux, L., Funke, B.,
1075 Gille, J., Kasai, Y., Kyrölä, E. T., Lumpe, J., Murtagh, D., Neu, J. L., Pérot, K., Remsberg, E. E., Rozanov, A.,
1076 Toohey, M., Urban, J., von Clarmann, T., Walker, K. A., Wang, H.-J., Arosio, C., Damadeo, R., Fuller, R. A.,
1077 Lingenfelter, G., McLinden, C., Pendlebury, D., Roth, C., Ryan, N. J., Sioris, C., Smith, L., and Weigel, K.:
1078 Overview and update of the SPARC Data Initiative: comparison of stratospheric composition measurements from
1079 satellite limb sounders, *Earth Syst. Sci. Data*, 13, 1855–1903, <https://10.5194/essd-13-1855-2021>, 2021.

1080 Hess, P. G., and Zbinden, R.: Stratospheric impact on tropospheric ozone variability and trends: 1990–2009, *Atmos.*
1081 *Chem. Phys.*, 13, 649–674, <https://doi.org/10.5194/acp-13-649-20132013>, 2013.

1082 Heue, K.-P., Coldewey-Egbers, M., Delcloo, A., Lerot, C., Loyola, D., Valks, P., and van Roozendael, M.: *Atmos.*
1083 *Meas. Tech.*, 9, 5037–5051, <https://doi.org/10.5194/amt-9-5037-2016>, 2016.

1084 **Horr, P., Borken-Kleefeld, J., Caro, D., Dessens, O., Endresen, O., Gauss, M., Grewe, V., Hauglustaine, D., Isaksen,**
1085 **I. S. A., Jockel, P., Lelieveld, J., Myhre, G., Meijer, E., Olivie, D., Prather, M., Schnadt Poberaj, C., Shine, K. P.,**
1086 **Staelin, J., Tang, Q., van Aardenne, J., van Velthoven, P., and Sausen, R.: The impact of traffic emissions on**
1087 **atmospheric ozone and OH: results from QUANTIFY, *Atmos. Chem. Phys.*, 9, 3113–3136, [phys.net/9/3113/2009/](http://www.atmos-chem-
1088 <a href=), 2009.**

1089 Hsu, J. and Prather, M. J.: Is the residual vertical velocity a good proxy for stratosphere-troposphere exchange of
1090 ozone?, *Geophys. Res. Lett.*, 41, 9024–9032, <https://doi.org/10.1002/2014GL061994>, 2014.

1091 Huang, L., Fu, R., Jiang, J. H., Wright, J. S., and Luo, M.: Geographic and seasonal distributions of CO transport
1092 pathways and their roles in determining CO centers in the upper troposphere, *Atmos. Chem. Phys.*, 12, 4683–4698,
1093 <https://doi.org/10.5194/acp-12-4683-2012>, 2012.

1094 Huang, L., Fu, R., and Jiang, J. H.: Impacts of fire emissions and transport pathways on the interannual variation of
1095 CO in the tropical upper troposphere, *Atmos. Chem. Phys.*, 14, 4087–4099, [https://doi.org/10.5194/acp-14-4087-](https://doi.org/10.5194/acp-14-4087-2014)
1096 [2014](https://doi.org/10.5194/acp-14-4087-2014), 2014.

1097 Huang, L., Jiang, J. H., Murray, L. T., Damon, M. R., Su, H., and Livesey, N. J.: Evaluation of UTLS carbon monoxide
1098 simulations in GMI and GEOS-Chem chemical transport models using Aura MLS observations, *Atmos. Chem.*
1099 *Phys.*, 16, 5641–5663, <https://doi.org/10.5194/acp-16-5641-2016>, 2016.

1100 Hubert, D., Lambert, J.-C., Verhoelst, T., Granville, J., Keppens, A., Baray, J.-L., Bourassa, A. E., Cortesi, U.,
1101 Degenstein, D. A., Froidevaux, L., Godin-Beekmann, S., Hoppel, K. W., Johnson, B. J., Kyrölä, E., Leblanc, T.,

1102 Lichtenberg, G., Marchand, M., McElroy, C. T., Murtagh, D., Nakane, H., Portafaix, T., Querel, R., Russell III, J.
1103 M., Salvador, J., Smit, H. G. J., Stebel, K., Steinbrecht, W., Strawbridge, K. B., Stübi, R., Swart, D. P. J., Taha,
1104 G., Tarasick, D. W., Thompson, A. M., Urban, J., van Gijssel, J. A. E., Van Malderen, R., von der Gathen, P.,
1105 Walker, K. A., Wolfram, E., and Zawodny, J. M.: Ground-based assessment of the bias and long-term stability of
1106 14 limb and occultation ozone profile data records, *Atmos. Meas. Tech.*, 9, 2497–2534,
1107 <https://doi.org/10.5194/amt-9-2497-2016>, 2016.

1108 Jiang, J. H., Livesey, N. J., Su, H., Neary, L., McConnell, J. C., and Richards, N. A. D.: Connecting surface emissions,
1109 convective uplifting, and long-range transport of carbon monoxide in the upper troposphere: New observations
1110 from the Aura Microwave Limb Sounder, *Geophys. Res. Lett.*, 34, L18812, <https://doi.org/10.1029/2007gl030638>,
1111 2007.

1112 Jiang, Z., Worden, J. R., Worden, H., Deeter, M., Jones, D. B. A., Arellano, A. F., and Henze, D. K.: A 15-year record
1113 of CO emissions constrained by MOPITT CO observations, *Atmos. Chem. Phys.*, 17, 4565–4583,
1114 <https://doi.org/10.5194/acp17-4565-2017>, 2017.

1115 Jones, C. D., Collins, M., Cox, P. M., and Spall, S. A.: The Carbon Cycle Response to ENSO: A Coupled Climate–
1116 Carbon Cycle Model Study, *J. Climate*, 14, 4113–4129, [https://doi.org/10.1175/1520-
1117 0442\(2001\)014<4113:tcerte>2.0.CO;2](https://doi.org/10.1175/1520-0442(2001)014<4113:tcerte>2.0.CO;2), 2001.

1118 Kinnison, D. E., Brasseur, G. P., Walters, S., Garcia, R. R., Sassi, F., Boville, B. A., Marsh, D. Harvey, L., Randall,
1119 C., Randel, W., Lamarque, J. F., Emmons, L. K., Hess, Orlando, J., Tyndall, G., and Pan, L.: Sensitivity of
1120 chemical tracers to meteorological parameters in the MOZART-3 chemical transport model, *J. Geophys. Res.*,
1121 112, D20302, <https://doi.org/10.1029/2006JD007879>, 2007.

1122 Khalil, M. A. K., and Rasmussen, R. A.: The global cycle of carbon monoxide: trends and mass balance, *Chemosphere*,
1123 20, Nos. 1–2, pp. 227–242, [https://doi.org/10.1016/0045-6535\(90\)90098-E](https://doi.org/10.1016/0045-6535(90)90098-E), 1990.

1124 Kumar, A., Wu, S., Weise, M. F., Honrath, R., Owen, R. C., Helmig, D., Kramer, L., Val Martin, M., and Li, Q.: Free-
1125 troposphere ozone and carbon monoxide over the North Atlantic for 2001–2011, *Atmos. Chem. Phys.*, 13, 12537–
1126 12547, <https://doi.org/10.5194/acp-13-12537-2013>, 2013.

1127 Laken, B. A., and Shahbaz, T.: Satellite-Detected Carbon Monoxide Pollution during 2000–2012: Examining Global
1128 Trends and also Regional Anthropogenic Periods over China, the EU and the USA, *Climate*, 2014, 2, 1-16,
1129 <https://doi.org/10.3390/cli2010001>, 2014.

1130 Lee, D. S., Fahey, D. W., Skowron, A., Allen, M. R., Burkhardt, U., Chen, Q., Doherty, S. J., Freeman, S., Forster, P.
1131 M., Fuglestedt, J., Gettelman, A., De Leon, R. R., Lim, L. L., Lund, M. T., Millar, R. J., Owen, B., Penner, J. E.,
1132 Pitari, G., Prather, M. J., Sausen, R., and Wilcox, L. J.: The contribution of global aviation to anthropogenic climate
1133 forcing for 2000 to 2018, *Atmos. Env.*, 244, 117834, doi.org/10.1016/j.atmosenv.2020.117834, 2021.

1134 Leventidou, E., Weber, M., Eichmann, K.-U., Burrows, J. P., Heue, K.-P., Thompson, A. M., and Johnson, B. J.:
1135 Harmonisation and trends of 20-year tropical tropospheric ozone data, *Atmos. Chem. Phys.*, 18, 9189–9205,
1136 <https://doi.org/10.5194/acp-18-9189-2018>, 2018.

1137 Li, L., and Liu, Y.: Space-borne and ground observations of the characteristics of CO pollution in Beijing, 2000–2010,
1138 *Atmos. Env.*, 45, 2367–2372. <https://doi.org/10.1016/j.atmosenv.2011.02.026>, 2011.

1139 Liu, J., Logan, J. A., Murray, L. T., Pumphrey, H. C., Schwartz, M. J., and Megretskaia, I. A.: Transport analysis and
1140 source attribution of seasonal and interannual variability of CO in the tropical upper troposphere and lower
1141 stratosphere, *Atmos. Chem. Physics*, 13, 129–146. <https://doi.org/10.5194/acp-13-129-2013>, 2013.

1142 Liu, J., Strode, S. A., Liang, Q., Oman, L. D., Colarco, P. R., Fleming, E. L., Manyin, M. E., Douglass, A. R., Ziemke,
1143 J. R., Lamsal, L. N., and Li, C.: Change in tropospheric ozone in the recent decades and its contribution to global
1144 total ozone, *J. Geophys. Res.-Atmos.*, 127, e2022JD037170. <https://doi.org/10.1029/2022JD037170>, 2022.

1145 Livesey, N. J., and Read, W. G.: Direct retrieval of line-of-sight atmospheric structure from limb sounding
1146 observations, *Geophys. Res. Lett.*, 27, 891-894, <https://doi.org/10.1029/1999GL010964>, 2000.

1147 Livesey, N. J., Van Snyder, W., Read, W. G., and Wagner, P. A.: Retrieval algorithms for the EOS Microwave Limb
1148 Sounder (MLS), *IEEE Trans. Geosci. Remote Sens.*, 44, 1144-1155, <https://doi.org/10.1109/TGRS.2006.872327>,
1149 2006.

1150 Livesey, N. J., Filipiak, M. J., Froidevaux, L., Read, W. G., Lambert, A., Santee, M. L., Jiang, J. H., Waters, J. W.,
1151 Cofield, R. E., Cuddy, D. T., Daffer, W. H., Drouin, B. J., Fuller, R. A., Jarnot, R. F., Jiang, Y. B., Knosp, B. W.,
1152 Li, Q. B., Perun, V. S., Schwartz, M. J., Snyder, W. V., Stek, P. C., Thurstans, R. P., Wagner, P. A., Pumphrey, H.
1153 C., Avery, M., Browell, E. V., Cammas, J.-P., Christensen, L. E., Edwards, D. P., Emmons, L. K., Gao, R.-S., Jost,
1154 H.-J., Loewenstein, M., Lopez, J. D., Nédélec, P., Osterman, G. B., Sachse, G. W., and Webster, C. R.: Validation
1155 of Aura Microwave Limb Sounder O₃ and CO observations in the upper troposphere and lower stratosphere, *J.*
1156 *Geophys. Res.*, 113, D15S02, <https://doi.org/10.1029/2007JD008805>, 2008.

1157 Livesey, N. J., Logan, J. A., Santee, M. L., Waters, J. W., Doherty, R. M., Read, W. G., Froidevaux, L., and Jiang, J.
1158 H.: Interrelated variations of O₃, CO and deep convection in the tropical/subtropical upper troposphere observed
1159 by the Aura Microwave Limb Sounder (MLS) during 2004–2011, *Atmos. Chem. Phys.*, 13, 579–598,
1160 <https://doi.org/10.5194/acp-13-579-2013>, 2013.

1161 Livesey, N. J., Read, W. G., Wagner, P. A., Froidevaux, L., Santee, M. L., Schwartz, M. J., Lambert, A., Millan Valle,
1162 L. F., Pumphrey, H. C., Manney, G. L., Fuller, R. A., Jarnot, R. F., Knosp, B. W., and Lay, R. R.: EOS MLS
1163 Version 5.0x Level 2 and 3 data quality and description document, Tech. rep., Jet Propulsion Laboratory D-105336
1164 Rev. B, Jan. 30, 2022, <https://mls.jpl.nasa.gov/eos-aura-mls/documentation.php>, 2022.

1165 Logan, Jennifer A.: Tropospheric ozone: Seasonal behavior, trends, and anthropogenic influence, *J. Geophys. Res.-*
1166 *Atmos.*, 90, 10463–10482, <https://doi.org/10.1029/JD090iD06p10463>, 1985.

1167 Logan, J. A., Prather, M. J., Wofsy, S. C., and McElroy, M. B.: Tropospheric chemistry: a global perspective, *J.*
1168 *Geophys. Res.*, 86, 7210–7254, <https://doi.org/10.1029/JC086iC08p07210>, 1981.

1169 Logan, J. A., Megretskaia, I., Nassar, R., Murray, L. T., Zhang, L., Bowman, K. W., Worden, H. M., and Luo, M.:
1170 Effects of the 2006 El Niño on tropospheric composition as revealed by data from the Tropospheric Emission
1171 Spectrometer (TES), *Geophys. Res. Lett.*, 35, L03816, <https://doi.org/10.1029/2007GL031698>, 2008.

1172 McDuffie, E. E., Smith, S. J., O'Rourke, P., Tibrewal, K., Venkataraman, C., Marais, E. A., Zheng, B., Crippa, M.,
1173 Brauer, M., and Martin, R. V.: A global anthropogenic emission inventory of atmospheric pollutants from sector-
1174 and fuel-specific sources (1970–2017): an application of the Community Emissions Data System (CEDS), *Earth*
1175 *Syst. Sci. Data*, 12, 3413–3442, <https://doi.org/10.5194/essd-12-3413-2020>, 2020.

1176 Meinshausen, M., Vogel, E., Nauels, A., Lorbacher, K., Meinshausen, N., Etheridge, D. M., Fraser, P. J., Montzka, S.
1177 A., Rayner, P. J., Trudinger, C. M., Krumme, P. B., Beyerle, U., Canadell, J. G., Daniel, J. S., Enting, I. G., Law,
1178 R. M., Lunder, C. R., O'Doherty, S., Prinn, R. G., Reimann, S., Rubino, M., Velders, G. J. M., Vollmer, M. K.,
1179 Wang, R. H.-J., and Weiss, R.: Historical greenhouse gas concentrations for climate modelling (CMIP6),
1180 Geoscientific Model Development, 10(5), 2057–2116. <https://doi.org/10.5194/gmd-10-2057-2017>, 2017.

1181 Meinshausen, M., Nicholls, Z. R. J., Lewis, J., Gidden, M. J., Vogel, E., Freund, M., Beyerle, U., Gessner, C., Nauels,
1182 A., Bauer, N., Canadell, J. G., Daniel, J. S., John, A., Krummel, P. B., Luderer, G., Meinshausen, N., Montzka, S.
1183 A., Rayner, P. J., Reimann, S., Smith, S. J., van den Berg, M., Velders, G. J. M., Vollmer, M. K., and Wang, R.
1184 H. J.: The shared socio-economic pathway (SSP) greenhouse gas concentrations and their extensions to 2500,
1185 Geosci. Model Dev., 13, 3571–3605, <https://doi.org/10.5194/gmd-13-3571-2020>, 2020.

1186 Meul, S., Langematz, U., Kröger, P., Oberländer-Hayn, S., and Jöckel, P.: Future changes in the stratosphere-to-
1187 troposphere ozone mass flux and the contribution from climate change and ozone recovery, Atmos. Chem. Phys.,
1188 18, 7721–7738, <https://doi.org/10.5194/acp-18-7721-2018>, 2018.

1189 Miyazaki, K., Bowman, K., Sekiya, T., Takigawa, M., Neu, J. L., Sudo, K., Osterman, G., and Eskes, H.: Global
1190 tropospheric ozone responses to reduced NO_x emissions linked to the COVID-19 worldwide lockdowns, Science
1191 Advances, 7(24), eabf7460, <https://doi.org/10.1126/sciadv.abf7460>, 2021.

1192 Monks, P. S., Archibald, A. T., Colette, A., Cooper, O., Coyle, M., Derwent, R., Fowler, D., Granier, C., Law, K. S.,
1193 Mills, G. E., Stevenson, D. S., Tarasova, O., Thouret, V., von Schneidmesser, E., Sommariva, R., Wild, O., and
1194 Williams, M. L.: Tropospheric ozone and its precursors from the urban to the global scale from air quality to short-
1195 lived climate forcer, Atmos. Chem. Phys., 15, 8889–8973, <https://doi.org/10.5194/acp-15-8889-2015>, 2015.

1196 Montzka, S. A., Krol, M., Dlugokencky, E., Hall, B., Jöckel, P., and Lelieveld, J.: Small Interannual Variability of
1197 Global Atmospheric Hydroxyl, Science, 331, 67–69, <https://doi.org/10.1126/science.1197640>, 2011.

1198 Murray, L. T., Mickley, L. J., Kaplan, J. O., Sofen, E. D., Pfeiffer, M., and Alexander, B.: Factors controlling
1199 variability in the oxidative capacity of the troposphere since the Last Glacial Maximum, Atmos. Chem. Phys., 14,
1200 3589–3622, <https://doi.org/10.5194/acp-14-3589-2014>, 2014.

1201 Nassar, R., Logan, J. A., Megretskaja, I. A., Murray, L. T., Zhang, L., & Jones, D. B. A., Analysis of tropical
1202 tropospheric ozone, carbon monoxide, and water vapor during the 2006 El Niño using TES observations and the
1203 GEOS-Chem model, J. Geophys. Res.-Atmos., 114, D17304, <https://doi.org/10.1029/2009jd011760>, 2009.

1204 Neely, R. R., and Schmidt, A.: VolcanEESM: Global volcanic sulphur dioxide (SO₂) emissions database from 1850
1205 to present - Version 1.0., <https://doi.org/10.5285/76ebdc0b-0eed-4f70-b89e-55e606bcd568>, 2016.

1206 Neu, J. L., Flury, T., Manney, G. L., Santee, M. L., Livesey, N. J., and Worden, J.: Tropospheric ozone variations
1207 governed by changes in stratospheric circulation, Nat. Geosci., 7, 340–344, <https://doi.org/10.1038/ngeo2138>,
1208 2014.

1209 O'Neill, B. C., Tebaldi, C., van Vuuren, D. P., Eyring, V., Friedlingstein, P., Hurtt, G., Knutti, R., Kriegler, E.,
1210 Lamarque, J.-F., Lowe, J., Meehl, G. A., Moss, R., Riahi, K., and Sanderson, B. M.: The Scenario Model
1211 Intercomparison Project (Scenario MIP) for CMIP6, Geosci. Model Dev., 9, 3461–3482,
1212 <https://doi.org/10.5194/gmd-9-3461-2016>, 2016.

1213 Oman, L. D., Ziemke, J. R., Douglass, A. R., Waugh, D. W., Lang, C., Rodriguez, J. M., and Nielsen, J. E.: The
1214 response of tropical tropospheric ozone to ENSO, *Geophys. Res. Lett.*, 38, L13706,
1215 <https://doi.org/10.1029/2011gl047865>, 2011.

1216 Oman, L. D., Douglass, A. R., Ziemke, J. R., Rodriguez, J. M., Waugh, D. W., and Nielsen, J. E.: The ozone response
1217 to ENSO in Aura satellite measurements and a chemistry-climate simulation, *J. Geophys. Res.*, 118, 965–976,
1218 <https://doi.org/10.1029/2012jd018546>, 2013.

1219 Park, M., Randel, W. J., Kinnison, D. E., Emmons, L. K., Bernath, P. F., and Walker, K. A., Boone, C. D., and Livesey,
1220 N. J.: Hydrocarbons in the upper troposphere and lower stratosphere observed from ACE-FTS and comparisons
1221 with WACCM, *J. Geophys. Res.-Atmos.*, 118, 1964–1980, <https://doi.org/10.1029/2012JD018327>, 2013.

1222 Park, K., Wang, Z., Emmons, L. K., and Mak, J. E.: Variation of atmospheric CO, $\delta^{13}\text{C}$, and $\delta^{18}\text{O}$ at high northern
1223 latitude during 2004–2009: Observations and model simulations, *J. Geophys. Res.-Atmos.*, 120, 11,024–11,036,
1224 <https://doi.org/10.1002/2015JD023191>, 2015.

1225 Park, M., Worden, H. M., Kinnison, D. E., Gaubert, B., Tilmes, S., Emmons, L. K., Santee, M. L., Froidevaux, L.,
1226 and Boone, C. D.: Fate of pollution emitted during the 2015 Indonesian fire season, *J. Geophys. Res.-Atmos.*, 126,
1227 e2020JD033474, <https://doi.org/10.1029/2020JD033474>, 2021.

1228 Patel, A., Mallika, C., Chandrab, N., Patrab, P. K., Steinbacher, M., Revisiting regional and seasonal variations in
1229 decadal carbon monoxide variability: Global reversal of growth rate, *Science of the Total Environment*, 909,
1230 168476, <https://doi.org/10.1016/j.scitotenv.2023.168476>, 2024.

1231 Petzold, A., Thouret, V., Gerbig, C., Zahn, A., Brenninkmeijer, C. A. M., Gallagher, M., Hermann, M., Pontaud, M.,
1232 Ziereis, H., Boulanger, D., Marshall, J., Nédélec, P., Smit, H. G. J., Friess, U., Flaud, J.-M., Wahner, A., Cammas,
1233 J.-P., and Volz-Thomas, A.: Global-scale atmosphere monitoring by in-service aircraft – current achievements and
1234 future prospects of the European Research Infrastructure IAGOS, *Tellus B*, 67, 28452,
1235 <https://doi.org/10.3402/tellusb.v67.28452>, 2015.

1236 Price, C., and Rind, D.: A simple lightning parameterization for calculating global lightning distributions, *J. Geophys.*
1237 *Res.-Atmos.*, 97, 9919–9933, <https://doi.org/10.1029/92JD00719>, 1992.

1238 Price, C., Penner, J., and Prather, M.: NO_x from lightning: 1. Global distribution based on lightning physics, *J.*
1239 *Geophys. Res.-Atmos.*, 102(D5), 5929–5941. <https://doi.org/10.1029/96JD03504>, 1997.

1240 Randel, W. J., Park, M., Wu, F., and Livesey, N. J.: A large annual cycle in ozone above the tropical tropopause linked
1241 to the Brewer-Dobson circulation, *J. Atmos. Sci.*, 64, 4479–4488, <https://doi.org/10.1175/2007JAS2409.1>, 2007.

1242 Read, W. G., Shippony, Z., and Snyder, W. V.: The clear-sky unpolarized forward model for the EOS Aura microwave
1243 limb sounder (MLS), *IEEE Trans. Geosci. Remote Sens.*, 44, 1367-1379,
1244 <https://doi.org/10.1109/TGRS.2006.862267>, 2006.

1245 Riahi, K., van Vuuren, D. P., Kriegler, E., Edmonds, J., O'Neill, B. C., Fujimori, S., Bauer, N., Calvin, K., Dellink,
1246 R., Fricko, O., Lutz, W., Popp, A., Crespo Cuaresma, J., Samir, K. C., Leimbach, M., Jiang, L., Kram, T., Rao, S.,
1247 Emmerling, J., Ebi, K., Hasegawa, T., Havlik, P., Humpenöder, F., Da Silva, A., Smith, S., Stehfest, E., Bosetti,
1248 V., Eom, J., Gernaat, D., Masui, T., Rogelj, J., Strefler, J., Drouet, L., Krey, V., Luderer, G., Harmsen, M.,
1249 Takahashi, K., Baumstark, L., Doelman, J. C., Kainuma, M., Klimont, Z., Marangoni, G., Lotze-Campen, H.,

1250 Obersteiner, M., Tabeau, A., Tavoni, M.: The Shared Socioeconomic Pathways and their energy, land use, and
1251 greenhouse gas emissions implications: An overview, *Global Environ. Chang.*, 42, 1045–1068, 2017,
1252 <https://doi.org/10.1016/j.gloenvcha.2016.05.009>, 2017.

1253 Rodgers, C.: *Inverse Methods for Atmospheric Sounding: Theory and Practice*, Vol. 2 of Series on Atmospheric,
1254 Oceanic and Planetary Physics, World Scientific, Singapore, 2000.

1255 Rowlinson, M. J., Rap, A., Arnold, S. R., Pope, R. J., Chipperfield, M. P., McNorton, J., Forster, P., Gordon, H.,
1256 Pringle, K. J., Feng, W., Kerridge, B. J., Latter, B. L., and Siddans, R.: Impact of El Niño–Southern Oscillation on
1257 the interannual variability of methane and tropospheric ozone, *Atmos. Chem. Phys.*, 19, 8669–8686,
1258 <https://doi.org/10.5194/acp-19-8669-2019>, 2019.

1259 Schoeberl, M. R., Duncan, B. N., Douglass, A. R., Waters, J., Livesey, N., Read, W., and Filipiak, M.: The carbon
1260 monoxide tape recorder, *Geophys. Res. Lett.*, 33, L12811, <https://doi.org/10.1029/2006gl026178>, 2006.

1261 Schumann, U., and Huntrieser, H.: The global lightning-induced nitrogen oxides source, *Atmos. Chem. Phys.*, 7,
1262 3823–3907, <https://doi.org/10.5194/acp-7-3823-2007>, 2007.

1263 Soulié, A., Granier, C., Darras, S., Zilbermann, N., Doumbia, T., Guevara, M., Jalkanen, J.-P., Keita, S., Liousse, C.,
1264 Crippa, M., Guizzardi, D., Hoesly, R., and Smith, S. J.: Global anthropogenic emissions (CAM5-GLOB-ANT) for
1265 the Copernicus Atmosphere Monitoring Service simulations of air quality forecasts and reanalyses, *Earth Syst.*
1266 *Sci. Data*, 16, 2261–2279, <https://doi.org/10.5194/essd-16-2261-2024>, 2024.

1267 Souri, A. H., Choi, Y., Jeon, W., Woo, J.-H., Zhang, Q., and Kurokawa, J.: Remote sensing evidence of decadal
1268 changes in major tropospheric ozone precursors over East Asia, *J. Geophys. Res.-Atmos.*, 122, 2474–2492,
1269 <https://doi.org/10.1002/2016JD025663>, 2017.

1270 SPARC: The SPARC Data Initiative: Assessment of stratospheric trace gas and aerosol climatologies from satellite
1271 limb sounders, M. I. Hegglin and S. Tegtmeier (eds.), SPARC Report No. 8, WCRP-5/2017, available at
1272 www.sparc-climate.org/publications/sparc-reports/, 2017.

1273 Stein, O., M. G. Schultz, M. G., Bouarar, I., Clark, H., Huijnen, V., A. Gaudel, A., George, M., and Clerbaux, C.: On
1274 the wintertime low bias of Northern Hemisphere carbon monoxide found in global model simulations, *Atmos.*
1275 *Chem. Phys.*, 14, 9295–9316, <https://doi.org/10.5194/acp-14-9295-2014>, 2014.

1276 Steinbrecht, W., Kubistin, D., Plass-Dülmer, C., Davies, J., Tarasick, D. W., Gathen, P. v. d., Deckelmann, H., Jepsen,
1277 N., Kivi, R., Lyall, N., Palm, M., Notholt, J., Kois, B., Oelsner, P., Allaart, M., Piters, A., Gill, M., Van Malderen,
1278 R., Delcloo, A. W., Sussmann, R., Mahieu, E., Servais, C., Romanens, G., Stübi, R., Ancellet, G., Godin-
1279 Beekmann, S., Yamanouchi, S., Strong, K., Johnson, B., Cullis, P., Petropavlovskikh, I., Hannigan, J. W.,
1280 Hernandez, J.-L., Diaz Rodriguez, A., Nakano, T., Chouza, F., Leblanc, T., Torres, C., Garcia, O., Röhling, A. N.,
1281 Schneider, M., Blumenstock, T., Tully, M., Paton-Walsh, C., Jones, N., Querel, R., Strahan, S., Stauffer, R. M.,
1282 Thompson, A. M., Inness, A., Engelen, R., Chang, K.-L., and Cooper, O. R.: COVID-19 Crisis Reduces Free
1283 Tropospheric Ozone Across the Northern Hemisphere, *Geophys. Res. Lett.*, 48, e2020GL091987,
1284 <https://doi.org/10.1029/2020GL091987>, 2021.

1285 Stevenson, D. S., Young, P. J., Naik, V., Lamarque, J.-F., Shindell, D. T., Voulgarakis, A., Skeie, R. B., Dalsoren, S.
1286 B., Myhre, G., Berntsen, T. K., Folberth, G. A., Rumbold, S. T., Collins, W. J., MacKenzie, I. A., Doherty, R. M.,

1287 Zeng, G., van Noije, T. P. C., Strunk, A., Bergmann, D., Cameron-Smith, P., Plummer, D. A., Strode, S. A.,
1288 Horowitz, L., Lee, Y. H., Szopa, S., Sudo, K., Nagashima, T., Josse, B., Cionni, I., Righi, M., Eyring, V., Conley,
1289 A., Bowman, K. W., Wild, O., and Archibald, A.: Tropospheric ozone changes, radiative forcing and attribution
1290 to emissions in the Atmospheric Chemistry and Climate Model Intercomparison Project (ACCMIP), *Atmos.*
1291 *Chem. Phys.*, 13, 3063–3085, <https://doi.org/10.5194/acp-13-3063-2013>, 2013.

1292 Strode, S. A., Worden, H. M., Damon, M., Douglass, A. R., Duncan, B. N., Emmons, L. K., Lamarque, J.-F., Manyin,
1293 M., Oman, L. D., Rodriguez, J. M., Strahan, S. E., and Tilmes, S.: Interpreting space-based trends in carbon
1294 monoxide with multiple models, *Atmos. Chem. Phys.*, 16, 7285–7294, <https://doi.org/10.5194/acp-16-7285-2016>,
1295 2016.

1296 Sudo, K. and Takahashi, M.: Simulation of tropospheric ozone changes during 1997–1998 El Niño: Meteorological
1297 impact on tropospheric photochemistry, *Geophys. Res. Lett.*, 28, 4091–4094,
1298 <https://doi.org/10.1029/2001GL013335>, 2001.

1299 Sudo, K., Takahashi, M., and Akimoto, H.: Future changes in stratosphere-troposphere exchange and their impacts on
1300 future tropospheric ozone simulations, *Geophys. Res. Lett.*, 30, 24, 2256, <https://doi.org/10.1029/2003GL018526>
1301 , 2003.

1302 Tapping, K.F.: The 10.7 cm solar radio flux (F10.7), *Space Weather*, 11, 394-406, <https://doi.org/10.1002/swe.20064>,
1303 2013.

1304 Thompson, A. M., Doddridge, B. G., Witte, J. C., Hudson, R. D., Luke, W. T., Johnson, J. E., Johnson, B. J., Oltmans,
1305 S. J., and Weller, R.: A tropical Atlantic ozone paradox: Shipboard and satellite views of a tropospheric ozone
1306 maximum and wave-one in January–February 1999, *Geophys. Res. Lett.*, 27, 3317–3320,
1307 <https://doi.org/10.1029/1999GL011273>, 2000.

1308 Thompson, A. M., Witte, J. C., Oltmans, S. J., Schmidlin, F. J., Logan, J. A., Fujiwara, M., Kirchhoff, V. W. J., Posny,
1309 F., Coetzee, G. J. R., Hoegger, B., Kawakami, S., Ogawa, T., Fortuin, J. P. F., and Kelder, H. M.: Southern
1310 Hemisphere Additional Ozonesondes (SHADOZ) 1998–2000 tropical ozone climatology. 2. Tropospheric
1311 variability and the zonal wave-one, *J. Geophys. Res.-Atmos.*, 108(D2), 8241,
1312 <https://doi.org/10.1029/2002JD002241>, 2003.

1313 Thompson, A. M., Stauffer, R. M., Wargan, K., Witte, J. C., Kollonige, D. E., and Ziemke, J. R.: Regional and
1314 seasonal trends in tropical ozone from SHADOZ profiles: Reference for models and satellite products, *J. Geophys.*
1315 *Res.-Atmos.*, 126, e2021JD034691, <https://doi.org/10.1029/2021JD034691>, 2021.

1316 Tilmes, S., Hodzic, A., Emmons, L. K., Mills, M. J., Gettelman, A., Kinnison, D. E., Park, M., Lamarque, J.-F., Vitt,
1317 F., Shrivastava, M., Campuzano-Jost, P., Jimenez, J. L., and Liu, X.: Climate forcing and trends of organic
1318 aerosols in the Community Earth System Model (CESM2), *J. of Adv. in Modeling Earth Systems*, 11, 4323–4351,
1319 <https://doi.org/10.1029/2019MS001827>, 2019.

1320 Tsvilidou, M., Sauvage, B., Bennouna, Y., Blot, R., Boulanger, D., Clark, H., Le Flochmoën, E., Nédélec, P., Valérie
1321 Thouret, V., Wolff, P., and Barret, B.: Tropical tropospheric ozone and carbon monoxide distributions:
1322 characteristics, origins, and control factors, as seen by IAGOS and IASI, *Atmos. Chem. Phys.*, 23, 14039–14063,
1323 <https://doi.org/10.5194/acp-23-14039-2023>, 2023.

1324 Verma, S., Yadava, P. K., Lal, D. M., Mall, R. K., Kumar, H., and Payra, S.: Role of Lightning NO_x in Ozone
 1325 Formation: A Review, *Pure Appl. Geophys.*, <https://doi.org/10.1007/s00024-021-02710-5>, 2021.

1326 Voulgarakis, A., Marlier, M. E., Faluvegi, G., Shindell, D. T., Tsigaridis, K., and Mangeon, S.: Interannual variability
 1327 of tropospheric trace gases and aerosols: The role of biomass burning emissions, *J. Geophys. Res.-Atmos.*, 120,
 1328 7157–7173, <https://doi.org/10.1002/2014JD022926>, 2015.

1329 Wang, P.-H., Fishman, J., Harvey, V. L., and Hitchman, M. H.: Southern tropical upper tropospheric zonal ozone
 1330 wave-1 from SAGE II observations (1985–2002), *J. Geophys. Res.-Atmos.*, 111, D08305,
 1331 <https://doi.org/10.1029/2005JD006221>, 2006.

1332 Wang, H., Lu, X., Jacob, D. J., Cooper, O. R., Chang, K.-L., Li, K., Gao, M., Liu, Y., Sheng, B., Wu, K., Wu, T.,
 1333 Zhang, J., Sauvage, B., Nédélec, P., Blot, R., and Fan, S.: Global tropospheric ozone trends, attributions, and
 1334 radiative impacts in 1995–2017: an integrated analysis using aircraft (IAGOS) observations, ozonesonde, and
 1335 multi-decadal chemical model simulations, *Atmos. Chem. Phys.*, 22, 13753–13782, <https://doi.org/10.5194/acp-22-13753-2022>, 2022.

1337 Warner, J., Carminati, F., Wei, Z., Lahoz, W., and Attié, J.-L.: Tropospheric carbon monoxide variability from AIRS
 1338 under clear and cloudy conditions, *Atmos. Chem. Phys.*, 13, 12469–12479, <https://doi.org/10.5194/acp-13-12469-2013>, 2013.

1340 Waters, J., Froidevaux, L., Harwood, R., Jarnot, R., Pickett, H., Read, W., Siegel, P., Cofield, R., Filipiak, M., Flower,
 1341 D., Holden, J., Lau, G., Livesey, N., Manney, G., Pumphrey, H., Santee, M., Wu, D., Cuddy, D., Lay, R., Loo, M.,
 1342 Perun, V., Schwartz, M., Stek, P., Thurstans, R., Boyles, M., Chandra, S., Chavez, M., Chen, G.-S., Chudasama,
 1343 B., Dodge, R., Fuller, R., Girard, M., Jiang, J., Jiang, Y., Knosp, B., LaBelle, R., Lam, J., Lee, K., Miller, D.,
 1344 Oswald, J., Patel, N., Pukala, D., Quintero, O., Scaff, D., Snyder, V., Tope, M., Wagner, P., and Walch, M.: The
 1345 Earth Observing System Microwave Limb Sounder (EOS MLS) on the Aura satellite, *IEEE Transac. Geosci.*
 1346 *Remote Sens.*, 44, 5, <https://doi.org/10.1109/TGRS.2006.873771>, 2006.

1347 Witte, J. C., Schoeberl, M. R., Douglass, A. R., and Thompson, A. M.: The quasi-biennial oscillation in tropical ozone
 1348 from SHADOZ and HALOE, *Atmos. Chem. Phys.*, 8, 3929–3936, <https://doi.org/10.5194/acp-8-3929-2008>, 2008.

1349 Wolter, K., and Timlin, M. S.: El Niño/Southern Oscillation behaviour since 1871 as diagnosed in an extended
 1350 multivariate ENSO index (MEI.ext), *Intl. J. Climatology*, 31, 1074–1087, <https://doi.org/10.1002/joc.2336>, 2011.

1351 Worden, H. M., Deeter, M. N., Frankenberg, C., George, M., Nichitiu, F., Worden, J., Aben, I., Bowman, K. W.,
 1352 Clerbaux, C., Coheur, P. F., de Laat, A. T. J., Detweiler, R., Drummond, J. R., Edwards, D. P., Gille, J. C.,
 1353 Hurtmans, D., Luo, M., Martinez-Alonso, S., Massie, S., Pfister, G., and Warner, J. X.: Decadal record of satellite
 1354 carbon monoxide observations, *Atmos. Chem. Phys.*, 13, 837–850, <https://doi.org/10.5194/acp-13-837-2013>,
 1355 2013a.

1356 Worden, J., Wecht, K., Frankenberg, C., Alvarado, M., Bowman, K., Kort, E., Kulawik, S., Lee, M., Payne, V., and
 1357 Worden, H.: CH₄ and CO distributions over tropical fires during October 2006 as observed by the Aura TES
 1358 satellite instrument and modeled by GEOS-Chem, *Atmos. Chem. Phys.*, 13, 3679–3692,
 1359 <https://doi.org/10.5194/acp-13-3679-2013>, 2013b.

1360 Yoon, J., and Pozzer, A.: Model-simulated trend of surface carbon monoxide for the 2001–2010 decade, *Atmos.*
1361 *Chem. Phys.*, 14, 10465–10482, <https://doi.org/10.5194/acp-14-10465-2014>, 2014.

1362 Zhang, L., Li, Q. B., Jin, J., Liu, H., Livesey, N., Jiang, J. H., Mao, Y., Chen, D., Luo, M., and Chen, Y.: Impacts of
1363 2006 Indonesian fires and dynamics on tropical upper tropospheric carbon monoxide and ozone, *Atmos. Chem.*
1364 *Phys.*, 11, 10929–10946, <https://doi.org/10.5194/acp-11-10929-2011>, 2011.

1365 Zhang, S., Zhao, P., He, L., Yang, Y., Liu, B., He, W., Cheng, Y., Liu, Y., Liu, S., Hu, Q., Huang, C., Wu, Y., On-
1366 board monitoring (OBM) for heavy-duty vehicle emissions in China: Regulations, early-stage evaluation and
1367 policy recommendations, *Science of the Total Environment*, Vol. 731, 139045, ISSN 0048-9697,
1368 <https://doi.org/10.1016/j.scitotenv.2020.139045>, 2020.

1369 Zhang, T., Hoell, A., Perlwitz, J., Eischeid, J., Murray, D., Hoerling, M., and Hamill, T.: Towards Probabilistic
1370 Multivariate ENSO Monitoring, *Geophys. Res. Lett.*, 46, <https://doi.org/10.1029/2019GL083946>, 2019.

1371 Zhang, Y., Cooper, O. R., Gaudel, A., Thompson, A. M., Nédélec, P., Ogino, S.-Y., and West, J. J.: Tropospheric
1372 ozone change from 1980 to 2010 dominated by equatorward redistribution of emissions, *Nat. Geosci.*, 9, 875–879,
1373 <https://doi.org/10.1038/ngeo2827>, 2016.

1374 Zheng, B., Chevallier, F., Ciais, P., Yin, Y., Deeter, M. N., Worden, H. M., Wang, Y., Zhang, Q., and He, K.: Rapid
1375 decline in carbon monoxide emissions and export from East Asia between years 2005 and 2016, *Environ. Res.*
1376 *Lett.*, 13, 044007, <https://doi.org/10.1088/1748-9326/aab2b3>, 2018.

1377 Ziemke, J. R., and Chandra, S.: La Niña and El Niño–induced variabilities of ozone in the tropical lower atmosphere
1378 during 1970–2001, *Geophys. Res. Lett.*, 30, 3, 1142, <https://doi.org/10.1029/2002GL016387>, 2003.

1379 Ziemke, J. R., Chandra, S., Oman, L. D., and Bhartia, P. K.: A new ENSO index derived from satellite measurements
1380 of column ozone, *Atmos. Chem. Phys.*, 10, 3711–3721, <https://doi.org/10.5194/acp-10-3711-2010>, 2010.

1381 Ziemke, J. R., A. R. Douglass, A. R., L. D. Oman, L. D., S. E. Strahan, S. E., and B. N. Duncan, B. N.: Tropospheric
1382 ozone variability in the tropics from ENSO to MJO and shorter timescales, *Atmos. Chem. Phys.*, 15, 8037–8049,
1383 <https://doi.org/10.5194/acp-15-8037-2015>, 2015.

1384 Ziemke, J. R., Oman, L. D., Strode, S. A., Douglass, A. R., Olsen, M. A., McPeters, R. D., Bhartia, P. K., Froidevaux,
1385 L., Labow, G. J., Witte, J. C., Thompson, A. M., Haffner, D. P., Kramarova, N. A., Frith, S. M., Huang, L.-K.,
1386 Jaross, G. R., Sefitor, C. J., Deland, M. T., and Taylor, S. L.: Trends in global tropospheric ozone inferred from a
1387 composite record of TOMS/OMI/MLS/OMPS satellite measurements and the MERRA-2 GMI simulation, *Atmos.*
1388 *Chem. Phys.*, 19, 3257–3269, <https://doi.org/10.5194/acp-19-3257-2019>, 2019.

1389 Ziemke, J. R., Kramarova, N. A., Frith, S. M., Huang, L.-K., Haffner, D. P., and Wargan, K.: NASA satellite
1390 measurements show global-scale reductions in free tropospheric ozone in 2020 and again in 2021 during COVID-
1391 19, *Geophys. Res. Lett.*, 49, e2022GL098712, <https://doi.org/10.1029/2022GL098712>, 2022.

1392

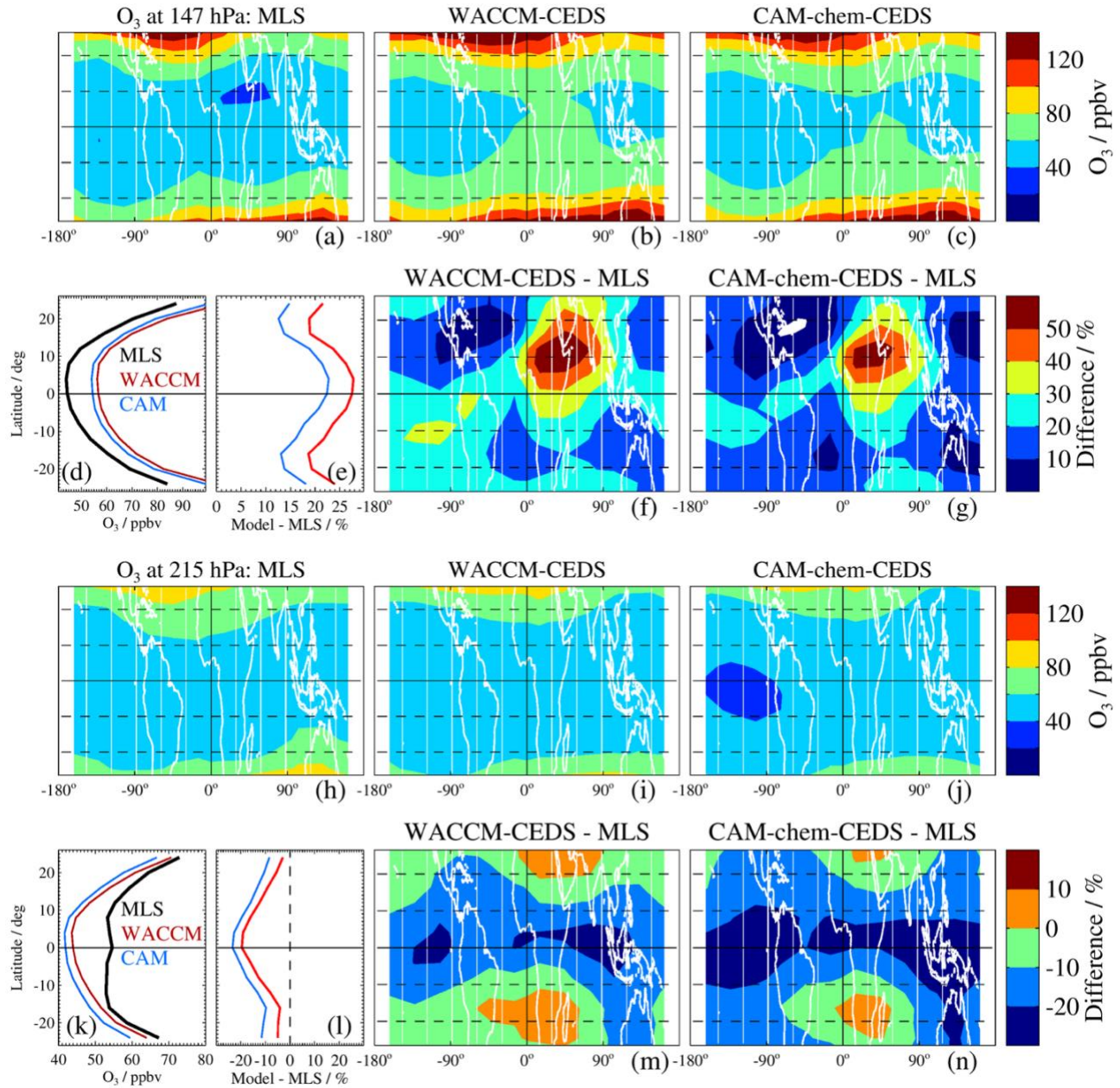
1393 **Table 1.** Some characteristics of the three chemistry climate model simulations used in this work.
 1394

Model Designation	Simulation Name	CO Anthropogenic Emissions Dataset	CO Biomass Burning dataset	Nudging timescale (hours)	Tropical Lightning NO _x (Tg N yr ⁻¹)	Aircraft NO _x Dataset ¹
CAM-chem	CAM-chem-CAMS	CAMS-GLOB-ANT_v5.1	QFED	6	2.34	Soulié et al. (2024)
CAM-chem	CAM-chem-CEDS	CEDSv2	QFED	6	2.34	Soulié et al. (2024)
WACCM	WACCM-CEDS	CEDSv2	QFED	12	2.78	CMIP6

1395
 1396 ¹For 2005–2014, the aircraft NO_x emissions for WACCM-CEDS and both CAM-chem model simulations
 1397 are identical. From 2015 onward, the WACCM-CEDS emissions are kept constant.
 1398

1399
 1400
 1401

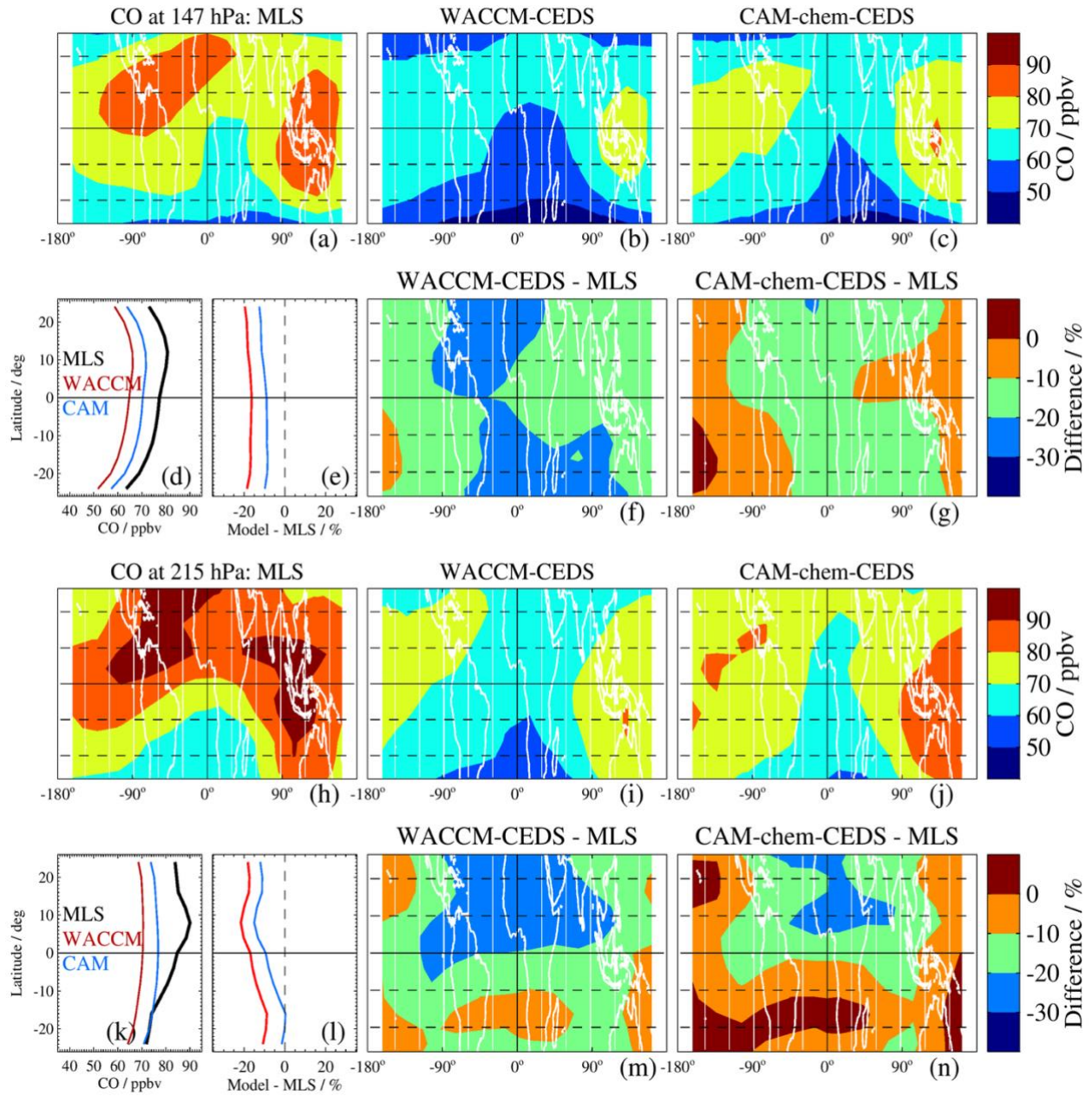
1402 **Figures**
 1403



1404
 1405

1406 **Figure 1.** Annually-averaged climatological comparisons between MLS and model ozone fields for 2005-
 1407 2020 at low latitudes (26°S to 26°N) at 147 hPa ((a) through (g)) and at 215 hPa ((h) through (n)). For 147
 1408 hPa: (a) climatological O₃ maps from MLS, (b) from WACCM-CEDS, (c) from CAM-chem-CEDS; (d)
 1409 shows the zonal mean climatology from the MLS data and both model simulations, with (e) giving the
 1410 differences in zonal means for both model simulations minus MLS (color-coded as shown in the (d) legend),
 1411 while (f) provides a difference map of the climatologies from WACCM-CEDS minus MLS, and (g) gives
 1412 the difference map for CAM-chem-CEDS minus MLS. Panels (h) through (n) provide the same information
 1413 as (a) through (g), but for 215 hPa. We note that in panels (d) and (k), CAM is an abbreviation for the CAM-
 1414 chem-CEDS simulation, and WACCM is an abbreviation for the WACCM-CEDS simulation.

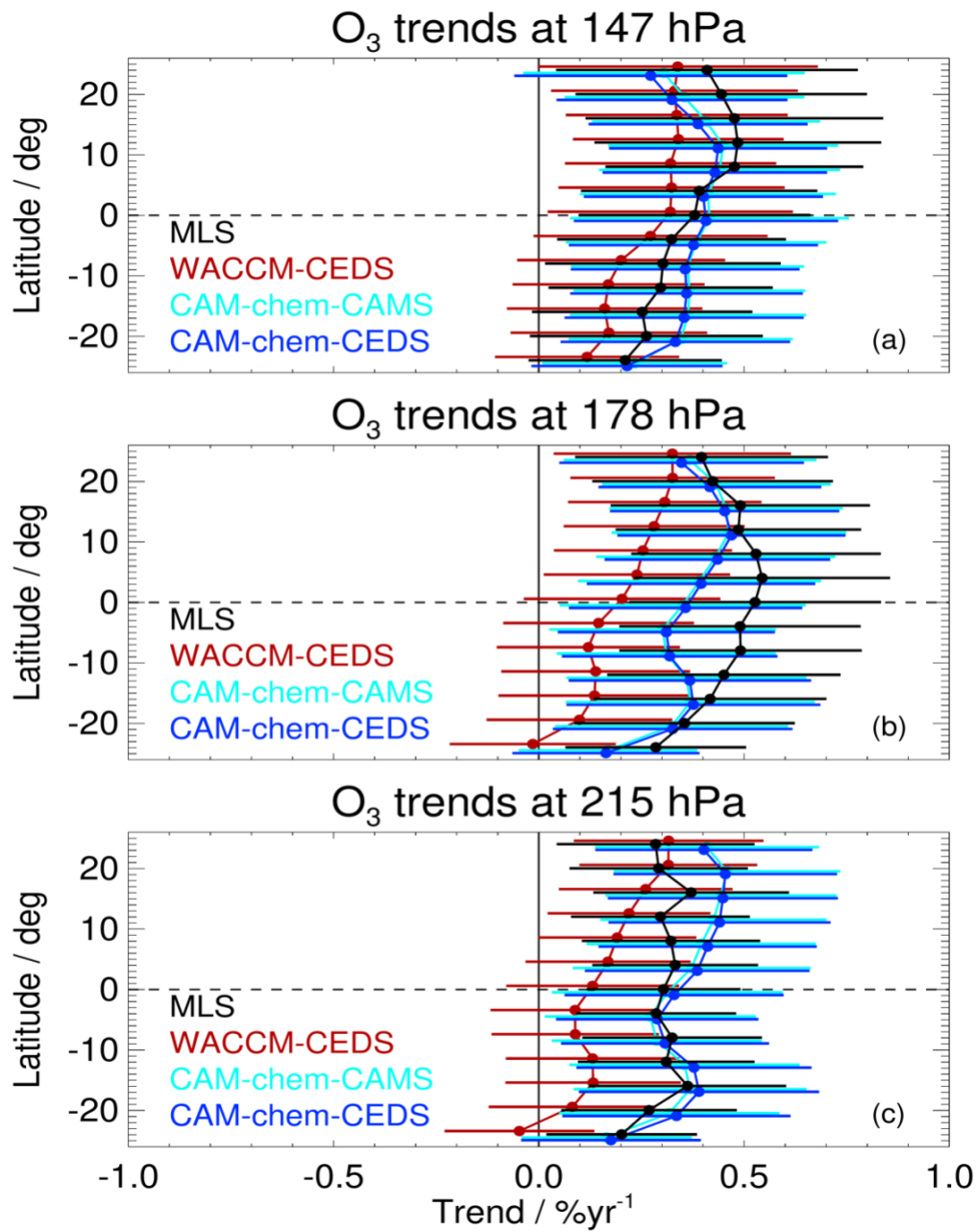
1415
1416



1417
1418
1419
1420
1421
1422
1423
1424
1425
1426
1427
1428

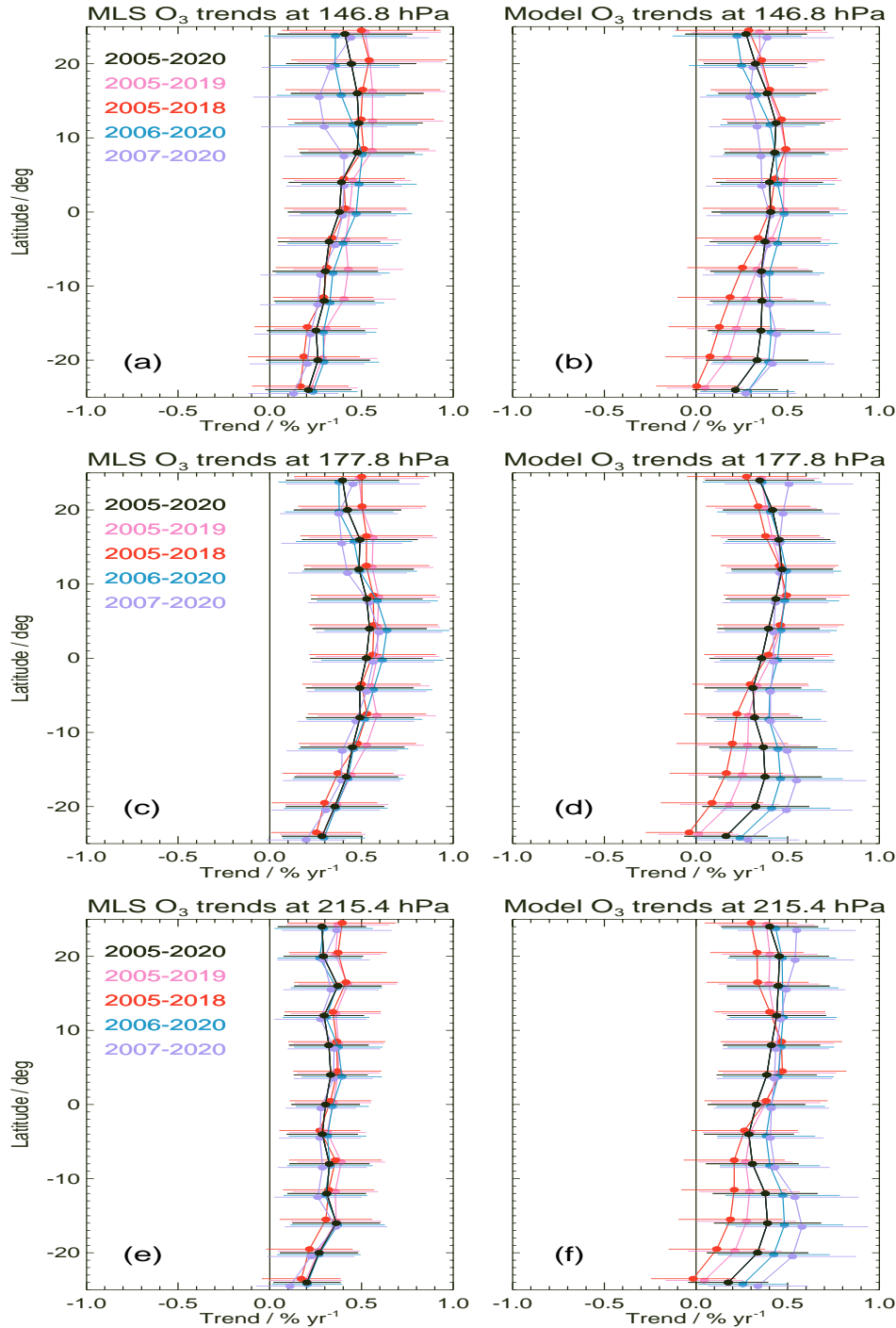
Figure 2. Same as Fig. 1, but for CO.

1429
1430
1431



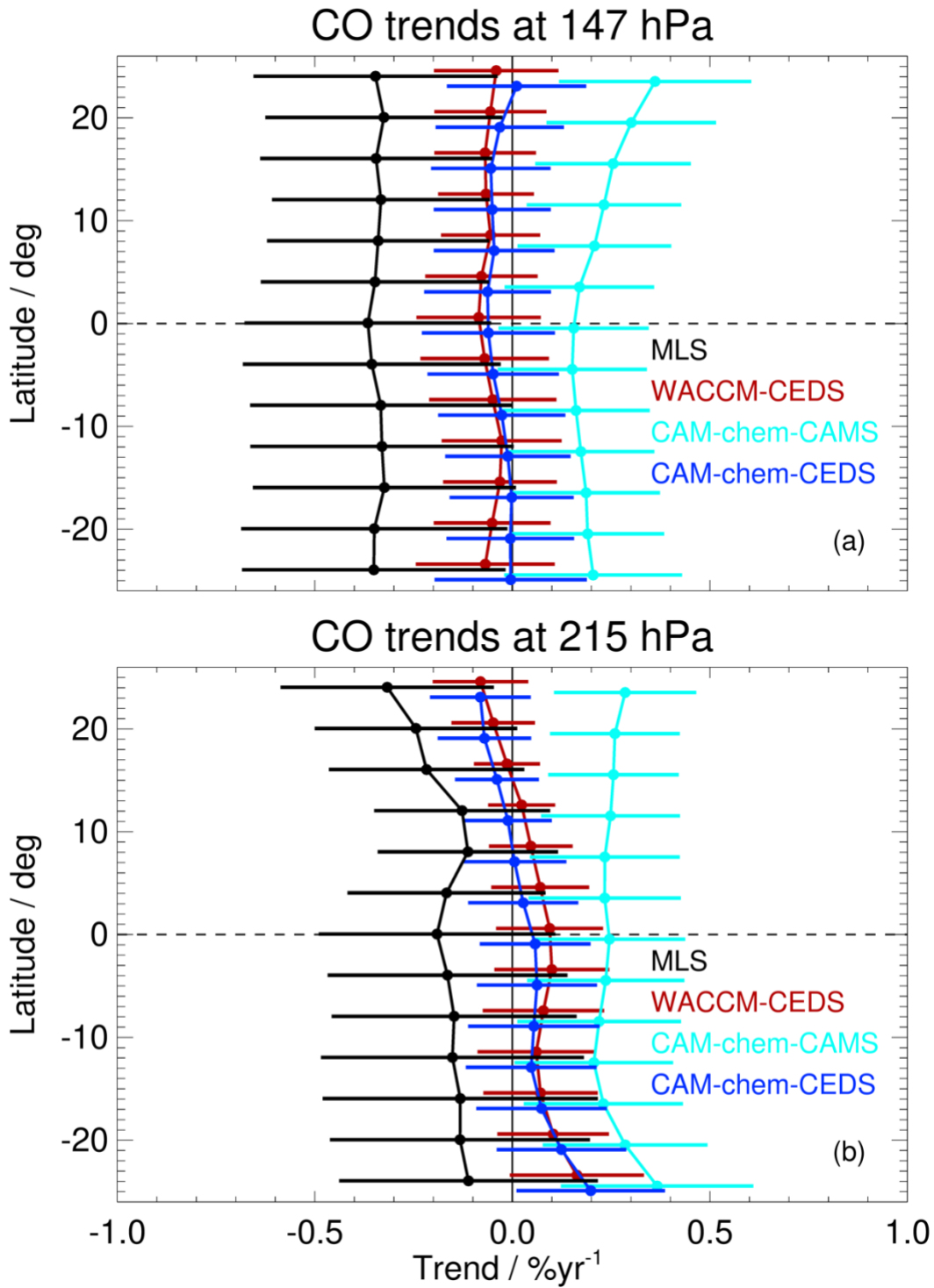
1432
1433
1434
1435
1436
1437
1438

Figure 3. Ozone zonal mean trends versus latitude in the tropical upper troposphere, for 2005–2020, based on MLR analyses of time series from MLS (black), WACCM-CEDS (red), CAM-chem-CAMS (cyan) and CAM-chem-CEDS (blue). Each row corresponds to a different pressure level: (a) for 147 hPa, (b) for 178 hPa, and (c) for 215 hPa, as labeled above each panel. Error bars give the uncertainties (2σ) in the estimated linear trends (see text for more details).



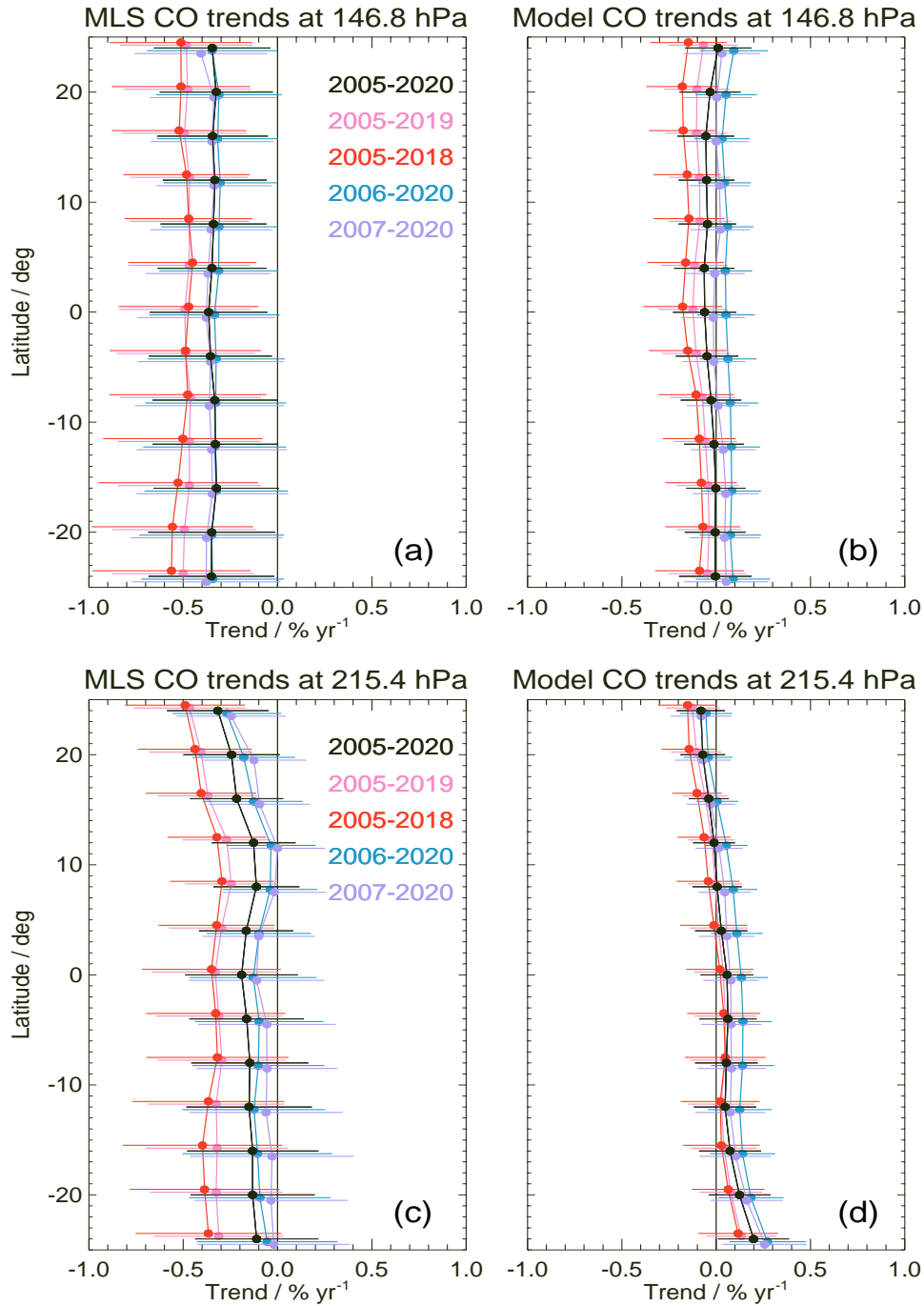
1439
 1440
 1441
 1442
 1443
 1444
 1445
 1446
 1447
 1448

Figure 4. Ozone zonal mean trends versus latitude in the tropical upper troposphere, with results from MLS data analyses shown in the left panels, and model results from CAM-chem-CEDS in the right panels. Each row corresponds to a different pressure level, as labeled. All panels show the trend sensitivity to the time period used in the regression fits. For example, black is used to show the period from 2005 through 2020; results from four other time periods are also shown, with the start or end year shifted by one or two years (see legend for the meaning of the various colors). The error bars given here represent the (2σ) uncertainties in the estimated linear trends.



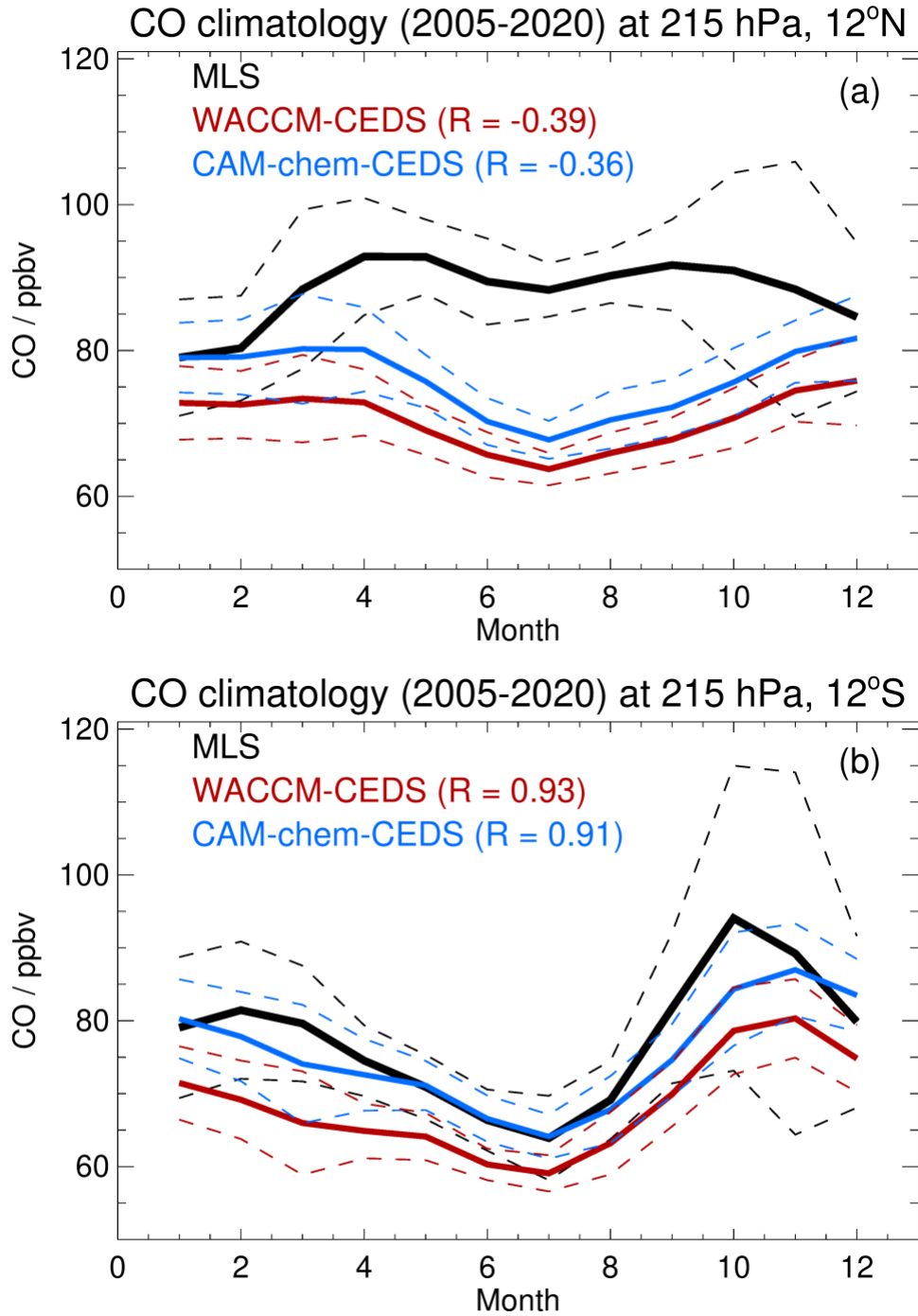
1450
1451
1452
1453
1454
1455
1456

Figure 5. Same as Fig. 3, but for CO zonal mean trends for (a) 147 hPa, and (b) 215 hPa.



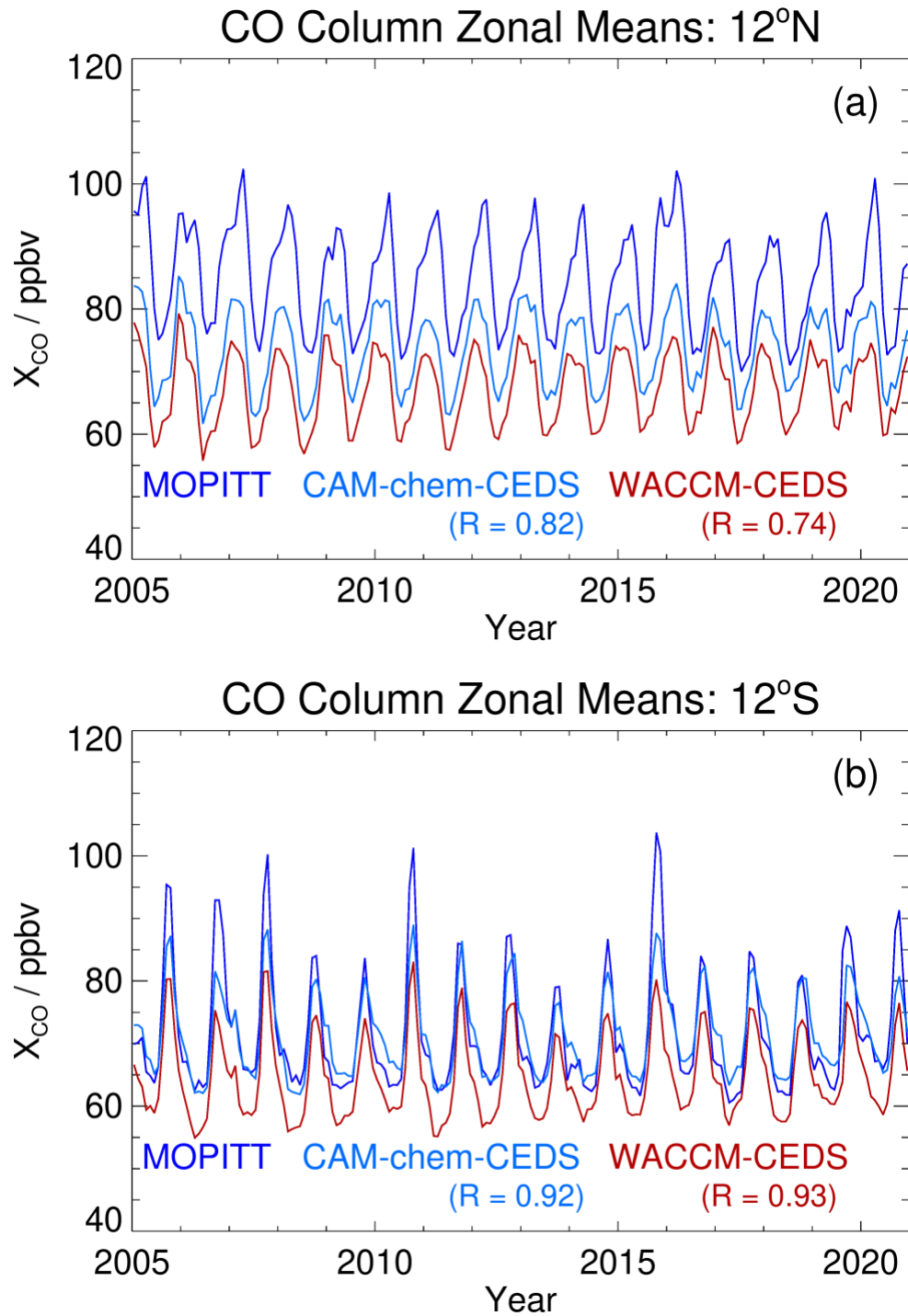
1457
 1458
 1459
 1460
 1461
 1462
 1463
 1464
 1465
 1466
 1467

Figure 6. Same as Fig. 4, but for CO tropical zonal mean trends from MLS and CAM-chem-CEDS at the MLS CO UT retrieval levels of 147 and 215 hPa.



1469
1470
1471
1472
1473
1474
1475
1476
1477

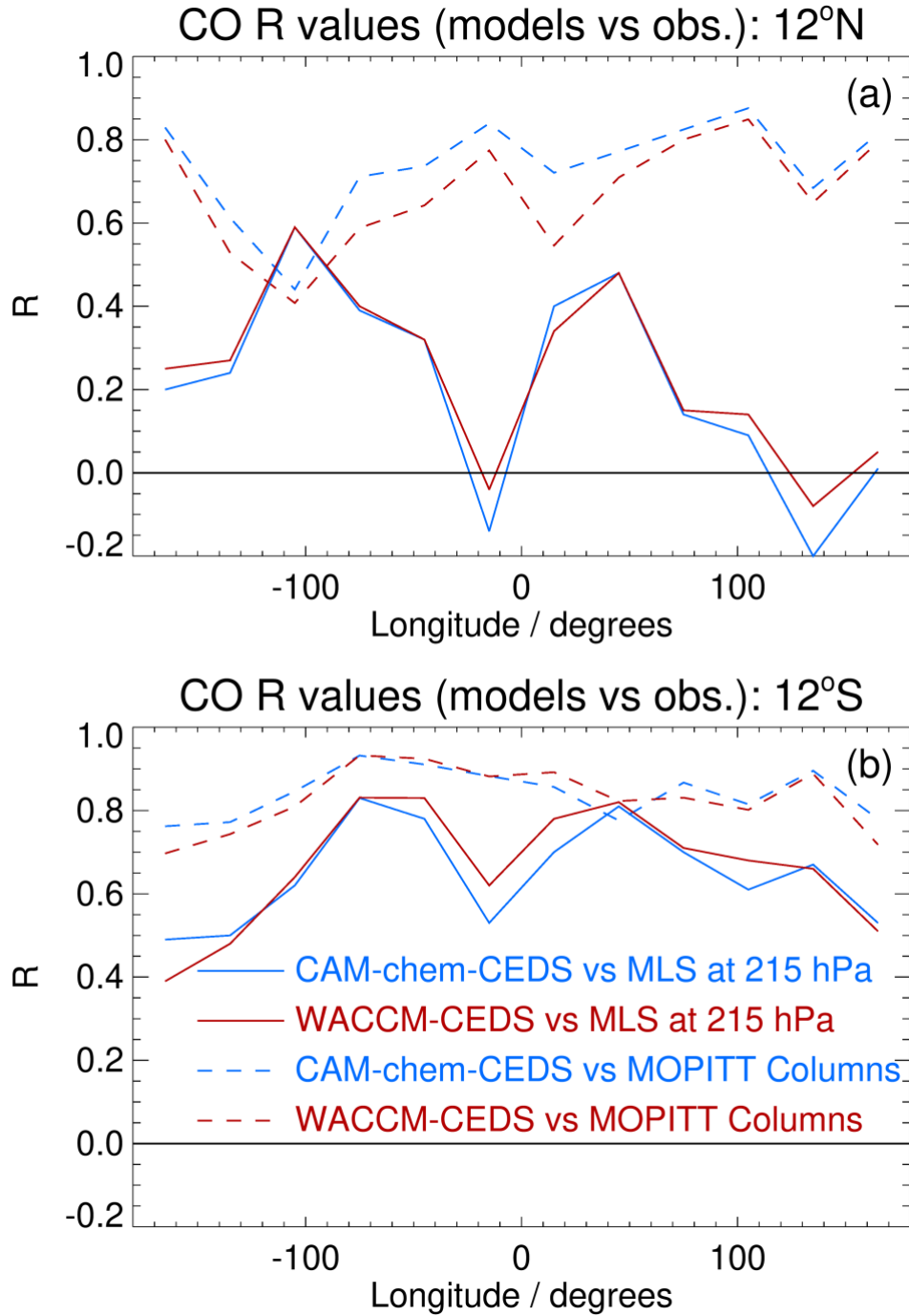
Figure 7(old9). CO climatology at 215 hPa (using the 2005–2020 period) from MLS, WACCM-CEDS, and CAM-chem-CEDS for 4°-wide latitude bins centered at (a) 12°N and (b) 12°S. The thick solid lines represent the mean values from MLS (black), WACCM-CEDS (red) and CAM-chem-CEDS (blue), with corresponding variability estimates (twice the standard deviations) given by the colored dashed lines about each mean.



1479
 1480
 1481
 1482
 1483
 1484
 1485

Figure 8(old10). CO column comparisons between zonal mean time series from MOPITT (purple) X_{CO} (see text) and from CAM-chem-CEDS (blue) and WACCM-CEDS (red) for 4°-wide latitude bins centered at (a) 12°N and (b) 12°S.

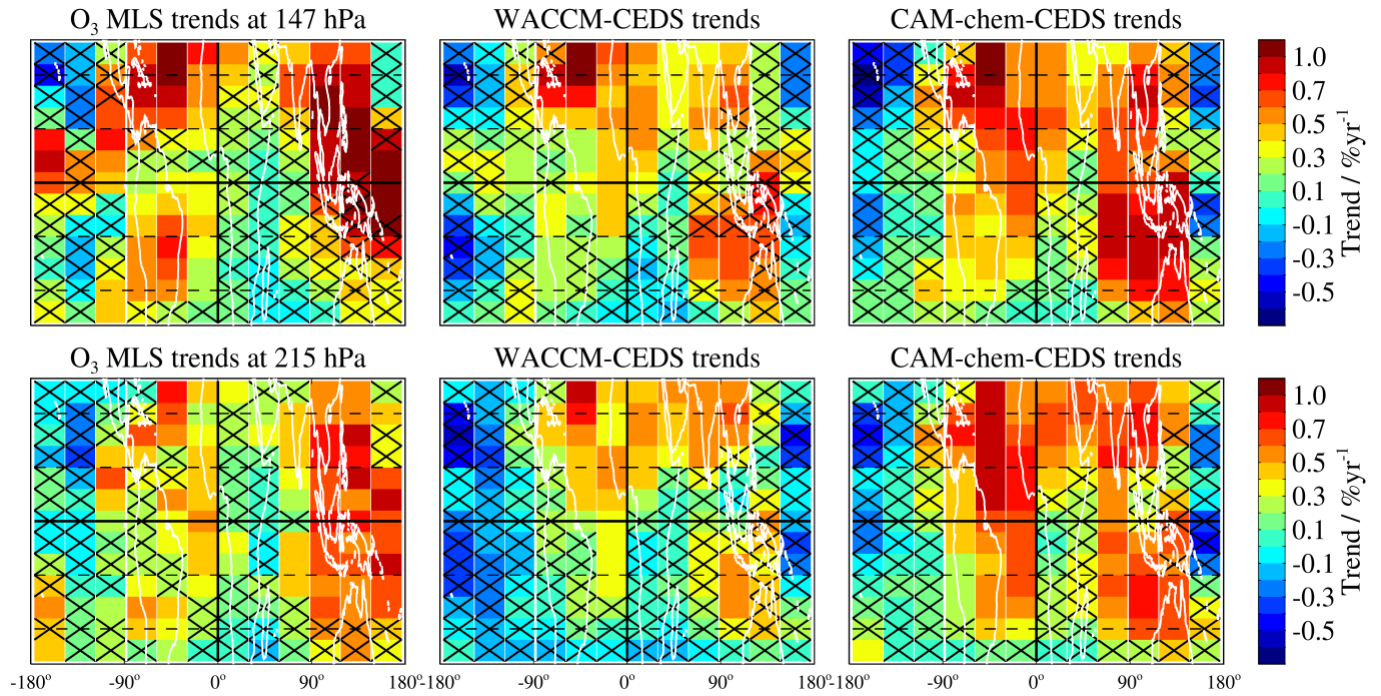
1486
1487



1488
1489
1490
1491
1492
1493
1494

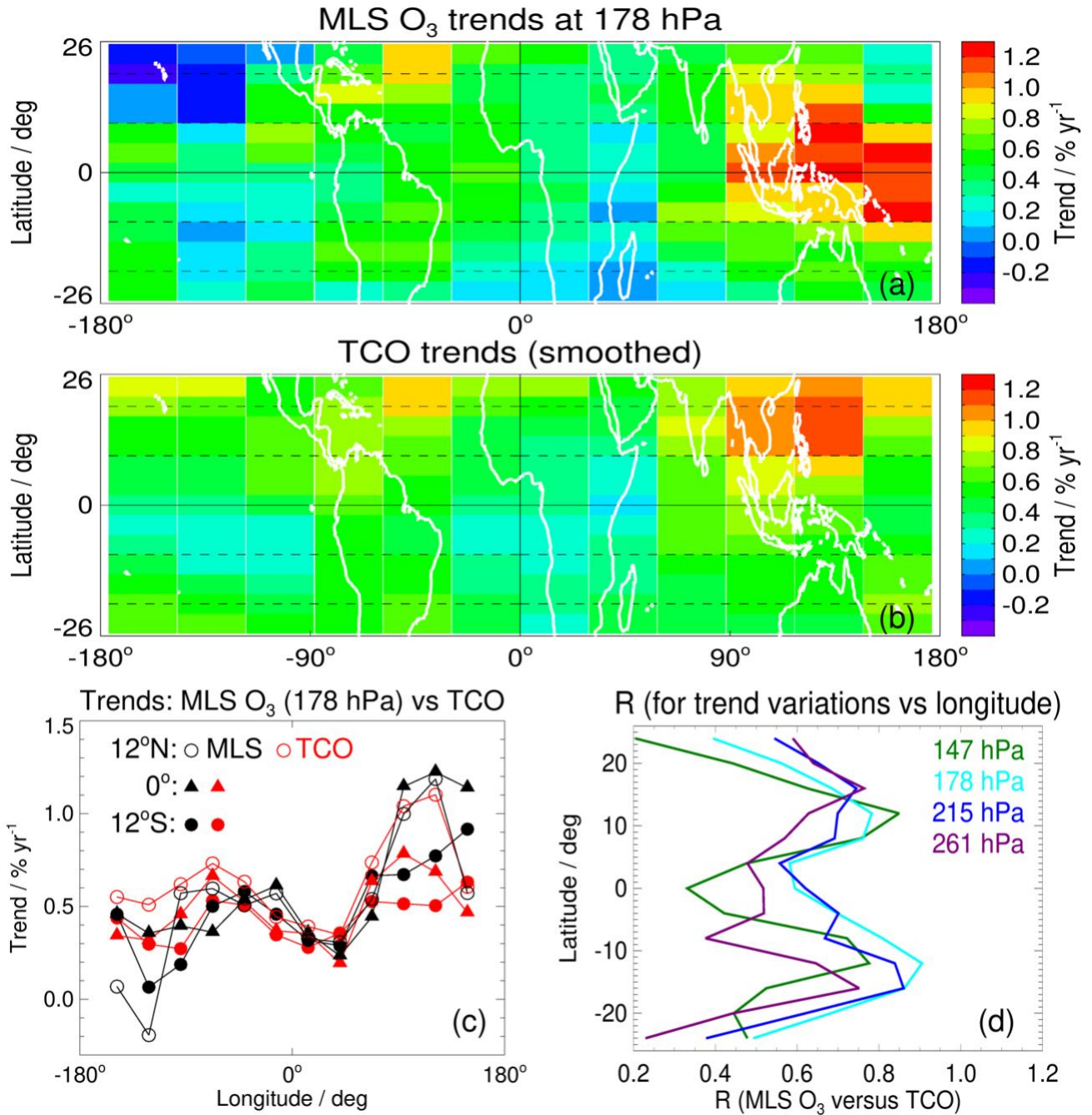
Figure 9(old11). Correlation coefficient values (R) for the zonal mean time series from the model CO columns (CAM-chem-CEDS in blue, WACCM-CEDS in red) versus MOPITT columns (dashed) and from the same two models' CO mixing ratios versus MLS CO at 215 hPa (solid) for 4°-wide latitude bins centered at (a) 12°N and (b) 12°S.

1495
1496



1497
1498
1499
1500
1501
1502
1503
1504

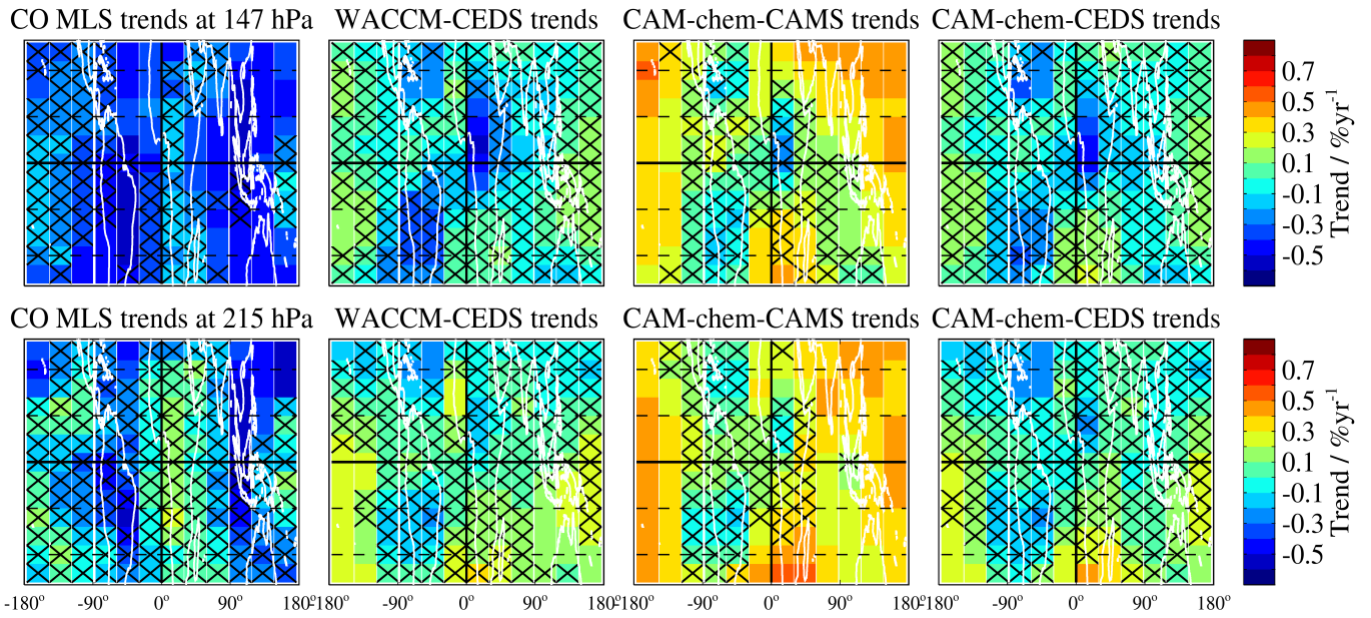
Figure 10(old12). Maps of upper tropospheric O₃ trends (% yr⁻¹) in the tropics for 147 hPa (top row) and 215 hPa (bottom row); the latitude range is from 26°S to 26°N, with maps all centered on the Greenwich meridian. MLS trends (left column) are compared to trends from **WACCM-CEDS** (middle column) and CAM-chem-CEDS (right column). Black crosses show grid boxes for which the trend estimate is not significantly different from zero (based on our 2 σ error estimates).



1505
 1506
 1507
 1508
 1509
 1510
 1511
 1512
 1513
 1514
 1515

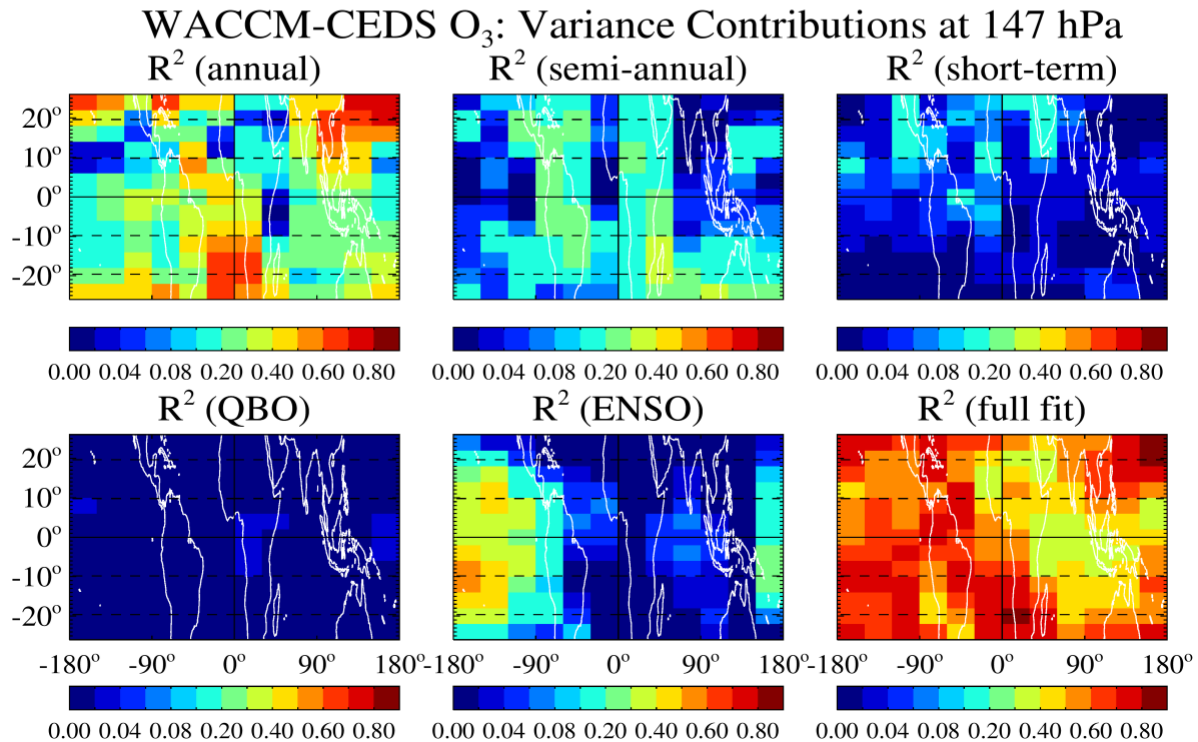
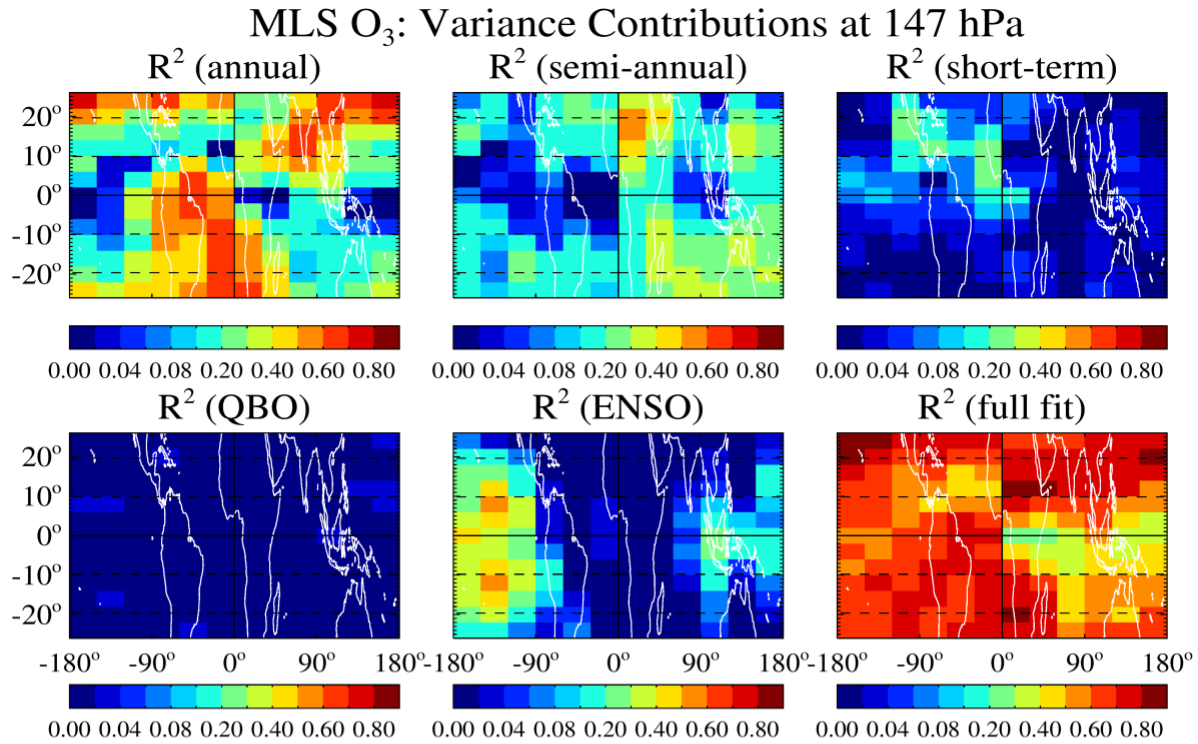
Figure 11(old13). (a) The top map shows MLS ozone trends (2005–2020) at 178 hPa, (b) the bottom map displays horizontally-smoothed tropospheric column ozone trends for the same time period, following the analyses of Ziemke et al. (2019), (c) cross sections of the above mapped trends in 4°-wide latitude bins centered at 12°N, 0°, and 12°S (see legend) for MLS (black) and TCO (red), and (d) correlation coefficient values R (on the x axis) between the MLS ozone trends at different pressures (see legend) and the TCO trends as a function of longitude, at different tropical latitudes (y axis). This panel provides a broader picture of the trend correlations, which exhibit a minimum near the Equator and maxima near 12°S and 12°N.

1516
1517



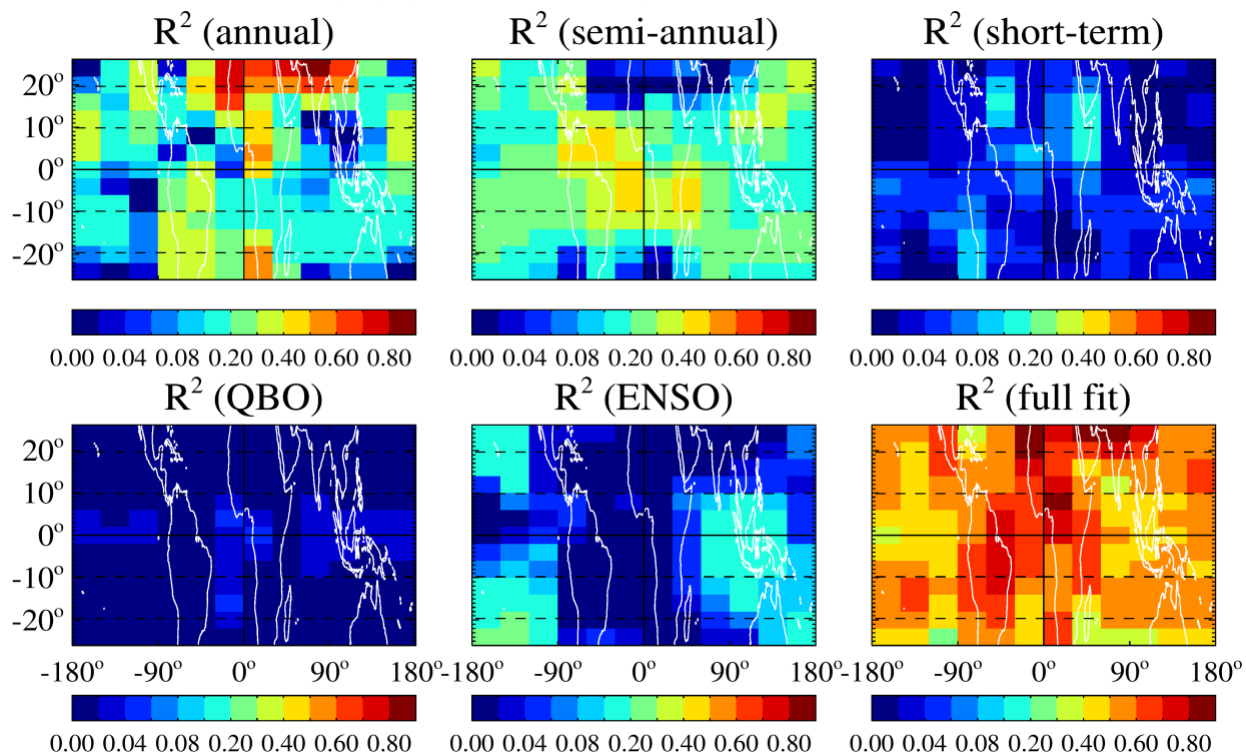
1518
1519
1520
1521

Figure 12(old14). Same as Fig. 10(old12), but for CO trends and all three model simulation results.

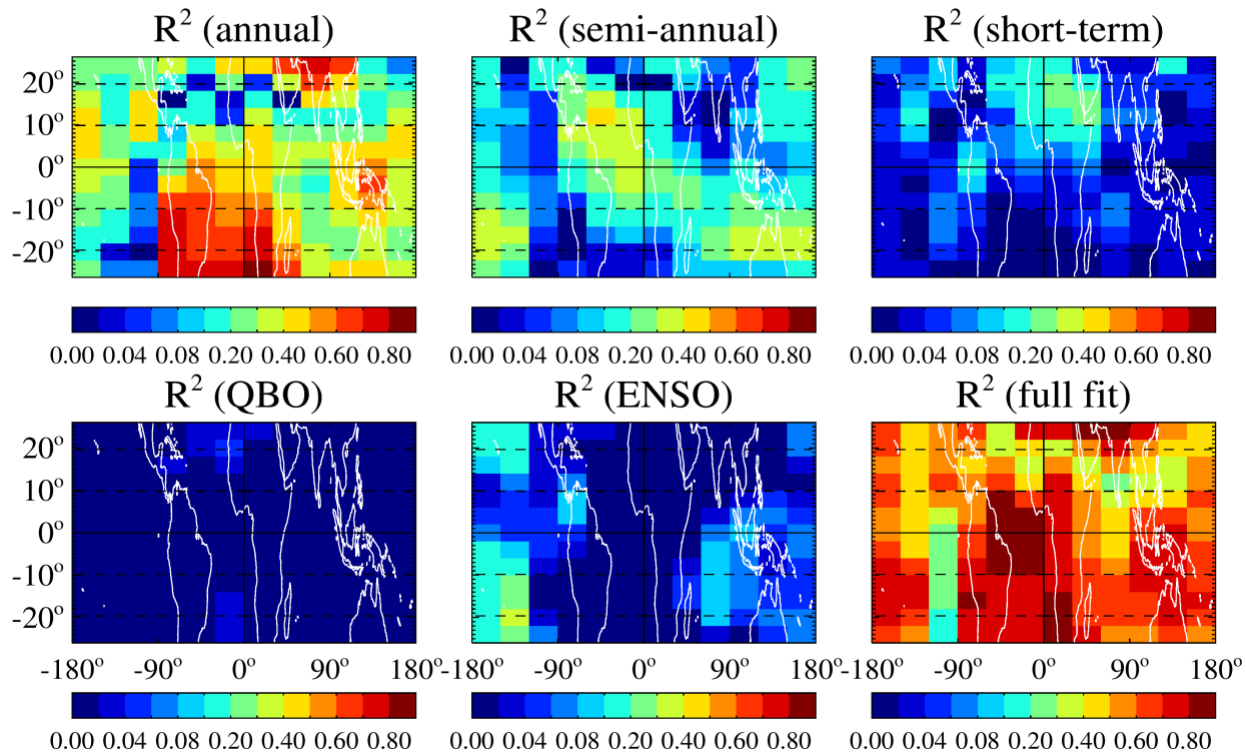


1522
 1523 **Figure 13(old15).** Contributions to the time series variance from the main fitted components of the
 1524 regression to the gridded tropical MLS ozone time series at 147 hPa (top 6 panels) and the same for the
 1525 WACCM-CEDS time series (bottom 6 panels). The titles in each panel indicate that the explained variance
 1526 is from specific components (annual, semi-annual, short-term, **meaning 3- and 4-months**, QBO, ENSO, and
 1527 full fit).

MLS CO: Variance Contributions at 147 hPa



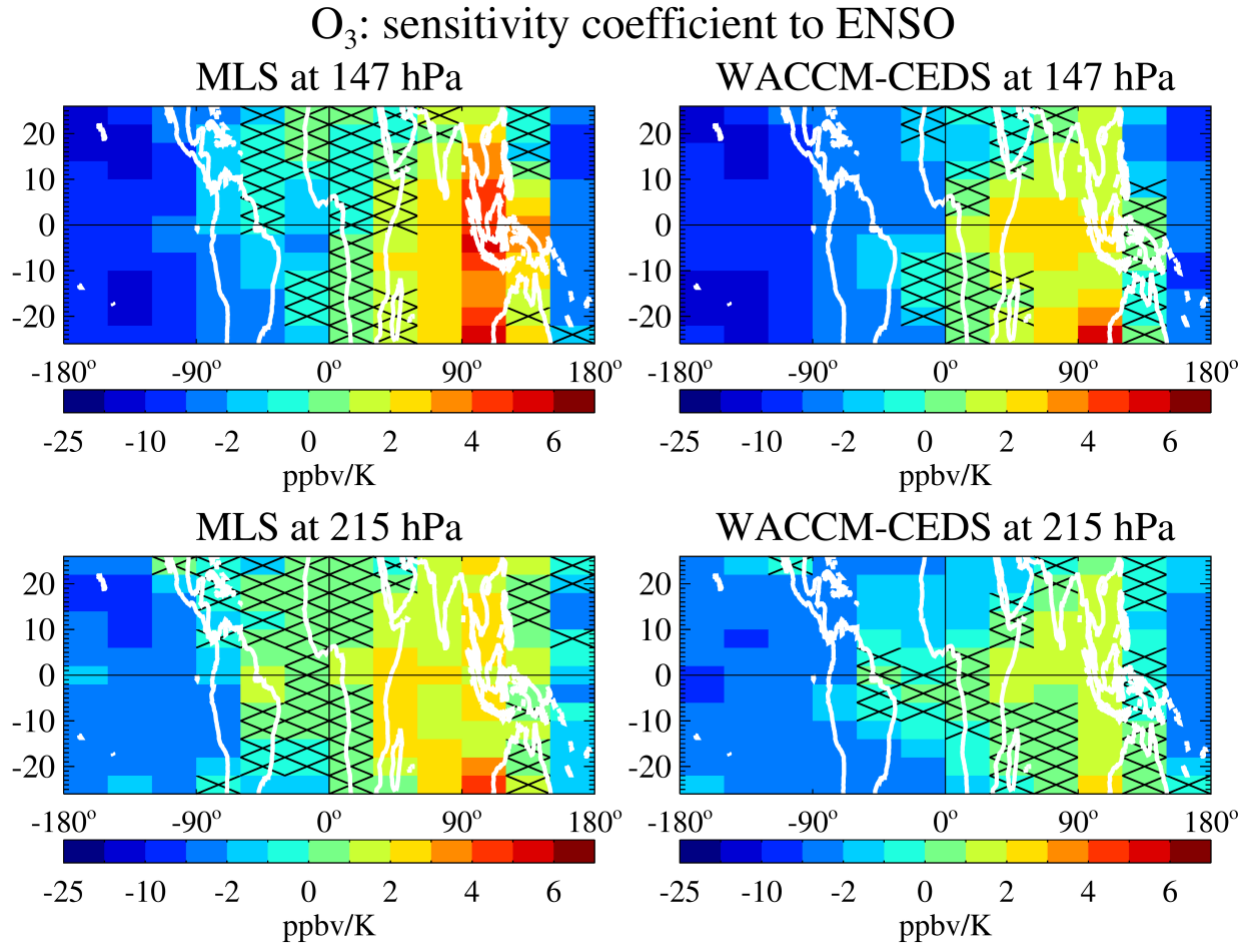
WACCM-CEDS CO: Variance Contributions at 147 hPa



1528
1529
1530

Figure 14(old16). Same as Fig. 13(old15), but for CO

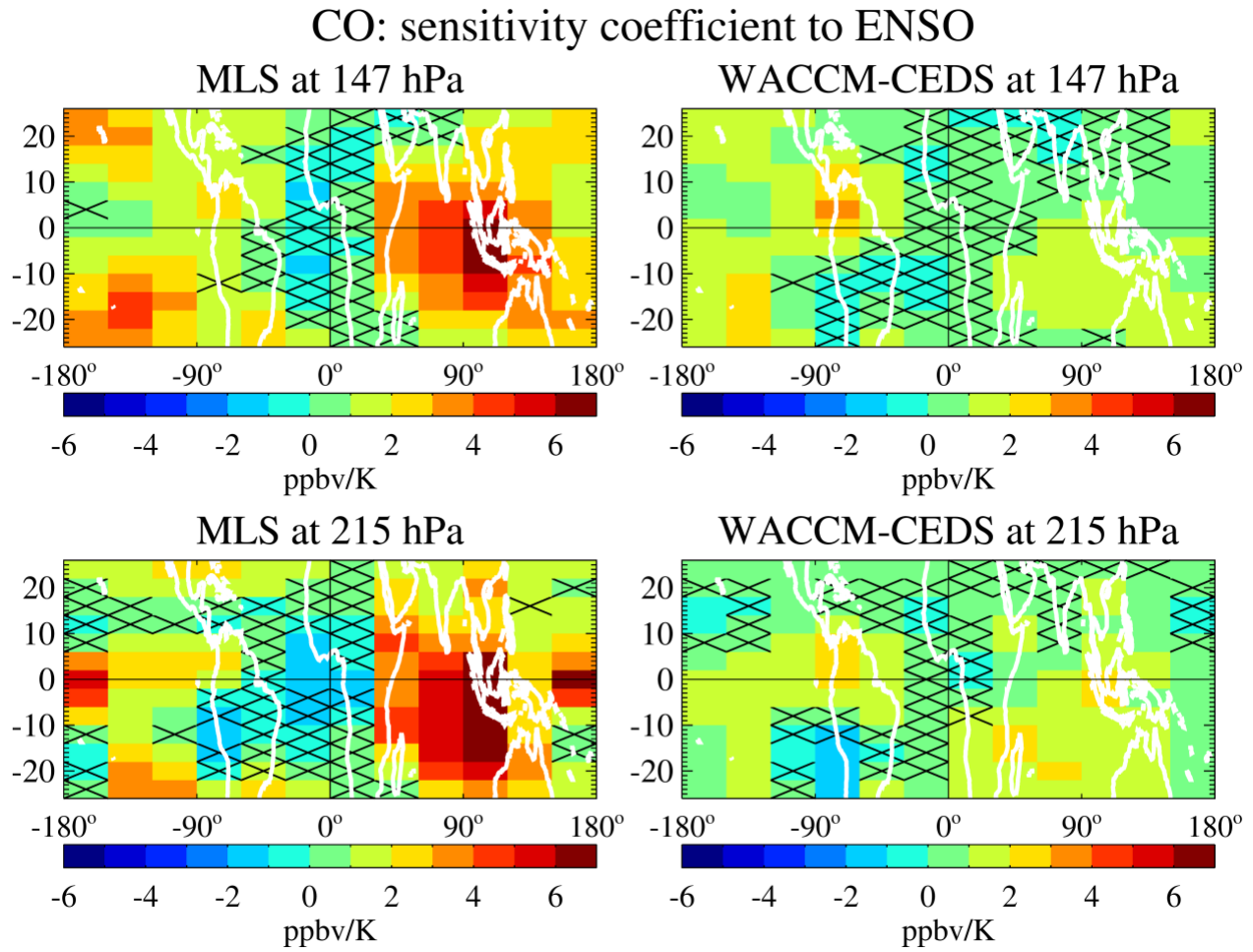
1531
1532



1533
1534
1535
1536
1537
1538
1539
1540

Figure 15(old17). Sensitivity coefficient to ENSO for ozone at 147 hPa (top panels) and 215 hPa (bottom panels); MLS results are shown in the left panels and the WACCM-CEDS results in the right panels. The black crosses show the grid boxes for which the sensitivity is not significantly different from zero (based on the 2σ error estimates). **Note that this color bar is asymmetric, with much larger negative values than positive values.**

1541
1542
1543



1544
1545
1546
1547
1548

Figure 16(old18). Same as Fig. 15(old17), but for CO; unlike for O₃, there is no need here for an asymmetric color bar, but the positive range is the same as in the O₃ Figure.